Università degli Studi di Napoli *Federico II*

DOTTORATO DI RICERCA IN

FISICA

Ciclo XXXII

Coordinatore: prof. Salvatore Capozziello

Photoemissive inorganic nanomaterials: characterization and their application in biophotonics

Settore Scientifico Disciplinare FIS/03 – FIS/07

Dottoranda

Chiara SCHIATTARELLA

Tutor

Prof. Raffaele VELOTTA

Dr. Ilaria REA

Anni 2017/2020

Acknowledgments

In un periodo storico particolare quale quello che tutti noi stiamo vivendo, mi accingo a mettere il punto sul percorso professionale, ma anche personale, degli ultimi tre anni. Un dottorato: due laboratori, due gruppi di ricerca, due approcci da conciliare. Devo ammettere che all'inizio non è stato semplice. Guardandomi indietro, prendo coscienza di quanto sia cresciuta e di come ciò non sarebbe stato possibile senza tutte le persone che vorrei qui sinceramente ringraziare. In tal senso, purtroppo, non sono mai stata formalmente brava né particolarmente verbosa, non me ne vogliano i diretti interessati.

Ringrazio i miei tutor, il prof. Raffaele Velotta e la dott.ssa Ilaria Rea, che con serietà, competenza e larghezza d'idee, mi hanno guidato in un filone di ricerca complesso e multidisciplinare, in cui un dialogo e una sinergia tra competenze diversificate diventa fondamentale.

Ringrazio il dott. Luca De Stefano per la fiducia che ho sempre sentito essermi accordata, nonché per avermi indirizzata verso la mia arricchente esperienza oltreoceano.

Ringrazio con affetto tutti i (tanti) colleghi dei laboratori UniNA e CNR: chi dall'inizio, chi di passaggio e chi nell'ultimo periodo, grazie per aver alleggerito la mia quotidianità, ovunque mi sia trovata a lavorare ogni giorno. Ringrazio un po' di più Martina e Rosalba, compagne di percorso da quel 1 febbraio 2017 e che ora, come me, sono in dirittura di arrivo; in bocca al lupo a noi, ragazze. Grazie al dott. Bartolomeo Della Ventura per la sua immensa disponibilità e pazienza nella gestione dei cosiddetti "problemi sperimentali" (di cui nessuno ha mai sentito certamente parlare…). Grazie anche al sig. Guido Celentano che, fino all'ultimo, anche durante i lunghi periodi di lontananza dal dipartimento, ha sempre fugato ogni dubbio e preoccupazione, supportandomi nella risoluzione delle tediose ma inderogabili procedure amministrative.

Ringrazio i miei più fidati e "antichi" amici: Francesco, Emanuele e il solo fisicamente lontano Mario, compagni di avventure, burle e corbellerie di dubbia ratio che hanno decisamente aiutato a risollevarmi nei momenti di sconforto.

Ringrazio te, Mrs. Grace, ovunque tu sia, anche se non approveresti affatto la cadenza decisamente poco Britannica che ha acquisito il mio Inglese.

Ringrazio la mia amica Tiziana, la persona da cui, ormai cinque anni fa, posso considerare essere partito tutto e che, anche a distanza, mi ha fatto sempre sentire il suo sostegno.

In ultimo ringrazio la mia famiglia tutta, in particolare mamma, papà e mia sorella che, anche se non lo dico né lo dimostro mai, sono per me importanti come l'aria che respiro.

Table of contents

Abstract

The present thesis work summarizes three years of research in the field of nanotechnology applied to life sciences. In the recent years, nanotechnologies and in particular nanomaterials have greatly sparked the interest of the scientific community: their small size and tunable functional properties make them appealing as tools for biomedical applications, ranging from bioimaging, biosensing to drug delivery and, in perspective, theranostics. Herein, the common feature is given by the property of distinctive photoluminescence from inorganic nanostructures whose "bulk" counterpart exhibits negligible emission. Indeed, in this thesis, the potentialities of three inorganic nanomaterials, porous silicon, graphene oxide and nanostructured zinc oxide, each of them exhibiting specific photoluminescence, will be investigated and successfully employed for applications in biophotonics, with focus on the bioimaging and biosensing fields.

This document is structured into three main blocks. Chapter I and II outline an introduction and a description of the fundamental concepts behind the studied nanomaterials properties and their potential manipulation *via* proper chemical strategies. The substantial results and discussion on the examined nanostructures characterizations will be explicated in Chapter III, describing their crucial role and their versatility in the development of innovative nanodevices. Most importantly, Chapter IV and V will be devoted to the final applications of the characterized and optimized platforms, which include label-free *in vivo* time-gated fluorescence imaging using *Hydra vulgaris* as target organism and multi-parametric optical biosensing for early diagnostics with focus on Brugada syndrome. Lastly, other interesting results achieved working on another typology of nanostructured material, namely noble metal nanoparticles, are reported in the Appendix.

The experimental activity has been "spread" for the whole PhD program duration. In particular, time-resolved photoluminescence measurements and *in vivo* time-gated imaging setup implementation have been optimized in the Optical Biosensors Lab at the department of Physics "E. Pancini" of University of Naples "Federico II"; whereas the surface chemistry processes design, fabrication of the functional platforms, morphological, structural and optical characterizations as well as *in vitro* and *in vivo* fluorescence imaging have been carried out at the Naples Unit of the Institute of Applied Sciences and Intelligent Systems (former Institute for Microelectronics and Microsystems) of National Research Council.

List of Figures

Chapter I

Chapter II

Chapter III

Chapter IV

List of Tables

Chapter I – Fundamentals

1.1 Introduction

The term “biophotonics” is referred to the field of research, which studies the wide variety of processes and interactions involving photons belonging to the UV-VIS-NIR range of the electromagnetic spectrum and biological matter (ranging from elementary compounds like peptides, up to living, complex organisms) [1]. Contextually, nanotechnologies have greatly developed in the recent years and the exploitation of nanostructured materials as tools in the biomedical field has greatly arisen [1].

Materials electronic and optical behavior can crucially change from the bulk to the nanoscale regime, conferring them with striking optical, photonic as well as morphological properties that can be exploited for the design and development of innovative nanodevices such as label-free fluorescent probes for bioimaging, optical biosensors with hybrid transduction mechanisms to even reach theranostic platforms. In this perspective, a key parameter is represented by the characteristic photoluminescence (PL) emission from semiconducting nanostructures. The origin of this phenomenon may be ascribed to different mechanisms, including lattice defects-induced radiative transitions or quantum confinement phenomena.

In this chapter, an outline of the photophysical properties of three emissive semiconductor nanomaterials, porous silicon, graphene oxide and zinc oxide, will be briefly discussed and contextualized. In that, such nanostructures constitute the starting point for the development of innovative platforms for applications in biophotonics.

1.2 Porous silicon

1.2.1 Porous silicon fabrication and photonic properties

Porous silicon (PSi) is a nanostructured form of silicon consisting of an irregular network of nanometric crystalline wires with variable dimensions and air holes. It was accidentally discovered by A. Uhlir in 1956 while conducting a study on electrolytic shaping of semiconductor surfaces, describing it as a “matte black, brown or red deposit”

[2]. In 1990, visible photoluminescence from PSi structures was firstly observed [3], [4]. Since then, a growing interest for this material has arisen thanks to its potential in a myriad of applications, ranging from optoelectronics to the biomedical field. In fact, the predisposition towards integration in CMOS-based technologies, efficient light emission from properly designed nanostructures, coupled with properties of biocompatibility, non-toxicity, biodegradability and versatile surface chemistry make PSi fully exploitable in the aforementioned contexts [5].

To date, the most utilized method for PSi fabrication is the electrochemical etching in hydrofluoric acid (HF)-based solutions. This process exploits the reaction:

$$Si + 6F^- + 2H^+ + 2h^+ \rightarrow SiF_6^{2-} + H_2.$$

In a typical etching setup, the silicon wafer acts as the anode, which is back-contacted on an aluminum plate, while the frontside is sealed with an O-ring and exposed to the electrolyte in which the cathode is immersed (Figure 1 | 1(a)). All the materials employed, from the metallic anode to the cell itself, are made of HF-resistant materials. In that, the sponge-like morphology of PSi can be tuned in terms of pores size, crystalline domains dimensions as well as layer thickness, by properly setting the HF concentration, current density and etching time [5]. The great variety of morphologies of PSi is also dependent on the doping (n or p, low or high) of the Si substrate. The IUPAC guidelines define ranges of pores size with specific properties [6]: nanostructures with pore diameter $\leq$ 2 nm are classified as “microporous”; the range 2-50 nm is regarded as “mesoporous”; whereas the cases of sizes > 50 nm are labelled as “macroporous” (Figure 1 | 1(b)).

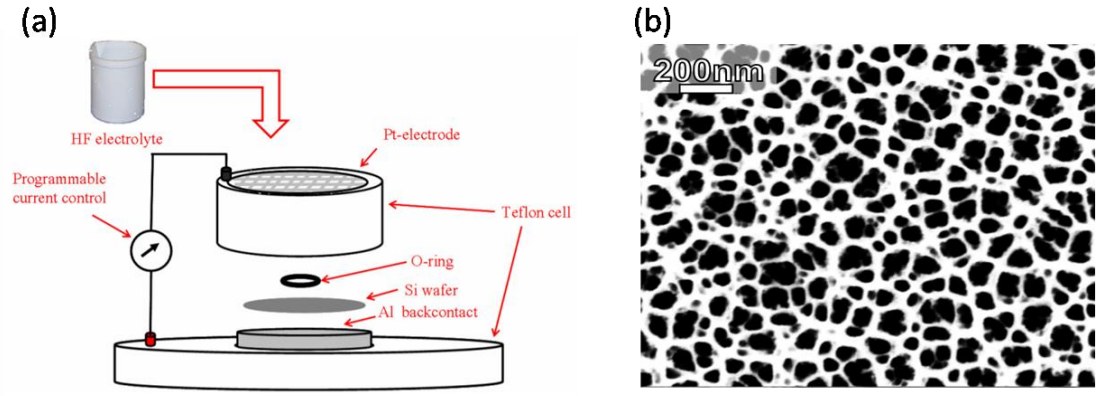

Figure 1 | 1. (a) Sketch of a typical setup for electrochemical etching of Si. (b) Typical morphology of a macroporous Si structure.

Different porosities can be combined to achieve personalized photonic properties basing on the layer refractive index variations, i.e., by tuning the "void" fraction within the PSi matrix. In fact, a proper current density temporal profile during the etching process always corresponds to a specific resulting refractive index profile. This implies that PSi multilayered photonic structures can be designed, including Fabry-Pérot interferometers [7], Bragg reflectors [8], optical microcavities [9], rugate filters [10] and others [11] (Figure 1 | 2).

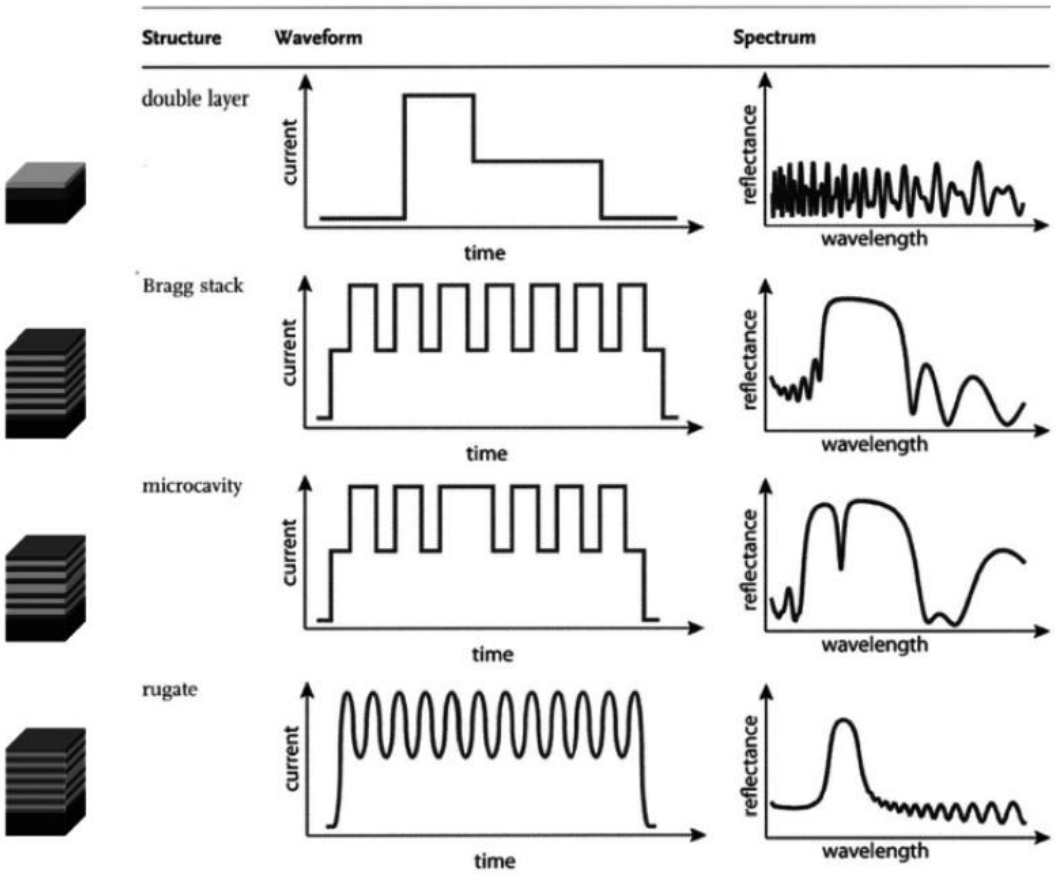

Figure 1 | 2. Examples of achievable PSi photonic structures with different current density profiles [12].

The simplest PSi structure is a fixed porosity monolayer and acts as a Fabry-Pérot interferometer, in which the involved interfaces, responsible of the interference fringes pattern, are Si/PSi and PSi/air. This feature is sensitive to the changes in the environment within the air holes in the structure, i.e., to the refractive index changes due to some substance infiltration. In the present thesis, such optical coding variations will be exploited for the development of a biosensing hybrid chip.

1.2.2 Photoluminescence from porous silicon

The exact origin of the mechanism of photoluminescence emission from PSi has been debated for long. Different models that have been proposed to explain it include the emission from occurring siloxene (Si:H:O) polymeric structures [13], [14] or amorphous Si structures [15], as well as quantum confinement phenomena from nanometric silicon crystallites [16], [17]. Among them, the latter represents the most utilized interpretation, as well as that mostly supported by experimental investigations [18].

It is well-known that crystalline bulk semiconductors energetic structure can be described using the notion of energy band, i. e., a continuum of energy levels occupiable by charge carriers and separated by a forbidden gap. Photon-induced radiative transitions from the valence to the conduction band in semiconductors may occur if the supplied photon energy exceeds such band-gap ($E_{ph} > E_G$). However, in the case of bulk silicon, which is an indirect bandgap semiconductor (Figure 1 | 3), direct band-to-band transitions hold an extremely low probability, since the assistance of a momentum supplied by a phonon arises. Phonons interaction with photons make indirect optical transitions possible by satisfying the momentum conservation rule in a second-order process [19].

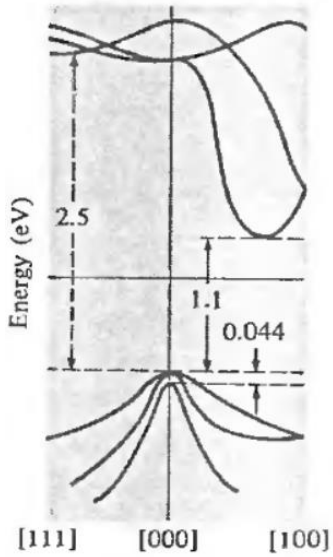

Figure 1 | 3. Band structure of bulk silicon [20].

The quasi-particles involved in the radiative transition processes are the excitons, i.e., the hydrogenic system of excitation-induced electron-hole couple, paired by coulombian attractive interaction [19]. A relaxation of the k-conservation rule in indirect

bandgap nanocrystals is manifested when quantum confinement effects become significative: due to Heisenberg uncertainty principle ($\Delta x \Delta p \geq \hbar/2$), when the size of a semiconductor structure decreases, i.e., electrons and holes spatial wave functions become more localized, their wave functions in the k-space spread accordingly. This implies a high confinement energy (> 0.7 eV), their significant overlap and a possible exciton recombination without the assistance of phonons [21], even with high efficiencies. Single Si nanocrystals with nearly 100% internal quantum efficiency have been reported [22]. However, this description represents an approximation (at the single nanocrystal level) of what is the real situation in luminescent porous silicon, which can be rather depicted as a network of interacting nanometric quantum-confined emissive domains.

Analogously to the energy levels of a particle in an infinite potential well, PL emission in PSi exhibits a power law dependence on the size d of its nanocrystalline structures (Figure 1 | 4); theoretical models predicting a $d^{-1.39}$ dependence were determined [17], [23].

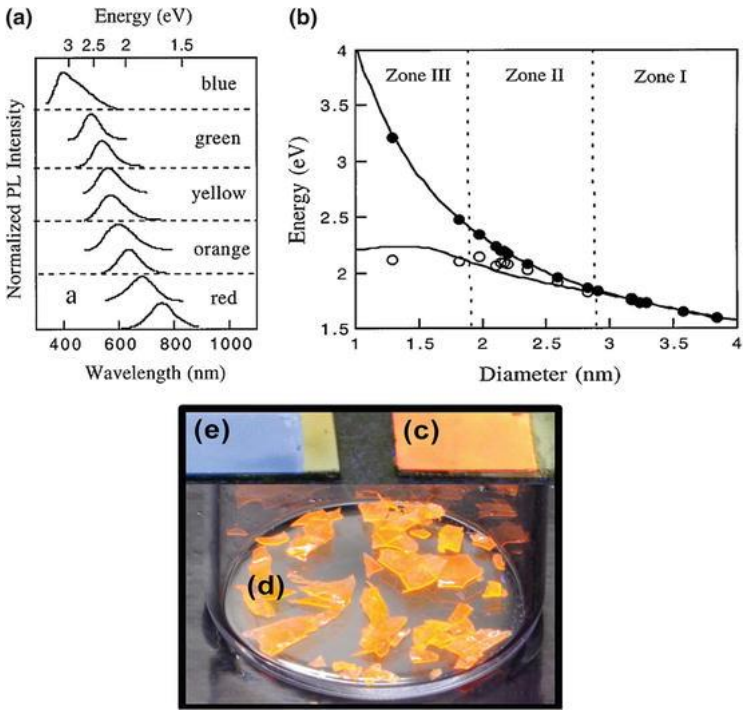

Figure 1 | 4. (a) Room-temperature PL spectra from porous silicon layers with different porosities. (b) Experimental and theoretical PL energies as a function of crystallite size. The upper line is the free exciton bandgap and the lower line is the lowest transition energy in the presence of a Si = O bond. The solid and open dots are the peak PL energies of PSi samples kept in Ar and air, respectively. (c) PL under UV excitation of a porous silicon layer, (d) the same membrane once detached and (e) the same type of porous layer heavily thermally oxidized [24].

Experimentally, PSi exhibits two distinctive PL spectral features. The excitonic red-NIR component is the most studied and technologically interesting and is denoted as S-band (where S stands for "slow") whose decay times are long compared to those of direct bandgap semiconductors (cf. next Section); nonetheless, it is also electrically excitable and its properties can be in principle engineered [25]. Besides, a so-called F-band (where F stands for "fast"), with emission maximum in the blue range of the VIS spectrum, has been reported in various thermally or chemically oxidized PSi samples. The PL lifetime lies in the nanosecond range. Many reports have attributed this band to oxide-related defects or undesired contamination [26], [27].

Finally, PSi luminescence is reported to undergo significant degradation under illumination in oxidizing environment, resulting in a decrease of PL efficiency [28]. This type of PL degradation is irreversible and severely limits PSi applications in the biophotonics field. Thus, proper surface capping strategies must be designed in order to overcome this issue (cf. Section 2.1).

1.2.3 Photoluminescence emission dynamics in porous silicon

In general, a characteristic relaxation time τ is associated to the excited carriers; the transition rate from an excited state back to the ground state is given by its inverse, $1/\tau$. Both radiative and non-radiative channels probability contribute to this quantity, thus being defined as:

$$\frac{1}{\tau} = \frac{1}{\tau_r} + \frac{1}{\tau_{nr}},$$

where τ_r and τ_{nr} are radiative and non-radiative lifetimes, respectively. As a consequence of the enhancement of the oscillator strength ($\frac{1}{\tau} \propto |\langle i_{CB}|\hat{p}|f_{VB}\rangle|^2$) due to quantum confinement, the PL lifetime of silicon nanocrystals at room temperature is relatively long (~μs) due to the indirect nature of the bandgap [29] and can be even longer at cryogenic temperatures (~ms) due to the progressive triplet state population [16]. Still, the oscillator strength for radiative transitions in Si nanocrystals is found to be significantly smaller than that of direct gap semiconductor nanostructures (whose lifetime usually lies in the ns range [30]). Hence, despite quantum confinement effects contribute to the arising of an efficient emission, PL from Si nanocrystals appears to be rather dominated by the suppression of non-radiative relaxation channels [31].

By its very nature, PSi can be described as a disordered system. This assumption is fundamental when it comes to describe the dynamic behavior of radiative quantum-confined emission processes in PSi. In fact, the photoluminescence recombination mechanism and carrier dynamics of an ensemble of Si nanocrystals exhibit a temporal decay shape described by the stretched exponential function:

$$I(t) = I_0 e^{-\left(\frac{t}{\tau}\right)^{\beta}}$$

where τ and β are lifetime and decay factor, respectively. In particular, the dispersion factor β ($0 < \beta \leq 1$) represents the distribution of the lifetimes in the system. A significant clue of the role of the disorder lies on the fact that different time-resolved studies report this dynamic PL behavior and that almost all the proposed models make use of some concept of disorder [32]–[34]. In the perspective of PSi as a skeleton of quantum-confined emissive structures, the notion of "disorder" is referred to factors such as a finite-width distribution of the nanocrystalline domains size; their random spatial arrangement as well as the structure of the nanocrystals surfaces [35]. Simultaneously, the dispersion factor β can be possibly interpreted as an extrinsic quantity, only dependent from the macroscopic properties of the medium surrounding the emissive nanostructures [31].

The characteristic long-lived emission from quantum-confined Si nanostructures represents a key feature that will be exploited for the implementation of time-gated fluorescence imaging *in vivo*, employing luminescent PSi nanoparticles (PSiNPs) as label-free probes.

1.3 Graphene oxide

Graphene is a single-atom thick layer of carbon atoms arranged in a two-dimensional honeycomb lattice [36]. It represents the fundamental constituent of graphite, which is an inexpensive and widely available material. In 2004, Andre Geim and Konstantin Novoselov firstly outlined the ambipolar electric field effect from single-layer graphene sheets [37]. Such outcome awarded the two researchers with the Nobel Prize. After Geim and Novoselov's breakthrough, graphene catalyzed the interest of the scientific community. Its striking electronic, optical and mechanical properties make graphene

desirable as raw material for several technological applications, such as solar cells, touch-screens, transistors, membranes, gas sensors and others [38].

However, pristine graphene suffers from severe limitations for its employment in the biomedical field. Amongst other things, it is a hydrophobic material and its chemical inertness significantly limits its feasibility of use in terms of realizable and robust surface anchoring of functional biomolecules. On the other hand, graphene oxide (GO; and also its reduced form - rGO) constitutes a more promising alternative: it is hydrophilic thanks to the myriad of moieties (carbonyl, carboxyl, hydroxyl, epoxide) spread throughout the single sp^2 carbon sheet. Such functional groups are also greatly exploitable for covalent bioprobes conjugation *via* well-established chemical approaches. Nonetheless, the bandgap opening results in an excitation-dependent broad PL emission from GO, with maximum in the red range (Figure 1 | 5).

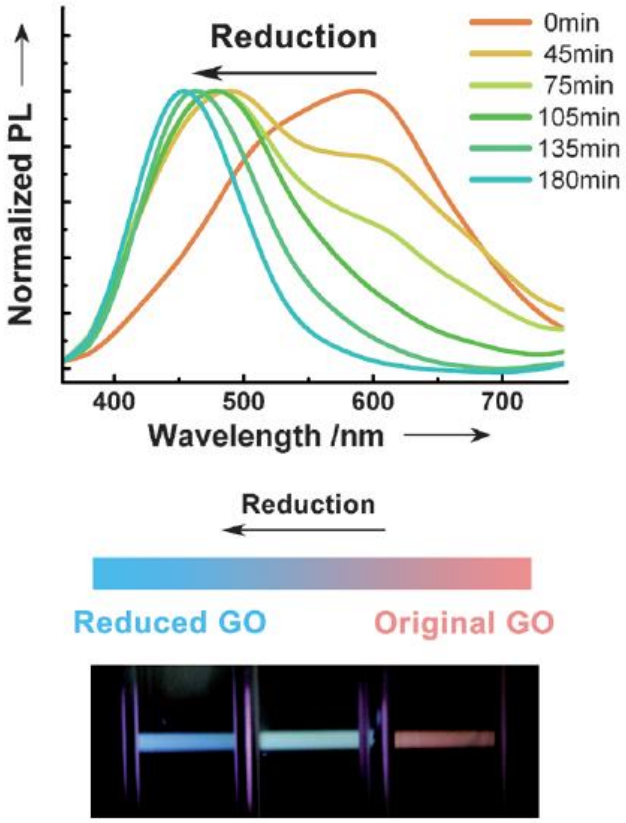

Figure 1 | 5. Normalized PL spectra of GO suspensions after different reduction times (0-180'). The lower panel shows the tunable PL emission from GO at 0 min (red), 75 min (green) and 180 min (blue) reduction times (adapted from [39]).

The exact origin of PL from GO is still debated: some groups have ascribed GO PL to bandgap transitions involving electron-confined sp^2 islands [40], [41], even though it seems more likely to arise from oxygen-related defect states. In particular, electron-hole recombination from the bottom of the conduction band and nearby localized states to wide-range valance band is suggested as origin of the fluorescence [42]. The excitation wavelength dependence of GO PL can be attributed to relative intensity changes of few emission species, namely from the electronic transitions among/between the "pristine" sp^2 carbon regions and the boundary of oxidized carbon atom regions where all three kinds of functional groups (C-O, C = O and O = C-OH) occur. This evidence is supported by the demonstrated tunability of PL maximum and bandwidth with the degree of reduction (Figure 1 | 5 and Figure 1 | 6) [39], [43].

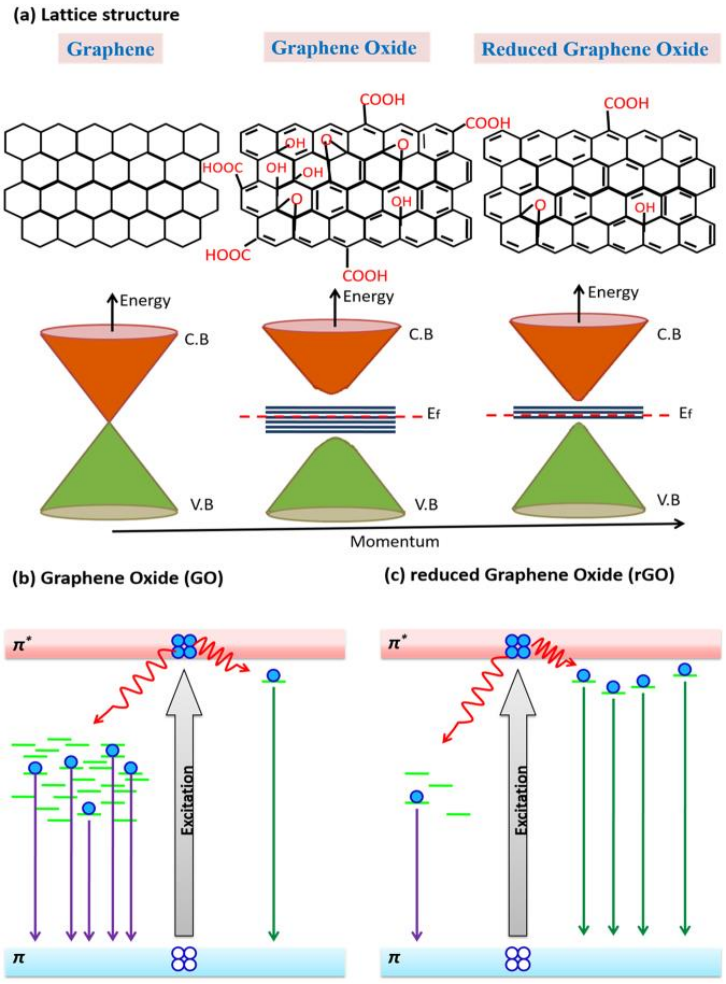

Figure 1 | 6. Band structure of pristine graphene compared to that of GO and rGO. In the latter cases, the proposed mechanism of radiative relaxation is also represented [44].

Fluorescent species emitting in the IR and NIR have great potential for biological applications, thanks to the reduced autofluorescence contribution in this spectral region [45]. In that, GO has been exploited as theranostic tool for simultaneous low-noise cell imaging and drug delivery [46]. In this thesis work, the PL characteristics and variations of few nm-sized GO nanosheets have been examined and monitored for biosensing purposes (cf. Chapter III-V).

1.4 Zinc oxide

Zinc oxide (ZnO) is a direct-bandgap semiconductor with a considerable fraction of ionic bonding. ZnO occupies a special place among wide bandgap semiconductors (GaN, ZnS), since it is considered to be the most favorable for creating light-emitting diodes and laser diodes with emission in the UV range. This is a consequence of its ultrafast radiative relaxation dynamics. Due to its thermal, optical, acoustic, and electric properties, ZnO nanostructures also find use in solar cells, gas sensors, varistors, generators of surface acoustic waves as well as scintillators [47].

Under ordinary conditions, ZnO crystallizes in a wurtzite structure with a hexagonal cell. The Zn–O spacing along the *c* axis is slightly shorter than that along the orthogonal direction (inset Figure 1 | 7(a)). The wide bandgap of ZnO (E_g = 3.4 eV) can be deduced from the high ionization energy of oxygen. This implies a strong interaction between the Zn 3d and O 2p orbitals [48]. Mixing of anionic p- and cationic d- orbitals in ZnO leads to a low position of the bottom of the conduction band [48].

Various forms of ZnO, including single crystals, thin films, nanocrystals, nanowires, etc., all exhibit two luminescence bands: a sub-nanosecond-lived (τ_{em} ~ 0.7 ns) short-wavelength band, which is spectrally located near the absorption edge of the crystal, i.e., the so-called “edge luminescence”, and a broad long-wavelength band, the maximum of which usually (but not always) lays in the green spectral range, herein regarded as “green luminescence” for the sake of simplicity. In particular, the edge luminescence (with maximum emission usually at λ_{max} ~ 380 nm) may involve the participation of free excitons (Xs) [49], excitons bound to acceptors and donors and their corresponding two-electron satellites, and donor–acceptor pairs (Figure 1 | 7(c)). Besides, the exact nature of the green luminescence emission is still unclear. Different types of lattice sites have been pinpointed as responsible of the green PL, including oxygen vacancies [50], zinc vacancies [51],

interstitial zinc ions [52] and also transitions between the latter two [53]. On average, all the proposed models are attributable to defect-induced radiative sites. This is a natural consequence of intrinsic imperfection of ZnO crystals, instability of certain point defects, and the variety of their forms. Therefore, it seems most likely that more centers may be involved in the green luminescence simultaneously rather than a particular one.

The doping-sensitive characteristics of ZnO nanostructures can be potentially exploited for the development of optical biosensing devices, as will be better discussed in Chapter III.

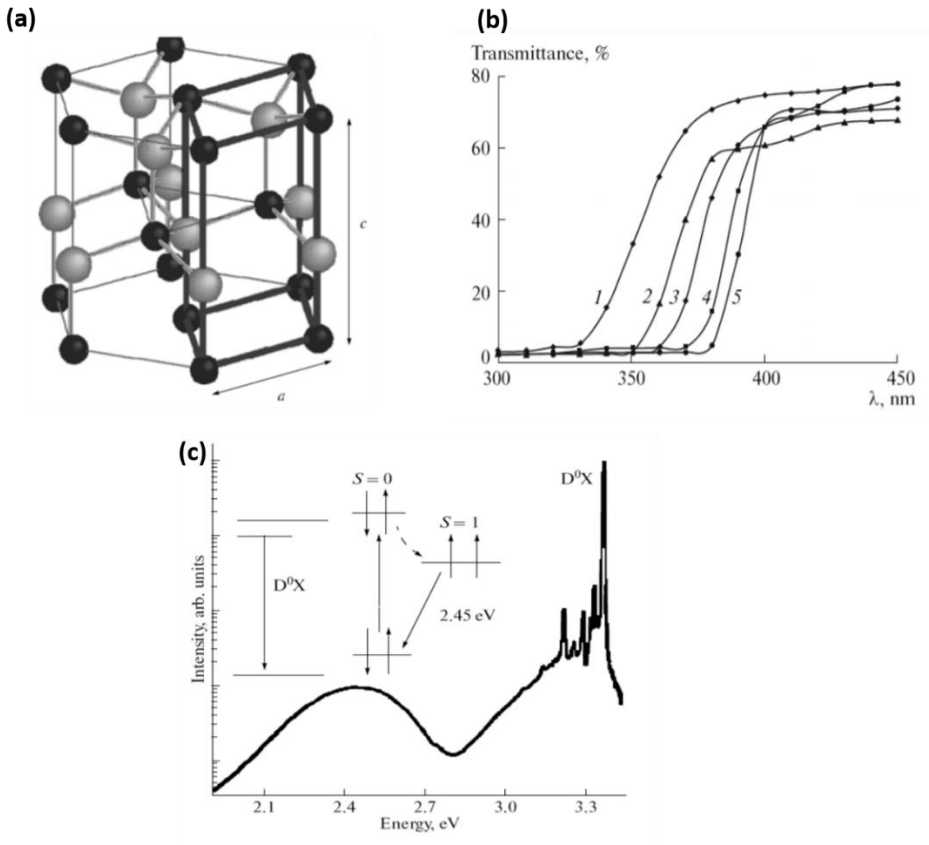

Figure 1 | 7. (a) ZnO crystal lattice [47]. (b) Transmittance spectrum of ZnO at different dopings [47]. (c) Typical PL spectrum of ZnO. The principal near-edge excitonic line can be ascribed to donor-bound excitonic transitions (indicated in the inset as D^0X) [47].

Chapter II – Bio/non-bio interfaces for biophotonic applications

A trivial, despite significant advantage of nanomaterials is the predisposition towards the tunability of the relevant properties *via* a properly designed functionalization process. The present chapter is devoted to a brief description of the chemical strategies that have been employed to add characteristic features to the "pristine" nanomaterials, including covalent approaches for effective surface modification: hydrosilylation, carbodiimide and silane crosslinking chemistries.

2.1 Hydrosilylation

As-etched PSi structures exhibit Si-H surface bonds, which is a highly thermodinamically unstable chemistry. Such bonds are highly prone to substitution with Si-O-Si in any oxygen-containing environment. This represent an important drawback when dealing with highly luminescent (i.e., highly nanostructured) PSi surfaces. The nanocrystalline photoemissive skeleton is easily compromised in terms of optical properties in this condition, since oxygen atoms may introduce surface defects [27] which act as radiative recombination sites responsible for a short-lived (ns range, cf. Section 1.2.2) PL emission in the blue area of the VIS spectrum. In that, quantum-confinement transitions are almost suppressed. Aiming at overcoming this issue, several surface passivation protocols were developed, including controlled oxidation of PSiNPs in sodium tetraborate [54] or coating with polymers [55]. Among all the possible strategies, the covalent addition of functional groups to the PSi surface is an interesting alternative approach to PSi passivation [56]. In particular, hydrosilylation consists in the substitution of Si-H with more stable Si-C bonds. This process is usually assisted by heat [57], microwaves [58] or UV illumination [59] and must be carried out in inert atmosphere [60]. In general, hydrosilylation reaction can be used for the synthesis of organosilicon compounds [61].

Hydrosilylation is widely utilized as method to reduce the high reactivity of PSi surfaces in oxidizing environment. However, the choice of the molecule to be conjugated can be targeted to add other functional moieties. This can introduce further anchoring possibilities via, e.g., exploiting the chemistries that will be introduced in the next sections. Thermal hydrosilylation with undecylenic acid (UA – formula $CH_2=CH(CH_2)_8COOH$) as

capping agent (Figure 2 | 1) has been herein carried out both on luminescent PSi nanostructures colloid and on-chip aiming at achieving an inert Si-C chemistry as well as a carboxyl-terminal surface.

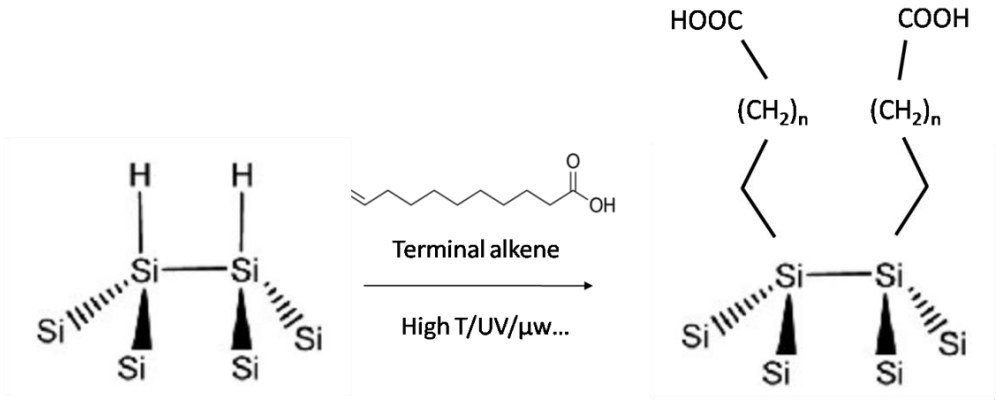

Figure 2 | 1. Sketch of the hydrosilylation process. The substitution of Si-H with Si-C bonds occurs only under catalytic conditions (high temperature, UV illumination, microwaves).

2.2 Carbodiimide chemistry

In organic chemistry, carbodiimides are functional groups having a basic structure RN=C=NR. Specifically, they are used to convert carboxylic acids to amides or esters [62]. In that, additives such as N-hydroxybenzotriazole or N-hydroxysuccinimide, are often added to increase the yield of the target process and, at the same time, decrease side reactions [62].

1-Ethyl-3-(3-dimethylaminopropyl)carbodiimide (EDC) is a water-soluble carbodiimide reagent used for a wide range of purposes. In particular, EDC is widely used as a crosslinker in many biochemical experiments, including peptide synthesis, protein crosslinking to nucleic acids, but also in the preparation of immunoconjugates. EDC basically acts as a carboxyl-activating agent for the coupling of primary amines to yield amide bonds. EDC is typically employed in the pH range 4.0-6.0 [63] and it is often used in combination with N-hydroxysuccinimide (NHS) for the immobilization of large biomolecules [64].

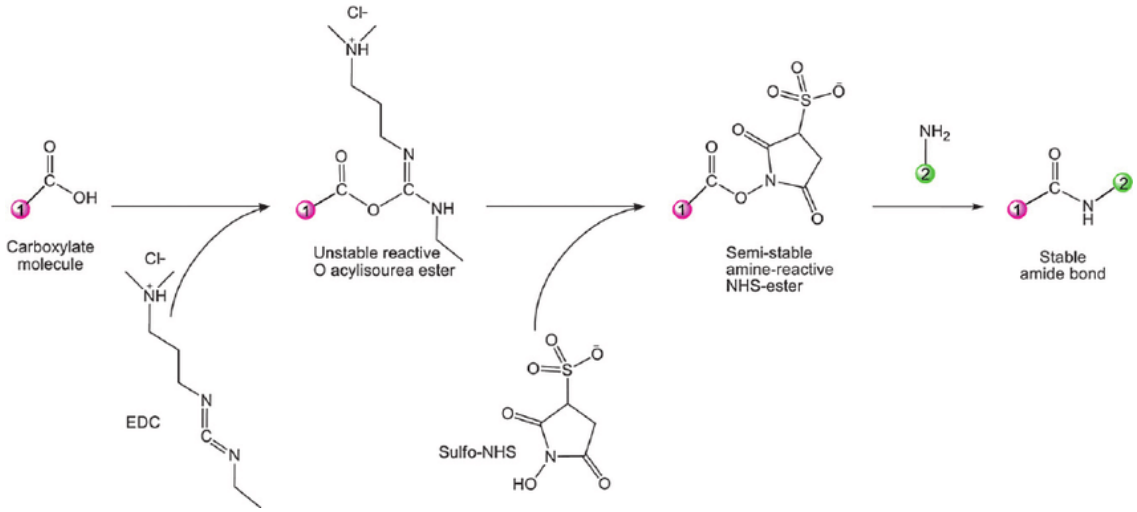

Figure 2 | 2. Scheme of EDC/NHS-mediated covalent conjugation between carboxyl and amine groups leading to the formation of amide bonds [65].

Figure 2 | 2 depicts the general subsequent steps for EDC/NHS-mediated coupling of carboxylic acids to amines under acidic conditions: firstly, the carbonyl of the acid attacks the carbodiimide group of EDC, thus resulting in a proton transfer. NHS acts by binding to the so-activated group and predisposes to the desired interaction with the amine to be conjugated. After discharging of the remaining byproducts; the desired amide bond is then finally obtained.

In the present thesis, EDC/NHS coupling chemistry has been widely exploited for achieving a covalent anchoring between different carboxyl-terminal and amine-terminal moieties for effective bioprobe immobilization.

2.3 Silane chemistry

Silanization is the covering of a surface with organofunctional alkoxysilane molecules [66]. Mineral components like glass and metal oxide surfaces can all be silanized, because they contain hydroxyl groups which attack and displace the alkoxy groups on the silane thus forming a covalent -Si-O-Si- bond. There are many types of commercially available silane-coupling agents, which are easy to react with hydroxyl-terminal surface and introduce active groups (e.g., amine group or carboxyl group). Among them, (3-Aminopropyl)triethoxysilane (APTES) is an aminosilane frequently used in the process of silanization (Figure 2 | 3).

Silanization is a low-cost and effective covalent coating method to modify hydroxyl-terminal material surfaces. Binding of silicon-based molecules on metal surfaces occurs because hydroxyl groups on metal surfaces can link steadily to silicon atoms. Silanized surfaces can also easily be modified by further grafting [67]. Since amine groups can react with proteins and DNA, silanized surfaces may find relevant applications in biotechnology [68]. In many applications, high surface coverage of amine groups is desired in order to have a large number of active sites on the surface for improving the performance of nanocomposites [69].

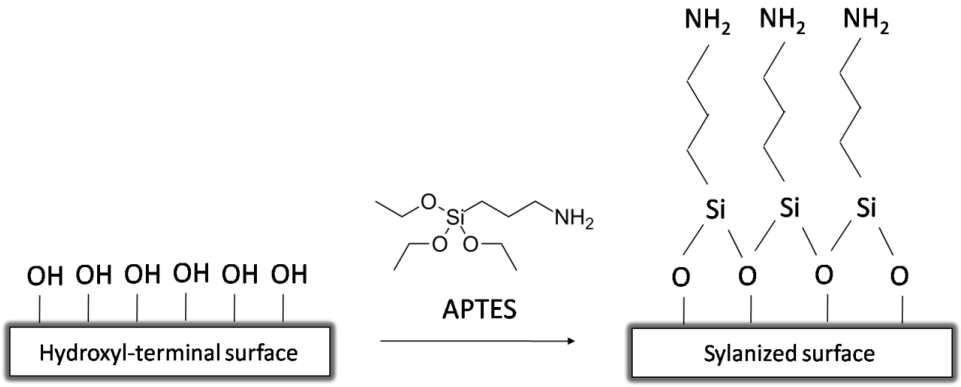

Figure 2 | 3. Outline of APTES-mediated silanization process.

Silanization with APTES is herein used to achieve an amine-terminal surface, making it prone to the use of a coupling chemistry *à la* EDC/NHS for biomolecules anchoring.

Chapter III – Materials and devices characterization

Herein, the main results on the examined nanomaterials fabrication, surface modification and characterization will be discussed. The effective tuning of the relevant optical and photonic properties as well as an enhancement of stability and robustness have been demonstrated.

3.1 Luminescent porous silicon nanoparticles

Porous silicon nanoparticles (PSiNPs) are non-toxic photoluminescent agents whose potential for biophotonic applications has been widely reported in recent years [70]. However, this material suffers from intrinsic limitations, due to its chemical instability and rapid photoluminescence extinction upon exposure to physiological environments. In order to overcome this limit, different surface passivation strategies have been developed. This section aims at showing the development and characterization of surface-modified PSiNPs with a view to their final *in vivo* time-gated imaging application (cf. Chapter IV).

3.1.1 Fabrication, functionalization and morphological characterization

Photoluminescent PSiNPs, fabricated by electrochemical etching, are herein chemically modified via hydrosilylation with undecylenic acid (UA). The replacing of metastable Si-H bonds with more stable Si-C ones (cf. Section 2.1) leads to a covalent surface passivation that prevents uncontrolled surface oxidation and subsequent PL degradation. The functionalization process does not modify the emission properties of nanoparticles in isopropanol, while it stabilizes the PL in physiological conditions.

Luminescent PSiNPs were obtained via electrochemical etching of low-doped p-type silicon wafers (1-5 Ω cm resistivity, <100> oriented, Siltronic-Wacker) in aqueous hydrofluoridic acid (HF) (30wt.%) and sulfuric acid (H_2SO_4) (38wt.%) mixture following an established protocol [71]. The resulting microporous silicon layer [72] was detached from the wafer by additional anodization in diluted HF-based solution, dispersed in isopropanol (IPA) to avoid air exposure and sonicated for 180 min to obtain micro and nanoparticles [72]. The resulting particle suspension was centrifuged 3 times at 6000 rpm for 10 min; the supernatant containing sub-micrometric PSiNPs was then collected and

characterized. The concentration of PSiNPs in IPA was 2 mg/mL, estimated by gravimetry using a Radwag AS82/220.R2 balance.

Surface chemistry modification was achieved via hydrosilylation with undecylenic acid as depicted in Section 2.1. All the chemicals were purchased from Sigma Aldrich. PSiNPs in IPA were placed in a vial with deoxygenated neat UA (99% v/v) and allowed to react overnight under Ar atmosphere at 110 °C under constant stirring. Hydrosilylated PSiNPs (hPSiNPs) were then extensively washed in IPA in order to remove residual unreacted reagent.

The remarkable red-orange PL emission was beforehand readily visible to the naked eye under illumination of low-power UV lamp (376 nm) right after the fabrication. The morphology of as-prepared PSiNPs was investigated by transmission electron microscopy (TEM). To this aim, 10 μL of (h)PSiNPs dispersed in IPA were placed on a TEM copper grid with a lacy carbon film, dried at room temperature and observed with a FEI Tecnai G2 Spirit BT TEM at an accelerating voltage of 100 kV. The TEM analysis revealed NPs with an irregular shape and a lateral dimension of about 450 nm, constituted of a network of holes and ensembles of nanometric crystallites (Figure 3 | 1(a)).

The presence of UA covalently conjugated to the surface of PSiNPs was investigated by Fourier Transform Infrared spectroscopy (FTIR). The spectra of bare PSiNPs and hPSiNPs were obtained using a Nicolet Continuum XL microscope (Thermo Scientific) in the wavenumber region of ~3200−700 cm^{-1} with 4 cm^{-1} resolution. The results of FTIR analysis, reported in Figure 3 | 1(b), demonstrated the successful UA bonding onto PSiNPs: the FTIR spectrum of air-dried bare PSiNPs showed peaks corresponding to Si-O-Si and Si-H_x bonds at 1200-1100 cm^{-1} and 985-800 cm^{-1}, respectively [5], [73]. After reaction, other peaks due to C-H_x (2920-2850 cm^{-1}) and carbonyl C=O stretching (1700 cm^{-1}) vibrations appeared [73]; the decreasing of Si-H_x peak intensity was compatible with the functionalization process that consumed silicon-hydrogen bonds inducing formation of silicon-carbon ones.

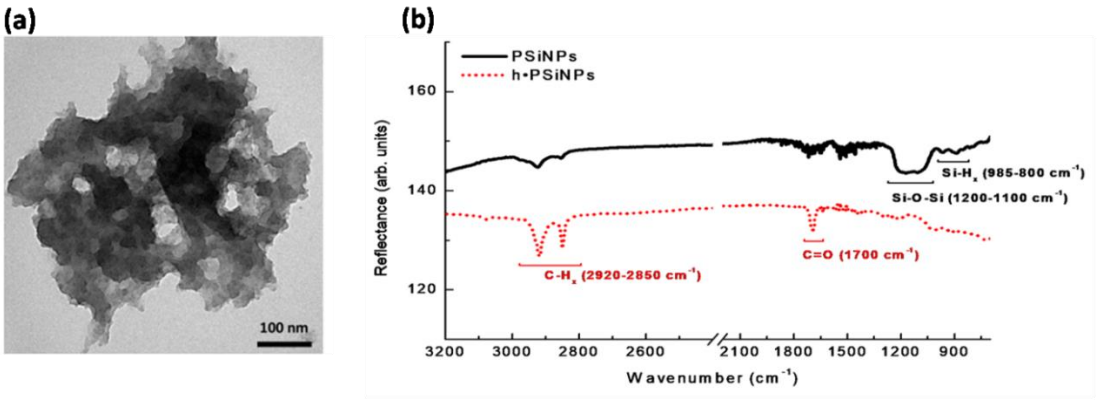

Figure 3 | 1. (a) TEM image of a single PSiNP. (b) FTIR spectra of PSiNPs before and after UA functionalization (the spectra were vertically shifted for clarity).

Hydrodynamic diameter (size) and surface charge (ζ potential) of (h)PSiNPs dispersed in deionized water (pH = 7) were estimated by Dynamic Light Scattering (DLS) using a Zetasizer Nano ZS (Malvern Instruments, U.K.) equipped with a He−Ne laser (633 nm), at fixed scattering angle of 173°, T = 25 °C. Results of DLS characterization are summarized in Table 1.

Material	**Size (nm)**	**ζ potential (mV)**
PSiNPs	420 ± 90	-0.3 ± 0.1
hPSiNPs	480 ± 70	-15 ± 4

Table 3 | 1. Measured size and ζ potential of PSiNPs and hPSiNPs dispersed in water (pH = 7).

According to TEM analysis, PSiNPs were characterized by a mean size of 420 nm, whereas, after surface modification with UA, the size of hPSiNPs was estimated to be 480 nm, comparable to that of bare PSiNPs within the experimental error. On the other hand, hydrosilylation strongly modified the surface charge of NPs: the absolute increase of the value of ζ potential, from -0.3 mV to -15 mV, can be ascribed to the presence of negatively charged carboxyl groups added subsequently to the functionalization. This result also indicated an increase of the repulsive electrostatic interaction between NPs and, as a consequence, a higher stability of hPSiNPs colloid.

3.1.2 Optical characterizations and stability in physiological medium

Steady-state and time-resolved photoluminescence analyses of bare and modified PSiNPs suspensions in IPA were performed in cuvette (1.3 mg/mL for PSiNPs and 0.9 mg/mL for hPSiNPs), exposing the samples to a LED pump (LLS, Ocean Optics, 365 nm). Emitted light was collected at 90° with respect to the pump through an optical fiber, dispersed in a spectrometer (ANDOR SR-163) and detected using an ANDOR iStar DH734 iCCD camera. For the stationary characterization, the LED pump was kept in continuous wave regime and the iCCD was set in internal trigger mode at 1 ms gate pulse width, whereas for time-resolved PL measurements, the pump and the iCCD were externally modulated via a Keysight 33220A pulse generator at a repetition rate of 500 Hz, 5 µs wide gate pulse width and at 10 µs steps. The intensity was integrated within 10 nm spectral intervals. In both analyses, a long-pass filter (nominal cut-on wavelength 410 nm) was used to remove undesired photons from the excitation source at the monochromator entrance. All the measurements were carried out at room temperature (T=25 °C).

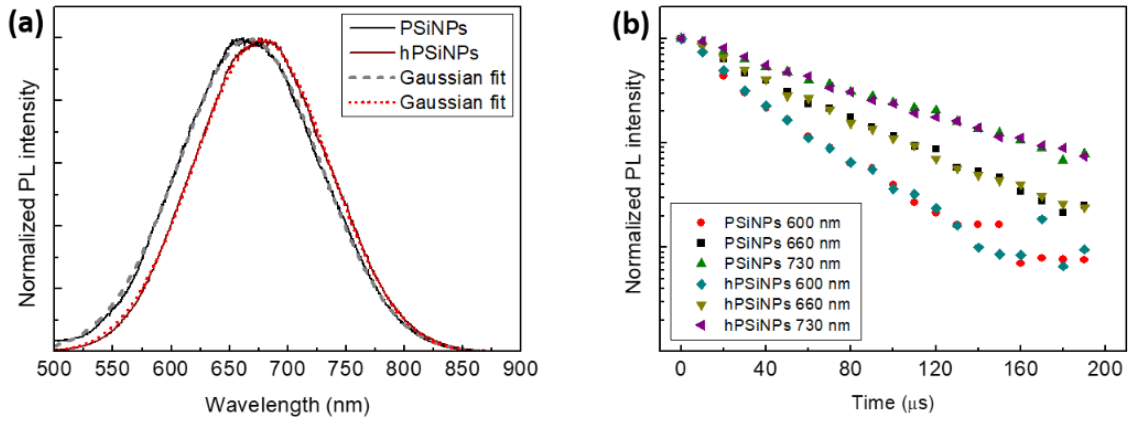

Figure 3 | 2. (a) Steady-state and (b) time-resolved PL measurements of PSiNPs and hPSiNPs in IPA at 365 nm excitation wavelength.

Normalized steady-state PL spectra of PSiNPs and hPSiNPs at λ_{exc} = 365 nm are reported in Figure 3 | 2(a): a typical Gaussian distribution between 500 and 900 nm was observed for both samples. Gaussian fits revealed that spectra of PSiNPs and hPSiNPs are centered at 667 nm and 677 nm, respectively. The red shift of 10 nm was imputed to the presence of UA in the nanometric pores of functionalized nanoparticles, which increased the average refractive index of the structures [74]. Steady-state PL spectra also evidence

the invariance in the emissive spectral behavior before and after functionalization, i.e. the increase of the PL lifetime at increasing wavelength coherent with the simultaneous obeying to the Fermi's golden rule ($1/\tau \propto E^2$) and the effect of size-dependent energy $E_{PL} = E_G + 3.73d^{-1.39}$ § due to quantum confinement [17] (E_G = 1.12 eV is the bandgap energy of bulk silicon [75]). The approximate expression § also allows to roughly estimate the mean value <*d*> of the Si nanocrystals size distribution: for hPSiNPs, <*d*> ~ 3 nm.

The stationary characterization was validated by time-resolved PL analysis. Radiative relaxation processes in porous silicon can be distinguished in two main classes: a fast decay with a lifetime of the order of ~10^{-9} s, and a slow decay, related to quantum-confined excitons in single Si nanocrystals, with characteristic times in the microsecond range (cf. Section 1.2.2). In the case of PSiNPs and hPSiNPs samples, the PL decay curves (Figure 3 | 2(b)) were in full agreement with a stretched exponential function, used to model the relaxation dynamics of complex systems [35] (cf. Section 1.2.3): $I(t) = I_0 e^{-\left(\frac{t}{\tau}\right)^{\beta}}$. This function represents a more accurate descriptive model with respect to the exponential law and depicts the PL emission behavior due to the dispersive diffusion phenomena of photoexcited carriers [35] and, in particular, the adimensional stretching factor β can be related to the characteristics of the environment surrounding the nano-emitters rather than their intrinsic crystalline structure, size and properties [31]: specifically, as already introduced in Section 1.2.3, β contains information about "the degree of disorder" of the system [35], i.e., phenomena which may be ascribed to the dispersive diffusion of the photoexcited carriers among the neighboring emissive sites, including transitions from localized to extended states or hopping between localized states. The localized states act as traps which are randomly distributed, on the single nanoparticle and either in the ensemble of NPs in the colloid. Such mechanisms mostly depend on the nanoparticle environment. In this frame, the slightly different values of β highlighted how the photo-physical properties of the nanocrystals on PSiNPs surface were fully maintained after UA conjugation. Moreover, the decay curves showed a dependence of PL lifetime on the emission wavelength, as predicted by the quantum confinement model [72], i.e. increasing decay times at longer emission wavelengths. The estimated values for τ and β did not substantially change for PSiNPs and hPSiNPs (Table 3 | 2). The almost single-exponential behavior of the decays in IPA reveals that the environment surrounding the single nanocrystal, at this stage (i.e., when the degradation processes at the nanoscale are absent

or follow a very slow dynamics) does not affect the transitions involved in the decay processes.

	600 nm		660 nm		730 nm	
Material	**τ (μs)**	**β (a.u.)**	**τ (μs)**	**β (a.u.)**	**τ (μs)**	**β (a.u.)**
PSiNPs	26.5±0.9	0.96±0.04	43±2	0.97±0.04	67±2	0.95±0.03
hPSiNPs	27.8±0.7	1.01±0.03	44±1	1.01±0.03	68±2	1.02±0.04

Table 3 | 2. Lifetimes (τ) and dispersion factors (β) of (h)PSiNPs samples at different emission wavelengths.

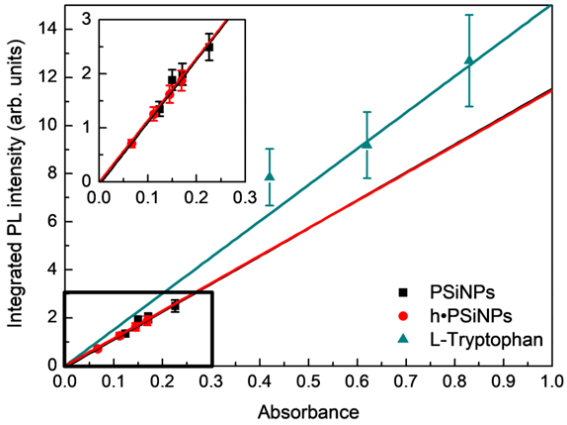

Figure 3 | 3. Plots of the integrated PL intensity versus absorbance (at 265 nm excitation) at different (h)PSiNPs samples concentration. The slopes of the fitted lines were used to calculate the QY of PSiNPs and hPSiNPs dispersed in IPA. The same plot for L-Tryptophan is herein reported as reference.

PL quantum yields (QYs) of nanoparticles in IPA were determined by measuring absorbance (A) and integrated PL intensity (I), in the interval 550-700 nm, at different material concentrations, at fixed excitation wavelength λ_{exc} = 265 nm. UV-Vis absorbance curves were obtained by using a Cary 100 spectrophotometer (VARIAN), whereas the emitted light was registered with a JASCO FP-8200 spectrofluorometer.

The PL spectra, in the investigated excitation spectral region, showed a slight modification in the shape probably due to the local interactions between the UA anchored on hPSiNPs surface and the IPA medium [76] (data not shown). QYs were estimated relative to L-Tryptophan (L-Trypt) used as standard dye (QYL-Trypt in water of (15±1)%,

absolute measurement done with an integrating sphere [77]) and calculated by the following equation [78]:

$$\left.\frac{QY_{NPs}}{n_{IPA}^2 \alpha_{NPs}}\right|_{\lambda_{exc}} = \left.\frac{QY_{L-T}}{n_{H_2O}^2 \alpha_{L-T}}\right|_{\lambda_{exc}}$$

where n^2 are the squared refractive indices of the media (H_2O or IPA) and α represents the ratio between integrated PL intensity and absorbance, I/A, at λ = 265 nm. The coefficients $\alpha_{PSiNPs} = (1.1 \pm 0.3)\cdot 10^5$ and $\alpha_{hPSiNPs} = (1.2 \pm 0.2)\cdot 10^5$ were obtained via linear regression from the plots of I versus A for PSiNPs and hPSiNPs, respectively (Figure 3 | 3). The coefficient $\alpha_{L\text{-}Trypt} = (1.5 \pm 0.2)\cdot 10^5$ was calculated for L-Trypt in water. Using $n_{IPA} = 1.422$ and $n_{H2O} = 1.357$ as refractive indices for IPA and water respectively (at 265 nm), QY values equal to 12 ± 5% and 13 ± 5% were determined. Since the QY was very similar for PSiNPs and hPSiNPs, it was confirmed that the UA passivation procedure fully preserved the surface nature and crystalline structure of NPs and, consequently, their PL behavior in terms of global emission.

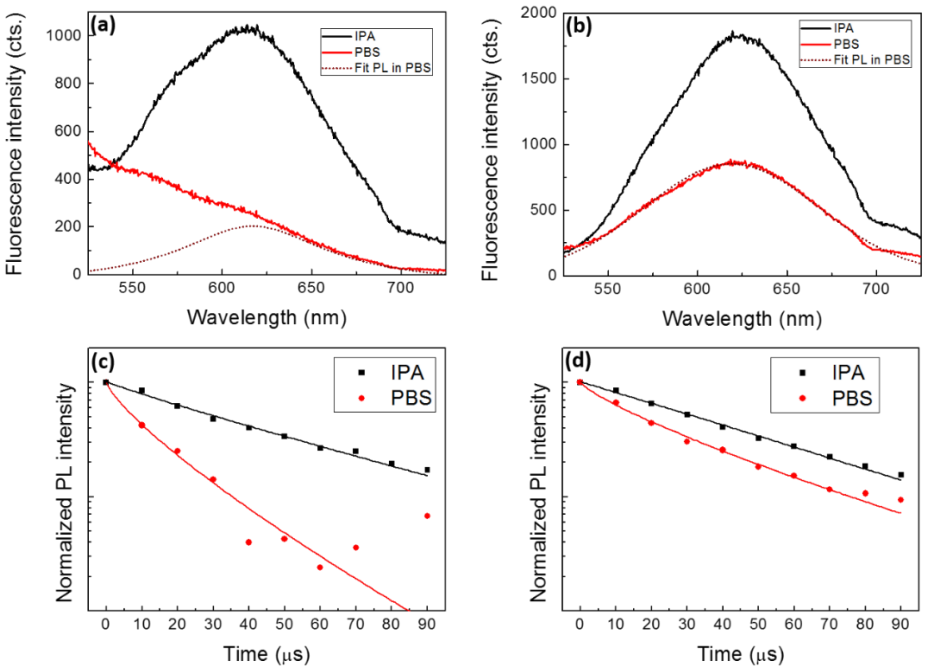

Figure 3 | 4. PL spectra of (a) PSiNPs and (b) hPSiNPs in different media: the almost instantaneous quantum-confined PL signal extinction of bare PSiNPs is clearly evidenced. (c) and (d) report the average PL decays in IPA compared to PBS of PSiNPs and hPSiNPs, respectively.

In order to probe the surface functionalization effectiveness under physiological conditions, PSiNPs and hPSiNPs stored in IPA were re-suspended in Phosphate Buffer Saline (PBS) 0.1 M, at pH = 7.4. In order to disclose the influence of the physiological medium on the photophysical properties of the materials, the PL spectra of (h)PSiNPs samples were compared to the corresponding curves in IPA at an excitation wavelength of 365 nm, as highlighted in Figure 3 | 4(a,b). Notably, the shape of the PL spectrum of PSiNPs dramatically changed due to the fast degradation of the quantum-confined nanocrystals into oxide-related radiative sites. Besides, time-resolved PL measurements of PSiNPs and hPSiNPs in PBS (pH = 7.4) at room temperature showed the crucial influence of the physiological environment on the optical properties of the investigated materials. In this frame, the average quantities $<\tau>$ and $<\beta>$ were introduced by integrating the whole PL spectra and plotting the corresponding decay. In particular, bare nanoparticles degraded almost instantaneously, with a percentage decrease of $<\tau>$ of ~70% (Figure 3 | 4(c), from 45(2) to 12(1) μs), when hPSiNPs underwent a slight lowering (~40%, from 46(1) to 27(1) μs, Figure 3 | 4(d)) and exhibited a slower degradation kinetics (as will be better discussed shortly afterwards). The stretching factor $<\beta>$ also resulted decreasing from 0.92(7) to 0.79(8) for PSiNPs and from 1.02(4) to 0.80(4) for hPSiNPs. Such evidence is mathematically consistent with a broadening of the lifetime distribution [79], giving symptom of a modification of the radiative relaxation channels.

t_{incub} (h) / λ_{em} (nm)		**IPA**	0	1	2	4
600	τ (μs)	**27.8(7)**	15.8(1)	18(2)	15.0(7)	16.5(7)
	β(au)	**1.01(3)**	0.96(4)	1.0(1)	0.87(4)	0.86(5)
660	τ (μs)	**44(1)**	26(1)	26.6(9)	23.1(8)	21.5(7)
	β(au)	**1.01(3)**	0.83(5)	0.86(4)	0.87(4)	0.77(3)
730	τ (μs)	**68(2)**	35(2)	33(3)	27(2)	26(1)
	β(au)	**1.02(4)**	0.76(4)	0.81(8)	0.76(6)	0.75(5)

Table 3 | 3. τ and β values at different emission wavelengths, monitored as a function of the incubation time in PBS. The values in IPA are a recall to Table 3 | 2.

τ and β at different emission wavelengths for hPSiNPs were also monitored at different incubation times in PBS for up to 4 h (Table 3 | 3). The samples were suspended

in PBS and put under gentle agitation at room temperature. As can be seen, bigger size nanocrystals were reported to be more influenced by the incubation in PBS; in fact, the relative variation of the lifetimes increased at increasing excitation wavelength when the medium is changed from IPA to PBS ($\Delta\tau/\tau|_{730\ nm}$ = 49% versus $\Delta\tau/\tau|_{600\ nm}$ = 5%). The same trend, despite less noticeable, was reported for the β behavior.

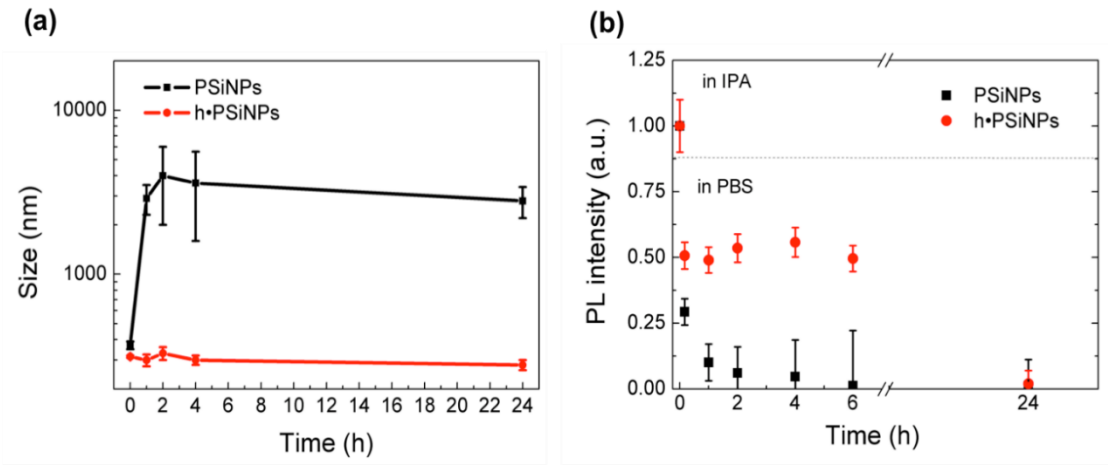

Figure 3 | 5. (a) Morphological and (b) integrated fluorescence stability of (h)PSiNPs samples at different incubation times in PBS.

The size of NPs was also monitored by DLS at different incubation times in PBS. After 1 h, significant aggregation was evidenced for bare PSiNPs, since the instrumental measured size value was well above the micron range. In the same conditions, hPSiNPs preserved their nanometric size for up to 24 h observation without evidencing any substantial change. The temporal behavior of (h)PSiNPs samples' size in PBS is reported in Figure 3 | 5(a). Besides, Figure 3 | 5(b) reports the integrated PL intensity of PSiNPs and hPSiNPs (in the 550-700 nm interval) measured after different incubation times in PBS. The PL emission of bare PSiNPs was strongly affected by exposure to the PBS environment and decreased by 94% in 2 h (black squares in Figure 3 | 5(b)). This effect could be a severe limitation to the use of PSiNPs as luminescent probes in bioimaging experiments, where the diffusion of the probes within the tissues could last several hours. Much better stability was obtained in the case of hPSiNPs: PL intensity was attenuated by only 50% of its value in IPA once placed in the PBS medium (Figure 3 | 5(b)), then remained constant for at least the following 6 h, as it can be seen in Figure 3 | 5(b) (red dots). Anyway, for both PSiNPs and hPSiNPs, no emitted light was observed after 24 h incubation. The PL quenching was

mainly due to the progressive bulk transformation of the silicon nanocrystals into silicon oxide nanostructures, which were not emissive at the same wavelength. On the other hand, the size of the nanoparticles was preserved by surface charge so that the observed quenching dynamic was disjointed from the overall stability of the colloid.

In conclusion, the experimental results demonstrated that hydrosilylation, leading to covalent UA conjugation, is an effective method to preserve morphology of PSiNPs and stabilize the emission properties up to 6 h in simulated biological conditions, preventing the uncontrolled degradation of the material. The unsusual long-lived emission from quantum-confined Si nanostructures represents a key feature that will be exploited for the implementation of time-gated fluorescence imaging *in vivo*, as will be extensively discussed in Chapter IV.

3.1.3 Poly-L-lysine conjugation to UA-functionalized PSiNPs

Hydrosilylated PSiNPs exhibit a negative surface charge due to the exposure of the UA carboxyl groups. Despite conferring a major stability to the colloidal suspension, this still represent a limitation when pursuing a study on the interactions with biological systems. In fact, the phospholipidic layer of cellular membranes usually exposes negative groups as well [80]. Therefore, interaction/internalization processes are intrinsically inhibited by electrostatic repulsion. In order to overcome this issue, hPSiNPs were further conjugated with poly-L-lysine (PLL – formula $(C_6H_{12}N_2O)_n$), a positively charged amino acid polymer commonly used to enhance cells adhesion onto solid substrates [81].

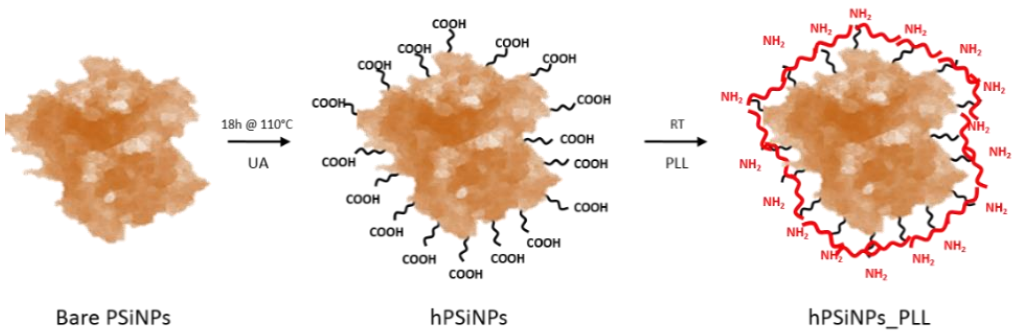

Figure 3 | 6. Outline of the whole PSiNPs functionalization process. The hydrosilylation reaction was already described in detail in Section 3.1.1.

PLL conjugation is herein reached via electrostatic interaction (Figure 3 | 6). PLL solution 0.1% (w/v) in H_2O was purchased from Sigma-Aldrich. PSiNPs fabrication and their hydrosilylation with UA followed the same protocol illustrated in Section 3.1.1. In order to pursue an effective coverage of their high surface area, hPSiNPs and PLL were allowed to react at a mass ratio 1:1 at RT under mild agitation for 30 mins at a pH ~ 5. The sample was extensively washed in ultrapure MilliQ water at the same pH range to remove PLL in excess. Finally, PLL-conjugated hPSiNPs (hPSiNPs_PLL) were resuspended in the desired medium (water or buffer for *in vivo* experiments) at pH 6 and characterized.

The as-prepared sample was examined via DLS (hydrodynamic diameter and ζ potential – Zetasizer Nano ZS, Malvern Instruments) and steady-state PL spectroscopy. To the latter aim, the samples were put in a quartz cuvette and exposed to continuous He-Cd laser pump (KIMMON Laser System, excitation wavelength 325 nm). Emitted light was collected at 90° with respect to the pump through an optical fiber, dispersed in a spectrometer (Princeton Instruments, SpectraPro 300i) and detected using a Peltier-cooled CCD camera (PIXIS 100F). A long-pass filter with a nominal cut-on wavelength of 350 nm was used to remove the laser line at the monochromator inlet.

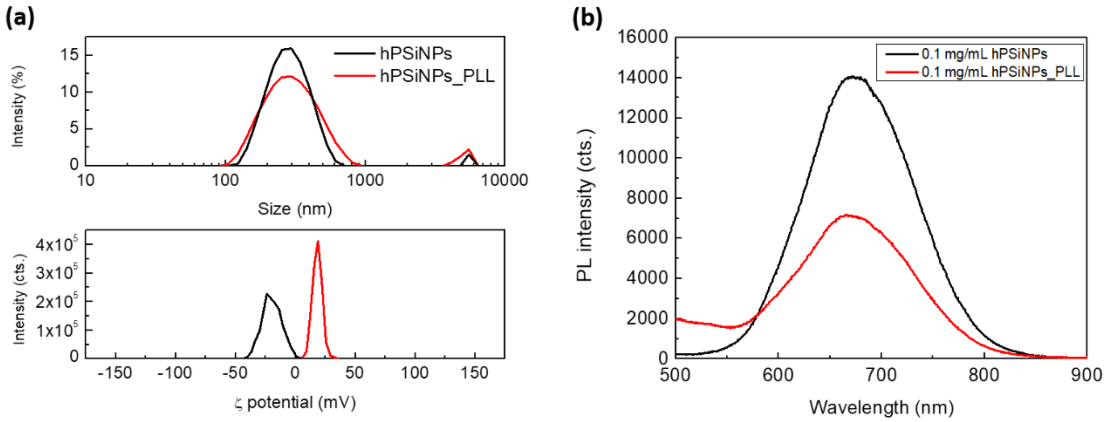

Figure 3 | 7. (a) DLS (hydrodynamic diameter and ζ potential) of hPSiNPs before and after PLL conjugation. (b) Steady-state PL spectra at 325 nm excitation of hPSiNPs(_PLL) samples at the same concentration.

An invariance in the hydrodynamic diameter, except for a slight increase of the polydispersity index (from 0.26 ± 0.04 to 0.4 ± 0.1) was observed after PLL conjugation, confirming an effective coverage of hPSiNPs rather than formation of polymeric agglomerates. Significantly, the ζ potential of hPSiNPs_PLL was succesfully tuned from -

15.8(0.4) to +16(4) mV thanks to the exposure of PLL positively charged amine groups (Figure 3 | 7(a)). From the optical point of view, a partial oxidation of the material and a consequent induced PL quenching was observed (Figure 3 | 7(b)); such phenomenon could be ascribed to an incomplete Si-C surface passivation after the hydrosilylation treatment. This evidence implies a decrease in the PL QY. Such variation was estimated by integrating and comparing the PL signal in two samples at the exact same PSiNPs concentration in the spectral range of interest, by virtue of the proportionality relation between QY and I: in particular, a 45% decrease was registered, thus resulting in a QY lowering from 13% (cf. Section 3.1.2) to ~8%, which still represents an acceptable value for the usage of hPSiNPs_PLL as luminescent probes for bioimaging [82] (cf. Chapter IV).

3.2 On-chip porous silicon/graphene oxide nanocomposite

A chemical procedure to covalently bind GO to a PSi surface has been developed in order to realize a stable hybrid device for biosensing purposes. A single-layer macroporous silicon matrix has been engineered by infiltrating GO nanosheets inside the pores of the PSi platform. Such PSi/GO hybrid device has then been covalently conjugated to FITC-labeled protein A (PrA^*) derived from *Staphylococcus aureus*, employed as model bioprobe. The effective covalent interaction between PSi/GO and PrA^* demonstrates the possibility to realize a robust system for biosensing whose operating mechanism could be based on the changes of PSi reflectance spectrum and GO photoluminescence.

3.2.1 Steady-state and time-resolved photoluminescence characterizations

GO photoluminescence exhibits specific features: excitation-dependent spectral emission and ns-range PL lifetime [42]. Such properties were preliminarily analyzed with both steady-state (at different excitations) and time-resolved photoluminescence characterizations (Figure 3 | 8).

One of the most utilized methods to determine short-lived fluorescence components is Time-Correlated Single Photon Counting (TCSPC). The method is based on the repetitive, precisely timed registration of single photons of a fluorescence signal. The reference for the timing is the corresponding excitation pulse. With periodic excitation, e.g., from a laser, it is possible to extend the data collection over multiple cycles of excitation

and emission. One can then reconstruct the fluorescence decay profile from the multitude of single photon events collected over many cycles. To do so, single-photon sensitive detectors like Photomultiplier Tubes (PMTs) can be used [83].

However, it is important to underline that the excitation pulse is not a delta function and the instrumentation additionally has a certain electronic response time. All these parameters are quantified by the instrument response function (IRF) which is the response profile of the instrument to a purely scattering solution [84]. Thus, the real registered signal is the convolution of such IRF and the actual fluorescence decay:

$$N(t) = (I * IRF)(t) = \int_0^t I(t - t')IRF(t')dt'.$$

The main task in TCSPC analyses is to determine the model, I(t), which yields the best overall fit between N(t) and IRF(t). A good fit is characterized by a value of reduced chi-square close to 1, with such quantity being defined as

$$\chi_R^2 = \left[\sum_{k=1}^{n} \frac{\left(N(t_k) - N_{fit}(t_k)\right)^2}{N(t_k)}\right] \times \frac{1}{n}.$$

A GO nanosheets aqueous suspension (1 mg/mL) was put in a quartz cuvette for both steady-state and time-resolved analyses. TCSPC measurements were performed employing a picosecond diode laser (LDH-P-C-405B, PicoQuant) as excitation source, emitting pulses at 40 MHz repetition rate and 405 nm emission wavelength. The laser beam was focused into a 10 mm sample cell with a proper lens. The emitted light was acquired at 90° with respect to the incident beam to minimize undesired transmitted or reflected light and collected with optical fiber. An Asahi ZBPA410 long-pass filter (nominal cut-on wavelength 410 nm) was used to block the excitation. The detection apparatus was composed of a PMT module (H9305-03, Hamamatsu, Tokyo, Japan) and a TCSPC electronic board (SPC130M, Becker and Hickl GmbH, Berlin, Germany). The instrument response function (IRF) determined by TCSPC was about 410 ps FWHM. The data were analyzed with DecayFit software (FluorTools.com).

In the examined case, the comparable temporal width of IRF and PL decay, as well as the extremely weak PL signal from GO (which remarkably lengthened the acquisition

time) led to an unoptimized measurement, in which the most acceptable accordance occurred by modeling with a single-exponential decay with $\tau = 620 \pm 40$ ps and a $\chi^2 = 4.5$. Such value is consistent with the average value reported in the literature [39]. Despite being preliminary data, the evidences were sufficient to establish the surface-defects-like nature of GO PL nanosheets rather than quantum confinement phenomena, since the measured τ resulted independent from the examined emission wavelength (Figure 3 | 8(b)).

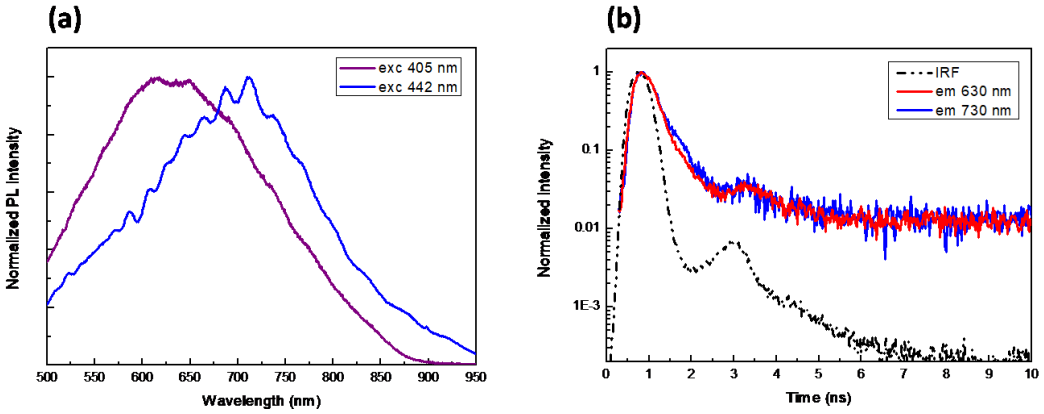

Figure 3 | 8. (a) Steady-state PL spectra of GO in H_2O at 405 nm and 442 nm excitation wavelengths. (b) TCSPC histogram of GO PL decay at 405 nm pulsed excitation, at 630 nm and 730 nm emissions.

3.2.2 Fabrication of the PSi/GO hybrid chip

Hydrofluoric acid (HF), undecylenic acid (UA), N-(3- Dimethylaminopropyl)-N'-ethylcarbodiimide hydrochloride (EDC), N-hydroxysuccinimide (NHS), 2-(N-morpholino)ethanesulfonic acid (MES) hydrate, tert- Butyloxycarbonyl-NH-PEG-Amine (BOC-NH-PEG-NH_2), trifluoroacetic acid (TFA), chloroform, tetrahydrofuran, FITC-labeled Protein A (PrA*) from *S. aureus* were purchased from Sigma Aldrich (St. Louis, MO, USA). GO nanosheets were purchased from Biotool.com (Houston, TX, USA) as a batch of 2 mg/mL in water with a nominal sheets size between 50 and 200 nm.

Before infiltration, GO at 1 mg/mL concentration was sonicated using an ultrasonic processor for 1 h in ice at 50% of available power amplitude, aiming at obtaining a nanosheets size lower than 100 nm (probed via DLS). The Fabry-Pérot PSi structure was fabricated by electrochemical etching of n-type crystalline silicon (0.01–0.02 Ω cm resistivity, <100> oriented and 500 μm thick) in HF (5% in weight)/ethanol solution at

room temperature (RT). Before the etching process, the silicon substrate was immersed in the same HF solution for 2 min to remove the oxide native layer. A current density of 20 mA cm^{-2} for 90 s was applied to obtain a single macroporous layer with a porosity of 61% (n_{PSi} = 1.83 at λ = 1.2 μm), a thickness L of 2.1 μm and a pore average dimension between 50 and 250 nm as determined previously [85].

The as-etched PSi chip was placed in a Schlenk tube containing deoxygenated neat UA (99% v/v) and allowed to react at 110 °C for 18 h in Ar atmosphere [86]. After extensive washing in tetrahydrofuran and chloroform, UA-modified PSi was placed in a Schlenk tube containing freshly prepared EDC/NHS aqueous mixture (0.005M in MES buffer 0.1 M) for 90 min at RT to allow the UA carboxyl groups activation. PEGylation was performed dipping the sample in BOC-NHPEG-NH_2 solution (0.4 M, overnight, at 4 °C) [87], [88]; the t-butyloxycarbonyl (BOC) protecting group of amine portion was removed from the PEG covalently bound to PSi surface via acid hydrolysis incubating the sample in a solution of TFA (95% v/v, 90 min, at RT). The sample was then washed in deionized water so as to remove the excess of TFA. The covalent anchoring of GO nanosheets within the porous matrix was performed incubating the sample in the sonicated GO suspension (1 mg/mL) in presence of EDC/NHS (0.020M EDC and 0.016M NHS in MES 0.1 M, overnight, at RT). Finally, the GO-modified PSi chip was incubated in 0.33 mg/mL of PrA^* in presence of EDC/NHS (0.020M EDC and0.016M NHS in MES 0.1 M, overnight, at RT). The whole process is graphically summarized in Figure 3 | 9.

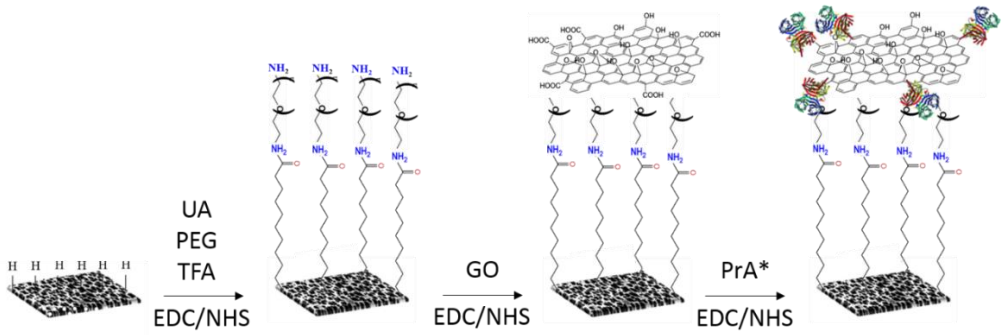

Figure 3 | 9. Summary of the chemical steps for achieving covalent GO and PrA* anchoring onto PSi surface.

3.2.3 PSi/GO hybrid chip characterization

The optical spectrum of a PSi monolayer consists of a fringe pattern due to interference occurring at air/PSi and PSi/bulk crystalline silicon interfaces. In other words, the PSi layer optically acts as a Fabry-Pérot interferometer, whose reflectance can be expressed as a function of the incident wavelength as [89]

$$R(\lambda) = r_1^2 + r_2^2 + 2r_1 r_2 \cos\left[2\pi\left(\frac{2n_{PSi}L}{\lambda}\right)\right],$$

where $r_1 = (n_{\mathrm{Air}} - n_{\mathrm{PSi}})/(n_{\mathrm{Air}} + n_{\mathrm{PSi}})$ is the Fresnel reflection coefficient at air/PSi interface, $r_2 = (n_{\mathrm{PSi}} - n_{\mathrm{Si}})/(n_{\mathrm{PSi}} + n_{\mathrm{Si}})$ is the same quantity at PSi/crystalline silicon interface, L is the thickness of the PSi layer, λ is the wavelength, and n_{Air}, n_{PSi}, and n_{Si} are the refractive indices of air, PSi, and bulk silicon, respectively. The optical thickness (n_{PSi}L) of the PSi layer can be calculated from the reflectivity spectrum by counting the fringe maxima, which satisfy the relationship $m\lambda = 2n_{\mathrm{PSi}}\mathrm{L}$ (where m is an integer and λ is the wavelength of the incident light) [90].

From the material point of view, the chemical functionalization and subsequent bioprobe conjugation are additive processes. This implies that the optical thickness (i.e., the product of physical thickness, which is fixed, by the average refractive index n of the porous matrix, which varies instead) of the obtained PSi/GO hybrid device is expected to progressively increase. The reflectance spectra of PSi sample were monitored throughout the whole functionalization process and measured at normal incidence by means of a Y optical reflection probe (Avantes) connected to a white light source and to an optical spectrum analyzer (Ando, AQ6315B). The spectra were collected over the 600-1600 nm range with 1 nm resolution. The spectra shown herein are the average on three measurements. As can be noticed, an increasing red shift resulted from a progressive pore filling. However, this evaluation is almost of qualitative nature. Also, the intermediate functionalization steps may not be immediately visualized due to the extremely low thickness of the capping reagents UA and PEG passivating the PSi surface.

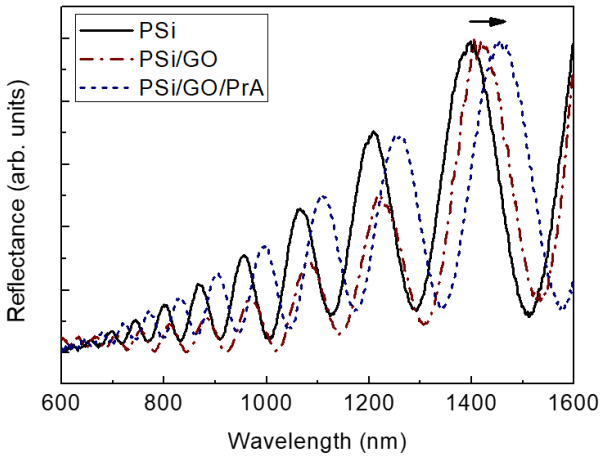

Figure 3 | 10. Progressive red shift in the optical spectrum of the Fabry-Pérot photonic PSi structure after GO (dash-dotted dark red line) and PrA* (dotted blue line) due to the increase of the refractive index within the porous matrix after infiltration.

A more straightforward method for quantitatively evidencing changes in the optical path is based on the fast Fourier transform (FFT) of PSi optical spectrum, which basically is a broad, single-harmonic peak function. In particular, the FFT peak position along the x-axis corresponds to two times the optical thickness (2OT) of the layer [89]. The FFTs of the normal incidence reflectance spectra of PSi before and after hydrosilylation and PEGylation process show a peak shift of about 90 nm and 145 nm, respectively. Since the physical thickness of the PSi layer was fixed, such shifts could only be due to the increase of the average refractive index of the composite material. This result clearly indicated that the two chemical functionalization steps added material layers within the PSi matrix. Besides, the reflectance spectrum as well as the FFT after the removal of the BOC protector group displayed a blue shift (-100 nm). Such evidence is consequence of the optimized acid hydrolysis process that partially “emptied” the pores (data not shown). Finally, the GO functionalization and the PrA* conjugation steps are reported in Figure 3 | 12 (such FFTs are referred to the optical spectra reported in Figure 3 | 11): the FFT peak shift of 90 nm after GO grafting and the remarkable further red shift of 275 nm after PrA* anchoring constituted a clear evidence of the occurred functionalization. Nevertheless, no significant changes were detected in negative control samples.

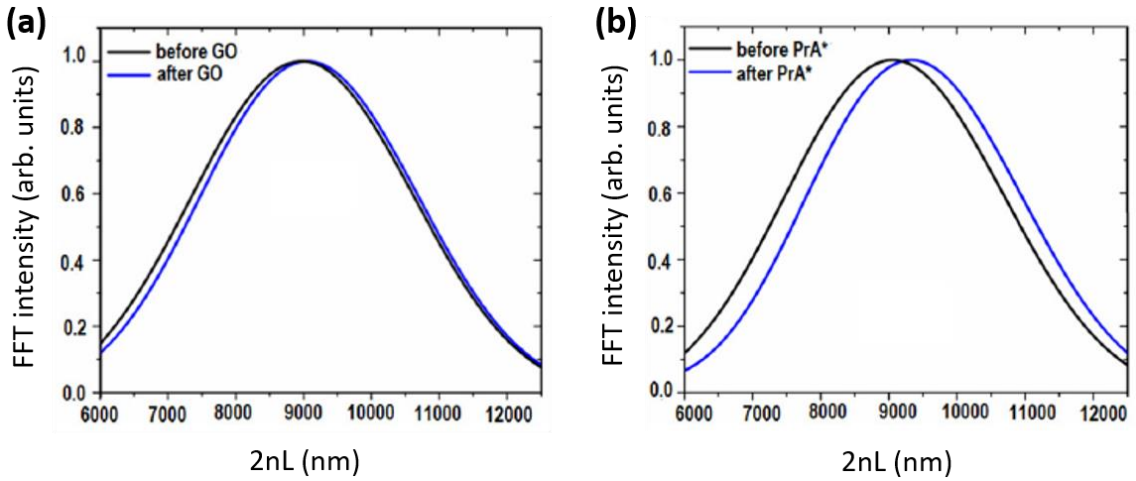

Figure 3 | 11. FFTs of reflectance spectra reveal a progressive red shift (a) after GO infiltration and (b) after PrA* grafting.

The infiltration of GO within the PSi layer was also analyzed by steady-state photoluminescence spectroscopy. Steady-state PL spectra were excited by a continuous wave He-Cd laser at 442 nm (KIMMON Laser System). Emitted light was collected at normal incidence to the surface of samples through a fiber, dispersed in a spectrometer (Princeton Instruments, SpectraPro 300i), and detected using a Peltier-cooled charge CCD camera (PIXIS 100F). A long-pass filter with a nominal cut-on wavelength of 458 nm was used to remove the laser line at the monochromator inlet. As can be evidenced in Figure 3 | 12(a), no PL signal could be detected in the case of bare PSi, whereas the covalent grafting of GO was revealed by a modulation of the PL signal. The experimental evidence of such phenomenon was already demonstrated in a previous work [90]: the modulation of PL intensity can be explained by considering once more the optical behavior of a Fabry-Pérot interferometer: among all the wavelengths λ_{em} emitted by GO infiltrated inside the PSi structure only those fulfilling the relationship $2n_{PSi}L = m\lambda_{em}$, with $2n_{PSi}L$ being the optical thickness of the PSi layer and m integer, could constructively interfere producing maxima in the PL spectrum of the hybrid structure. Figure 3 | 12(b) shows a comparison between PL and reflectance spectra of the GO-infiltrated PSi monolayer: the distance between two consecutive PL maxima was about 67 nm, which well matched the free spectral range of the PSi/GO photonic structure. Finally, the concentration of GO covalently conjugated to PSi was estimated to be ~7.5 μg/mL; this value was obtained by comparing the recorded PL intensity of PSi/GO device with those of aqueous GO solutions at different concentrations.

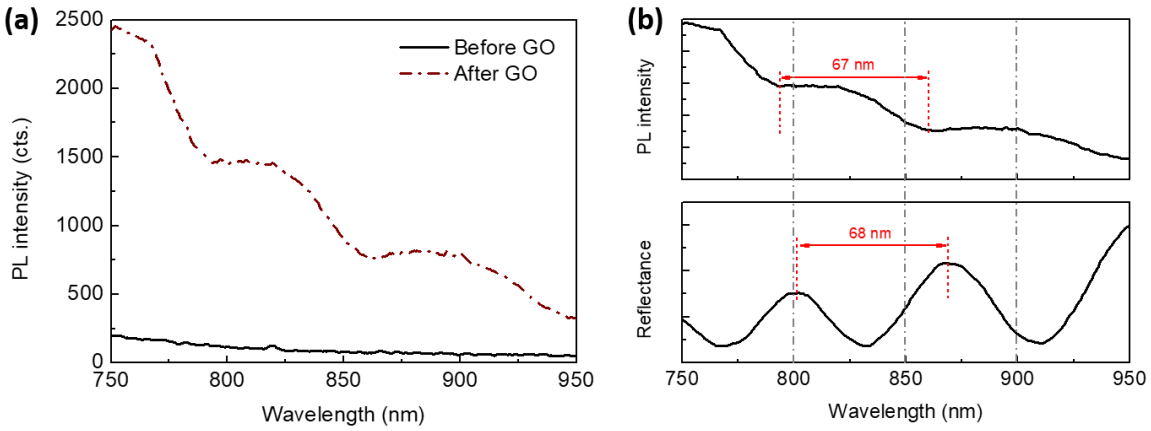

Figure 3 | 12. (a) Steady-state PL spectrum of PSi surface before and after GO infiltration. (b) Comparison between the same PL spectrum with the interference pattern of the Fabry-Pérot PSi photonic structure.

Morphological features of the surface were highlighted by AFM (Figure 3 | 13). A XE-100 AFM (Park Systems) was used for the imaging of PSi sample before and after functionalization with GO and PrA*. Surface imaging was obtained in non-contact mode using silicon/aluminum coated cantilevers (PPP-NCHR 10 M; Park Systems) 125 μm long with resonance frequency of 200 to 400 kHz and nominal force constant of 42 N/m. The scan frequency was typically 1 Hz per line. AFM images were analyzed by the program XEI 1.8.1 build 214 (Park Systems). The 3D topography image of bare PSi revealed the presence of hillocks and voids of about 100 nm uniformly distributed throughout the whole surface (Figure 3 | 13(a,b)); partial pore blocking was evidenced after the functionalization of the PSi chip with GO due to the presence of bigger-sized nanosheets on the PSi surface (Figure 3 | 13(c,d)) and further coverage of the surface was visible after PrA∗ bioconjugation (Figure 3 | 13(e,f)). The roughness of the sample surfaces were progressively calculated leading to values of roughness statistical media (Rsm) equal to 0.22 ± 0.01 μm for pristine PSi sample, Rsm = 0.45 ± 0.03 μm after GO, and Rsm = 0.34 ± 0.02 μm after PrA*.The final PSi/GO/PrA* hybrid device had an almost covered surface and partially blocked pores.

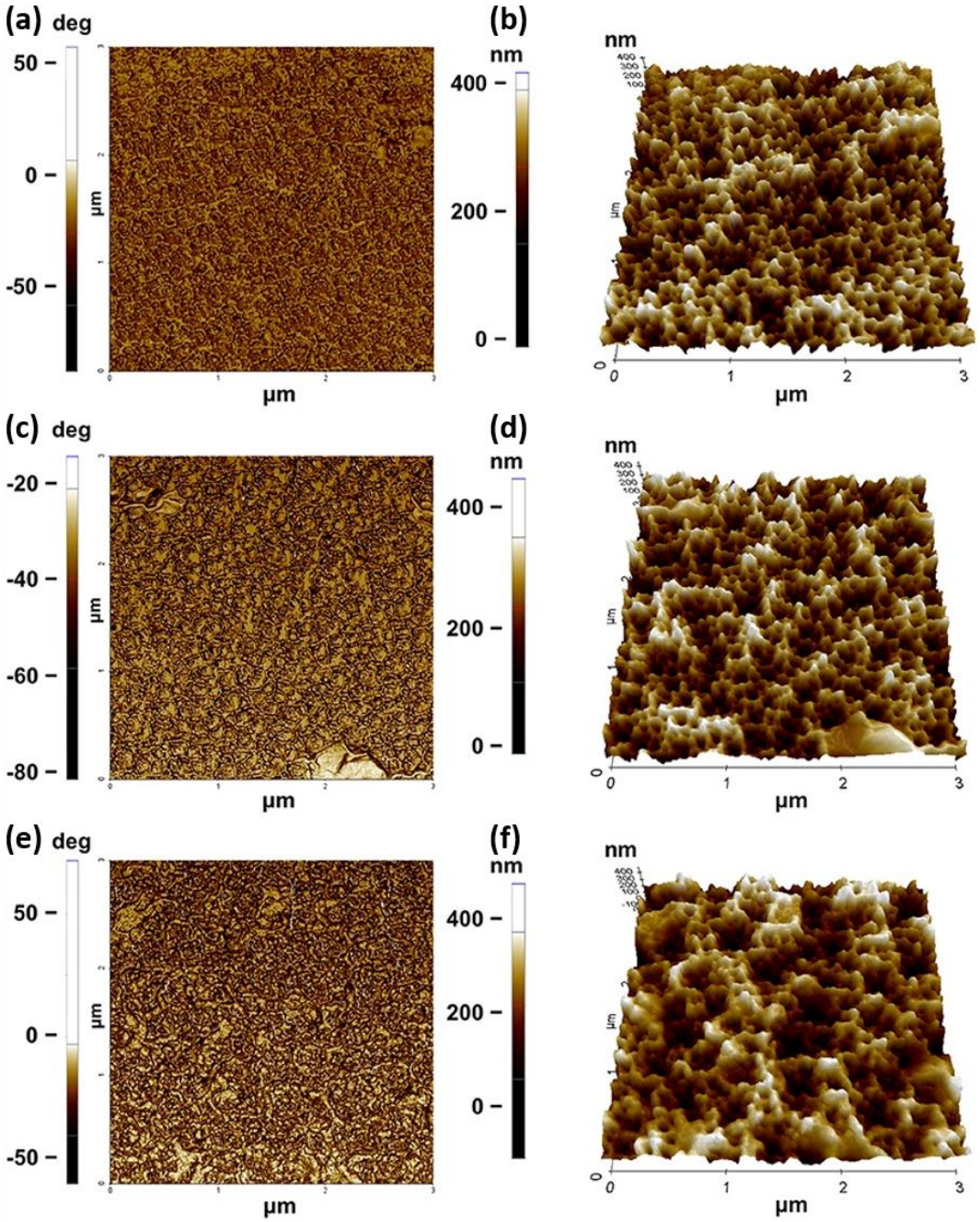

Figure 3 | 13. Phase and 3D topography AFM images of PSi chip: after etching ((a) and (b)); after GO infiltration ((c) and (d) – bigger size nanosheets can be visualized) and after PrA* anchoring ((e) and (f)).

Confocal fluorescence microscopy was used for a deeper characterization of the PrA* infiltration process. In particular, Figure 3 | 14(a) shows the 3D representation of all the recorded focal planes. In case of the negative control, the corresponding 3D image was completely dark and there was no evidence of nonspecific absorption onto the sample surface, thus confirming the covalent bioconjugation of PrA*. Figure 3 | 14(b) shows the

sequence of the single focal planes of the PrA*-infiltrated PSi monolayer, with the first image being the one of the chip surface and the last being the bottom of the porous layer. Figure 3 | 14(c) quantifies the average integrated fluorescence intensity profiles and, as can be clearly seen, the labeled protein signal followed a Gaussian distribution along the z axis having its maximum value close to the center of the layer. This result further confirms the protein penetration within the pores [91].

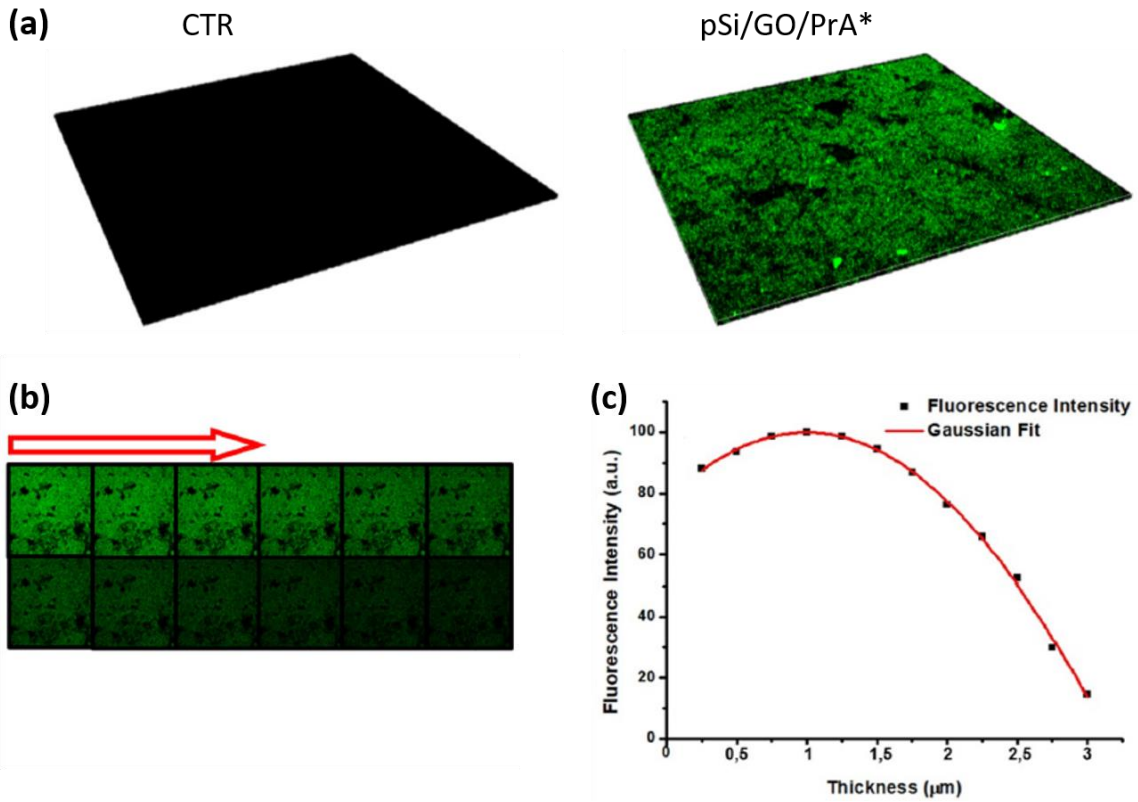

Figure 3 | 14. (a) Sum of all focal planes of negative control and PrA*-infiltrated PSi/GO chip. (b) Sequence of fluorescence images of PrA*-infiltrated PSi starting from to the PSi surface down to the bottom of the porous layer. (c) Profile of the averaged fluorescence intensities of the same sample along the z axis. Herein, a 3 μm-thick PSi chip was analyzed.

To conclude, a chemical procedure to covalently bind GO to PSi surface was developed in order to realize a stable hybrid device for biosensing purposes. A macroporous Si monolayer, characterized by a pore size > 50 nm, was employed for GO nanosheets infiltration within the porous matrix. The PSi/GO hybrid device was covalently conjugated to PrA* derived from *S. aureus*, used as model bioprobe. EDC/NHS coupling chemistry was successfully exploited to achieve a GO grafting to PSi and PrA* anchoring to the

PSi/GO matrix. AFM and confocal fluorescence imaging revealed the main morphological features of the composite structure. In addition, an unlabeled biorecognition element belonging to another typology, a PNA sequence for DNA point-mutations detection, was effectively conjugated to the PSi/GO device following the same chemical approach. The trackable probe anchoring-induced photoluminescence quenching allowed to estimate the probe concentration correspondent to the optimized surface coverage. Changes in the Fabry-Pérot interference pattern of the PSi photonic structure and in photoluminescence intensity have been exploited to characterize the fabrication process but also revealed their potential as transducing features. The results highlighted promising performances and pave the way to the development of innovative biosensors with multi-parametric operating mechanism, as will be better outlined in Chapter V (cf. Section 5.1).

3.3 Nanostructured fluorine-doped ZnO

One of the key issues to be addressed in the development of robust and reliable biosensing devices is represented by the choice of the functionalization strategy in order to correctly immobilize the bioprobes on the substrate surface. From this point of view, ZnO nanostructures have displayed their potential in allowing covalent binding of biomolecules on the surface preserving their specific functionalities and, at the same time, controlling their orientation. In that, the use of ZnO nanowires obtained by the hydrothermal method as a photoluminescent biosensor was demonstrated [92].

Contextually, doping ions play a significant role in the morphological, electrical and optical properties of nanostructured ZnO [93]. In particular, extensive studies demonstrated that fluorine atoms mainly occupy oxygen vacancies present in the material, without producing any substantial change of plasma frequency but only the enhancement of scattering rate due to an increase of grain boundary density [94]. Herein, nanostructured pristine (nZnO) and fluorine (F)-doped ZnO (nZnO-F) were directly grown on a crystalline silicon substrate via hydrothermal synthesis, and chemically modified in order to fabricate a technological platform for optical biosensing purposes. Interestingly, the results reveal an enhancement in the response of nZnO-F-based structure with respect to the undoped one.

3.3.1 Fabrication and functionalization of ZnO(-F) nanostructures

Nanostructured undoped and F-doped ZnO films were prepared following a hydrothermal route [94]. All reagents herein employed were purchased from Sigma-Aldrich. A solution containing a 1:1 molar ratio of triethylamine (TEA) and zinc acetate dihydrate (ZAD) was firstly prepared by mixing TEA (0.21 mL) and ZAD (0.33 g) into ethanol (90 mL) under constant stirring. After complete dissolution of ZAD, water (10 mL) was added dropwise, producing a whitish suspension which was transferred within a Teflon recipient (with the liquid volume corresponding to 75% of the whole). The same procedure was used to prepare the nanostructured F-doped ZnO sample except from adding a specific amount (2.14 mg) of ammonium hydrogen fluoride (NH_4FHF) in the starting solution aiming at obtaining a final atomic F concentration of 5 at.%. Two silicon supports with sputtered ZnO thin films were alternatively immersed uPSide down in the prepared suspensions within the Teflon recipients and heated at 90°C for 4 h. The obtained samples were rinsed with de-ionized water, dried with nitrogen, and finally calcined at 400 °C for 2 h.

Functionalization of as-prepared nanostructured nZnO(-F) films was performed through a three-steps process: silanization with (3-Aminopropyl)triethoxysilane (APTES), crosslinking bis(sulfosuccinimidyl)suberate (BS^3) anchoring and Protein A (pristine and FITC-labeled) grafting (Figure 3 | 15). APTES, toluene, BS^3, and PrA(*) were purchased from Sigma Aldrich (Milan, Italy). Hydroxyl (OH) groups were activated on the surfaces of nZnO(-F) samples by exposing the devices to oxygen plasma for 40 s. The cold plasma activation is a standard technique used to induce the formation of surface chemical functional groups through the use of plasma gases such as oxygen, hydrogen, nitrogen, and ammonia, which dissociate and react with the surface. Samples were then silanized using a 5% APTES solution in anhydrous toluene for 30 min at room temperature. Excess ungrafted silane was removed by intensive washing in dry toluene and subsequent curing performed at 100 °C for 10 min. Samples were then treated with a 1.7 mM solution of BS^3 in PBS pH 7.4 at 4 °C for 5 h. After the washing in PBS, samples were dried by a nitrogen stream and incubated with a 2 mg/mL solution of PrA* in PBS pH 7.4 overnight at 4 °C. Excess PrA* was removed by washing the samples five times in PBS. Any variation of the optical signals of devices was not observed after the last washing step, demonstrating the complete removal of unbound or non-specific bound PrA.

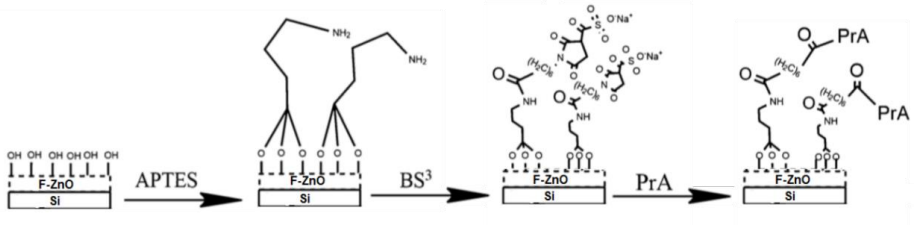

Figure 3 | 15. Outline of the ZnO(-F) nanostructures functionalization process.

3.3.2 ZnO(-F) nanostructures characterizations

The as-obtained nanostructures were morphologically characterized prior to the functionalization with scanning electron microscopy. The acquisitions were performed through a FESEM ULTRA-PLUS (Zeiss, Oberkochen, Germany) at 20 kV with the SE2 detector and a 15.9 mm working distance. The samples were gold sputtered (3 nm thickness) using a HR208 Cressington sputter coater.

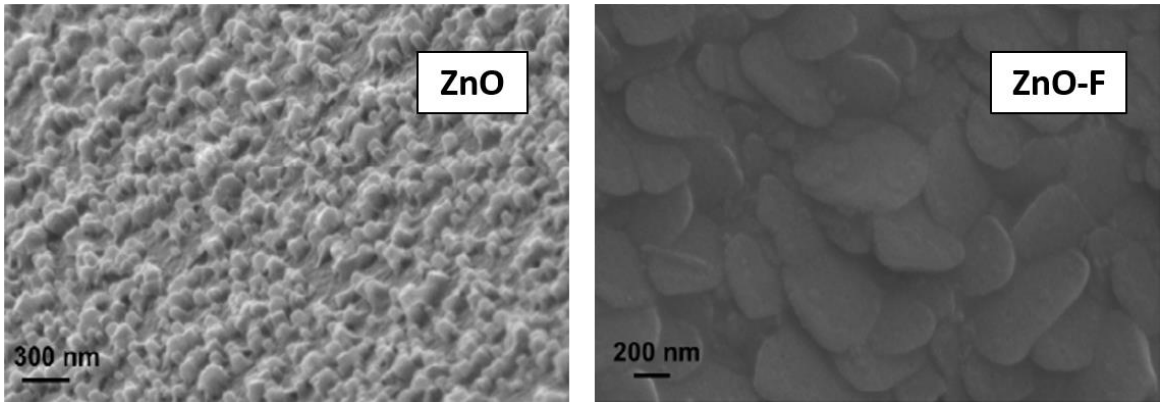

Figure 3 | 16. SEM images of as-synthesized nZnO(-F) nanostructures.

The presence of F atoms as doping agent in ZnO powders strongly affected the morphology of ZnO nanocrystals by inducing the formation of a clear granular nanometric phase [93]. The results, reported in Figure 3 | 16, highlighted an impressive difference of the morphology in the different materials: the nZnO-F appeared as a packed film constituted by flake-like nanograins of about 600 nm width; while the nZnO was formed by standard hexagonal nanocolumns (cf. Section 1.3) of 200 nm diameter almost perpendicular to the plane. The surface roughness of doped and undoped nZnO was measured by a profilometric technique; the nZnO-F was characterized by a rms (root mean squared) of 20(2) nm, while the nZnO surface resulted smoother (rms = 9(1) nm).

Water contact angle (WCA) measurements were performed to investigate the wettability of samples throughout the functionalization process and confirming the successful outcome of each step. A First Ten Angstroms FTA 1000 C Class coupled with drop shape analysis software was used for this purpose. The WCA values reported in this work are the average of at least three measurements on the same sample. Changes in the hydrophilicity coherent with those expected after each functionalization step were evidenced in both samples.

Material	Bare	Plasma	APTES	BS^3	PrA*
nZnO	117(7)°	61(9)°	98(2)°	54(8)°	65(10)°
nZnO-F	110(10)°	45(5)°	106(12)°	68(9)°	71(9)°

Table 3 | 4. Summary of the WCA values measured throughout nZnO(-F) surfaces functionalization.

Surface chemical composition of samples was investigated by Fourier Transform Infrared (FTIR) spectroscopy. FTIR spectra were acquired before and after PrA immobilization using a Nicolet Continuum XL (Thermo Scientific, Waltham, MA, USA) microscope in the wavenumber region of 4000–1200 cm^{-1} with a resolution of 4 cm^{-1}.

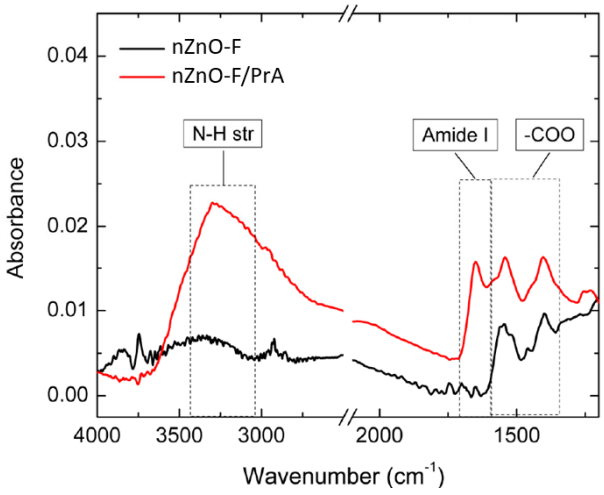

Figure 3 | 17. FTIR spectra of nZnO-F sample before and after PrA* conjugation.

Figure 3 | 17 shows the FTIR spectra of the nZnO-F sample acquired before and after the last functionalization step with PrA*; spectra related to intermediate

functionalization steps (i.e., APTES and BS^3) were not reported because any substantial variation was not observed. The features at 1540 and 1400 cm^{-1} were attributed to asymmetric and symmetric stretching modes of the acetate groups (-COO) absorbed during the synthesis process [73]. The peaks at 1650 cm^{-1} and about 3300 cm^{-1}, only visible in the spectrum of the functionalized sample, were due to the amide I band and to N-H stretching vibration of protein, respectively [95]. Differently, the FTIR spectrum of nZnO, after the PrA* immobilization procedure, did not evidence change, giving symptom of a very low amount of protein bound on its surface (data not shown).

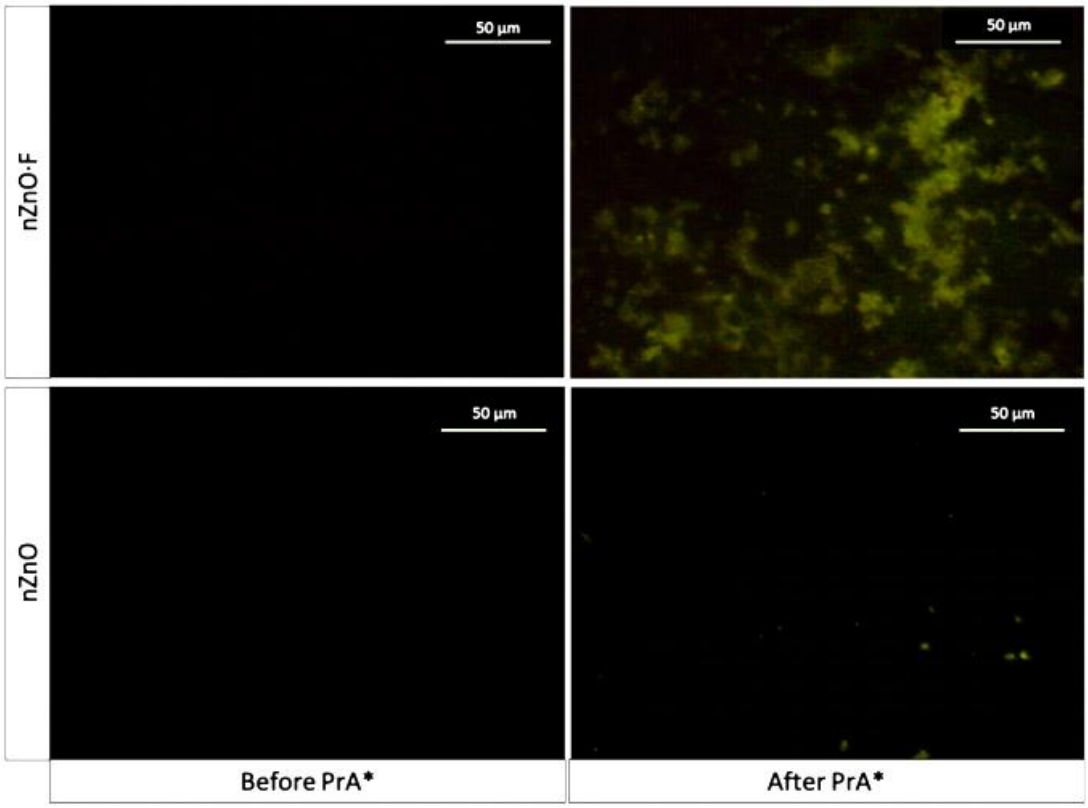

Figure 3 | 18. Fluorescence microscopy imaging of nZnO(-F) surfaces after functionalization and PrA* anchoring.

A Leica Z16 APO fluorescence macroscope equipped with a camera Leica DFC300 was used for the fluorescence analysis of the samples functionalized with PrA*. The imaging was performed using an I3 filter cube constituted by a 450–490 nm band-pass excitation filter, a 510 nm dichromatic mirror and a 515 nm suppression filter. Fluorescence microscopy imaging was used to highlight the presence of the PrA* on the sample surfaces after the last functionalization step. The images, reported in Figure 3 | 18, showed a

fluorescence homogeneously clustered on the whole surface of PrA*-modified nZnO-F (mean fluorescence intensity = 20(1) counts), while only few luminescent spots, corresponding to a mean fluorescence intensity of 13(1) counts, occurred on the surface of nZnO after PrA*. Analyzing the percentage difference between the values of the mean fluorescence intensities in both samples, we estimated that about 35% as much protein was immobilized on the F-doped one. The control samples, i.e., the nZnO-F and nZnO without the PrA*, appeared completely dark (mean fluorescence intensity = 5(1) counts). Indeed, the fluorescence microscopy imaging outcomes were in perfect agreement with the results obtained by FTIR spectroscopy.

To sum up, the results of the optical investigations clearly demonstrated that nZnO-F, synthesized on silicon substrate by a hydrothermal process in presence of ammonium hydrogen fluoride, could be functionalized with a higher efficiency with respect to the undoped nZnO. This effect was mainly ascribed to the characteristic flake-like morphology of the F-doped material, made of nanograins with a larger average lateral dimension (~600 nm) with respect to the nZnO nanocolumns (~200 nm) and with a more exposed area that could sustain a stronger surface interaction with the PrA biomolecules. In that, a mild chemical procedure based on aminosilane modification followed by a cross-linker (bis-sulfosuccinimidyl suberate) immobilization was used to covalently bind a model biomolecule, fluorescein-labeled protein A, on the nZnO-F surface. All the FTIR, WCA and fluorescence microscopy characterizations revealed a successful functionalization of the surface. The examined characteristics set the basis for the design of PL-based biosensing platforms, whose proof-of-concept will be discussed in Chapter V.

Chapter IV – Materials applications I: *in vivo* time-gated imaging of luminescent porous silicon nanoparticles in *Hydra vulgaris*

4.1 *In vitro* study on HeLa cells: cytotoxicity and fluorescence imaging

In vitro studies represent the very first step towards the application in living organisms. The interactions between cells and external agents may follow different and complex mechanisms and a crucial requirement is that the examined compound/composite/… does not induce any undesired effect on the cellular vital processes. Cell viability is usually quantified via a colorimetric assay relatable to the presence of compounds only produced in living cells. Such compounds usually exhibit a characteristic optical absorbance trace whose "intensity" is straightforwardly linked to the cell metabolic activity, which is plotted in a histogram expressed in terms of percentage of living cells. Among all the available assays, the monitoring of mitochondrial degradation of the dye MTT (yellow) into its reduced counterpart (purple) is commonly used [96].

As far as PSiNPs are concerned, a favorable premise lies in the fact that Si is a fully biocompatible material, since it hydrolyzes in physiological environment degrading into orthosilicic acid (formula $Si(OH)_4$) and it is consequently expelled from the body via the urinary pathway [97]. However, to ensure that no toxicity contribution appears, MTT assays were performed at two different concentrations (50 µg/mL and 100 µg/mL) of bare and UA-conjugated PSiNPs at 3 h, 6 h and 24 h incubation times. The experiments were performed on the HeLa cell line.

The results are shown in Figure 4 | 1: as can be seen, (h)PSiNPs samples seem to display an excellent biocompatibility. In particular, cell viability is almost 100% for up to 6h incubation at 50 µg/mL of pristine PSiNPs and slightly decreases to 89(3)% after 24 h. A similar trend was evidenced for hPSiNPs 50 µg/mL (89(2)% after 6 h, setting to 70(1)% after 24 h). In both cases, cell viability retains a high percentage even after 24 h incubation for both pristine and UA-conjugated PSiNPs (77(2)% and 66(4)%, respectively) at higher (h)PSiNPs concentrations (100 µg/mL). However, it is important to underline that the utilized methodology is not sufficient to provide an unambiguous cytotoxicity assessment, since enzymatic reduction-based strategies, including MTT, suffer from a limitation when

PSi-based nanostructures are tested. This is due to an undesired non-specific dye reduction ascribable to the presence of highly reactive Si hydride groups and dangling bonds on the (h)PSiNPs surface, which leads to an overestimation of cell viability [98], [99]. Thus, an investigation via direct observation is required to evaluate the morphological appearance of the treated HeLa cells samples.

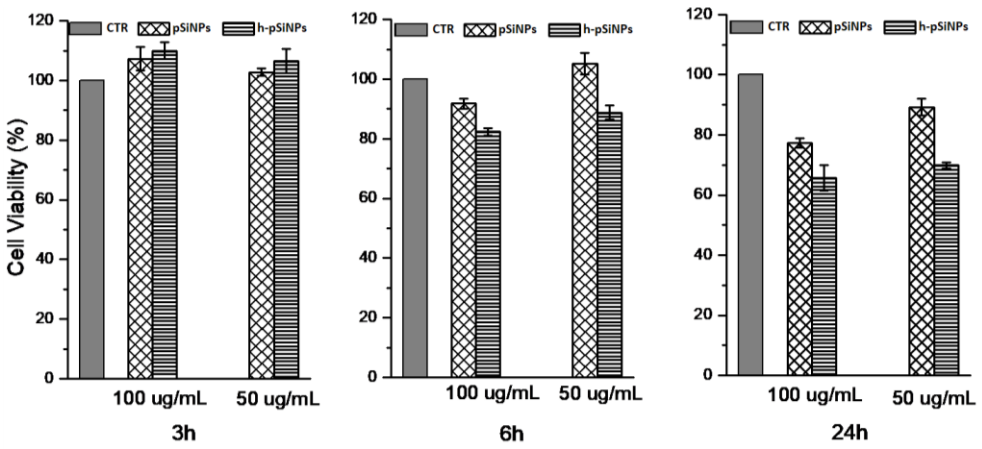

Figure 4 | 1. MTT assay on HeLa cells at different concentrations and incubation times of (h)PSiNPs samples.

As a next step, a preliminary fluorescence imaging feasibility study was carried out. To this aim, (h)PSiNPs samples (100 µg/mL) were resuspended in HBSS-HEPES cell medium at slightly acidic pH (~5.5). HeLa cells were incubated at T = 37 °C for 6 h. After treatment, the cells were gently washed with fresh HBSS-HEPES medium, fixed using 4% paraformaldehyde and observed using a Zeiss ApoTome microscope. A custom filter cube with band-pass excitation (~365 ± 30 nm) and long-pass emission (cut-on ~420 nm) was employed for all observations.

The result is reported in Figure 4 | 2. As can be noticed, control and pristine PSiNPs-incubated samples appeared completely dark. Besides, fluorescence could only be evidenced in HeLa cells incubated with hPSiNPs, thanks to the enhancement of the photoemissive stability consequent to UA surface capping. hPSiNPs appear randomly distributed throughout the whole cell without a preferential site. An improvement in the targeting becomes practical with the addition of specific biorecognition elements, conjugable by virtue of the carboxyl moieties exposed on hPSiNPs surface. However, the drawback of endogenous fluorescence limits the applicability of such approach to *in vitro* samples, where such signal usually gives a negligible contribution.

The outcomes pave the way towards the *in vivo* imaging application of hPSiNPs, which require the development of alternative strategies as will be disserted in the next sections. From now on, pristine PSiNPs will not be considered due to their PL instability in aqueous environment (cf. Section 3.1.2).

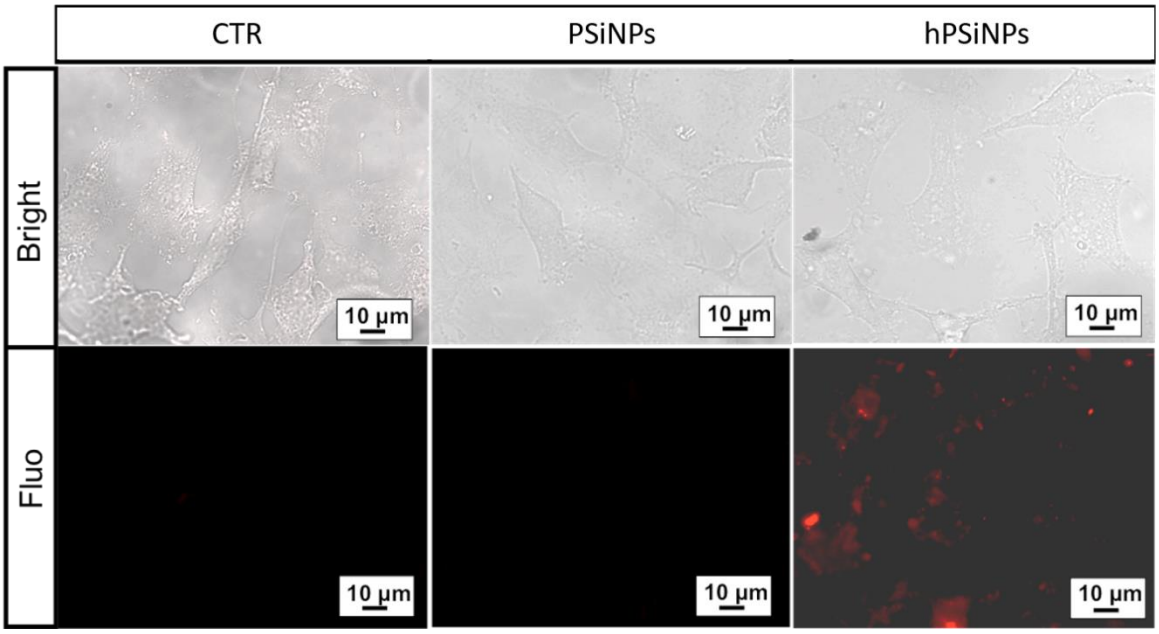

Figure 4 | 2. Fluorescence imaging of unlabeled HeLa cells incubated in HBSS-HEPES medium with 100 µg/mL of (h)PSiNPs samples (6 h).

4.2 *In vivo* toxicity assessment in *Hydra vulgaris*

4.2.1 *Hydra vulgaris* as model organism

The positive results of *in vitro* assays are not necessarily predictive of analogous outcomes *in vivo*; therefore, the *in vivo* evaluation of NPs toxicity is of utmost importance for the development of safe nanodevices for biomedical applications. In this context, *Hydra vulgaris* (*Cnidaria*, *Hydrozoa*) is used as *in vivo* model.

Hydra is a simple multicellular organism consisting of a tube made of two connected epithelial cell layers: the outer ectoderm and inner endoderm, separated by an acellular mesoglea layer (Figure 4 | 3) [100]. At the top end of the body, there is the hypostome composed by an oral cavity surrounded by 6–8 tentacles containing the most part of stinging cells that help *Hydra* catch its prey [101]. The central body has four

distinctive sections: the gastric region, located between the tentacles and the apical bud; the budding section, from which buds grow and detach; the peduncle, located between the lowest bud and basal area; and the basal disc, which is an adhesive foot-like formation [102]. A diffuse nerve net throughout the body constitutes a simple nervous system [103]. This structural complexity, simpler than vertebrates with central nervous system and specialized organs, but more complex than cultured cells, makes *Hydra* comparable to a living tissue whose cells and distant regions are physiologically connected.

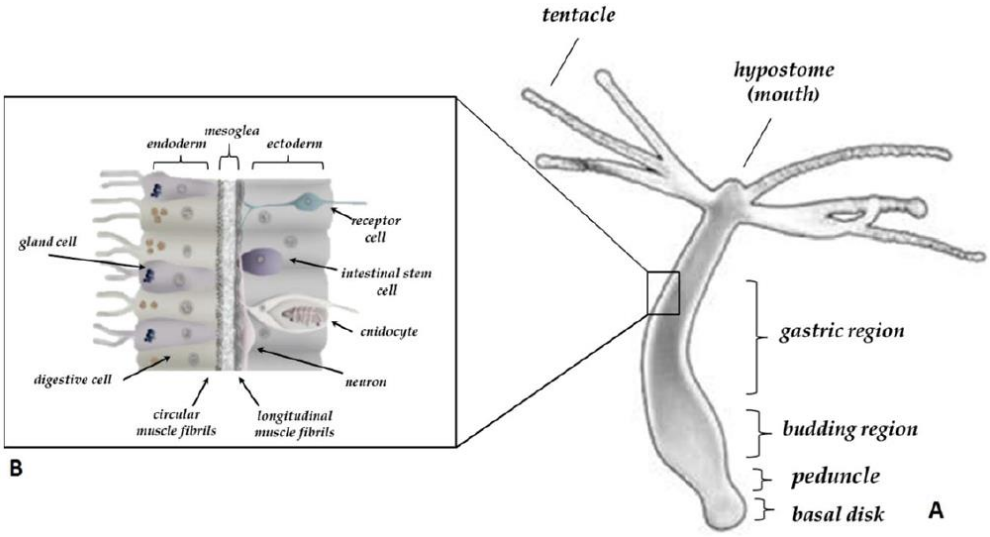

Figure 4 | 3. Schematics of *Hydra* morphology [104]. The inset shows the bilayer structure characterizing the whole body, from the foot to the tentacles, i.e. the ectoderm and endoderm layers separated by the mesoglea. The few specialized cell types differentiated by the interstitial stem cells are shown (neurons, cnidocytes, gland cells).

4.2.2 Morphological toxicity tests

Hydra is sensitive to a range of pollutants and has been used as a biological indicator of water pollution [105]. Several bioassays are available to assess the toxicity of a given substance in terms of acute or sub-lethal toxicity. *Hydra* exposure to different substances may cause:

(1) alteration of morphological traits and developmental programs;

(2) alteration of regeneration or pattern formation;

(3) alteration of population growth rates (measuring *Hydra* population growth by asexual reproduction).

Moreover, the toxicity can also be analyzed at the single cell level by macerating the whole animal into fixed cell suspension and pursuing *in vitro* procedures analogous to those described in Section 4.1.

Herein, to evaluate the impact of PSiNPs in *Hydra* organism, it was decided to proceed by examining the traits identified by category (1). Toxicity of a substance can be measured and quantified observing changes in the animal morphology following a criterion given by Wilby's classification (depicted in Figure 4 | 4(a)), which attributes a score from 10 (normal, elongated tentacles and body) to 0 (disintegrated) [106]. Scores 10−6 are reversible while the tulip phase (score 5 and below) is considered as the endpoint for lethality [106]. With this premise, a screening of the animals morphology *via* direct observation has been performed at first stage.

In order to attribute a toxicity score according to Wilby's criterion, bright field real-time monitoring of *Hydra* incubated at different concentrations of hPSiNPs and hPSiNPs_PLL was carried out. To this aim, samples of hPSiNPs (in IPA) and hPSiNPs_PLL (in H_2O) were centrifuged three times at 15000 rpm for 50 mins and resuspended in *Hydra* medium buffer ($NaHCO_3$ and $CaCl_2$ 1:2 v/v aqueous mixture, pH ~ 6) at 1 mg/mL concentration. N = 5 animals were then incubated in the as-prepared samples (V_f = 200 µL) at room temperature and continuously observed using a Leica DM6 M microscope equipped with DFC 7000 T camera at 5x magnification. The same number of animals in freshly prepared medium were kept as control (CTR).

The results are reported in Figure 4 | 4(b). High concentrations of UA-conjugated hPSiNPs revealed to be totally non-toxic, since *Hydra* morphology did not result affected (score 10) after up to 72 h incubation at 1 mg/mL. Notably, 1 mg/mL of hPSiNPs_PLL led to very low scores, showing lethal toxicity after 2 h incubation. This evidence was ascribed to cell damages induced by the high amount of amine groups in PLL [107]. However, incubations at lower material dosages (0.5 mg/mL and 0.25 mg/mL) resulted in a progressive increase of biocompatibility, reaching a score 10 in the latter case. Therefore, 2 h incubation at 0.25 mg/mL of hPSiNPs_PLL represented the right compromise of usage thanks to both the high PL from hPSiNPs_PLL and the requirement of short uptake time for positively charged materials [108].

It is important to underline that these results represent a preliminary assessment. Other studies to univocally establish the exact degree of toxicity, including screening on a higher number of animals as well as analyses on growth rate, still need to be carried out.

However, the feasibility of usage of hPSiNPs_PLL as label-free luminescent probes for bioimaging can be considered proven.

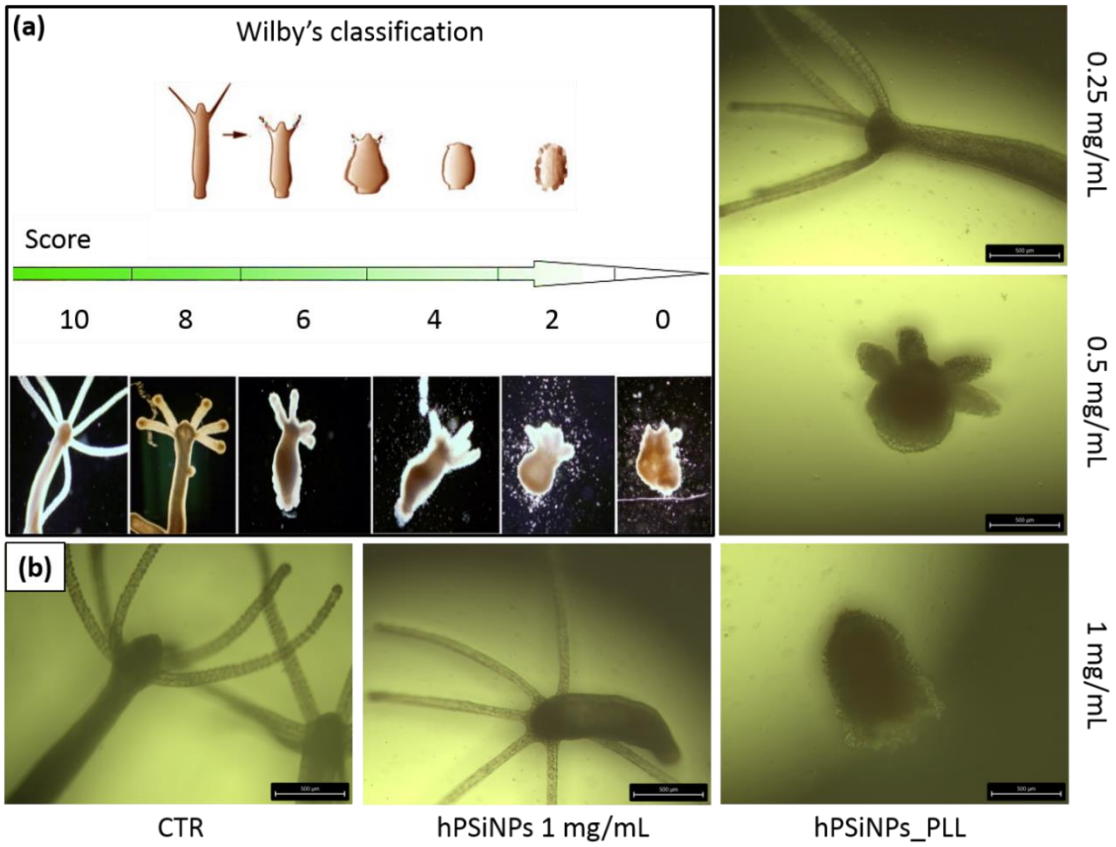

Figure 4 | 4. (a) General scheme for toxicity score attribution according to Wilby's criterion. (b) Evaluation of toxicity of hPSiNPs and hPSiNPs_PLL (in the latter case at different concentrations in order to establish the working conditions) at 2 h incubation. The scale bar is 500 µm.

4.3 *In vivo* imaging of *Hydra vulgaris*

4.3.1 Time-gated fluorescence imaging technique

Fluorescence imaging is one of the most versatile and exploited tools in the biomedical as well as clinical diagnostics fields [109]. This technique is commonly implemented using exogenous fluorescent probes. In that, a major limitation is represented by the background signal originating from bright tissue autofluorescence, interfering with and limiting the spectral discrimination of the probe component. It is commonly referred as "autofluorescence" the background emitted light, generally occurring in tissue sections,

unrelated to that of the target probe, making it difficult to discern relevant signal from background noise and crucially worsening the signal-to-noise ratio of the measurement. Tissue autofluorescence is often due to native components such as fluorite, chlorophyll (in plants), collagen, and others [110]. These components are generally fluorescent in the green and yellow portions of the visible spectrum, which is the same wavelength range of some of the most utilized fluorophores in immunofluorescence assays (e.g., FITC or Alexa Fluor 488). Autofluorescence also results from the use of fixatives, which are commonly used to "immobilize" biological samples while retaining their cellular structure. Such fluorescence contribution leads to a broad emission over the whole visible spectral range.

In order to overcome this issue, several alternative methods have been developed, including use of fluorophores that emit in the near-infrared (NIR) range where tissue autofluorescence contribution is reduced [111], two-photon or upconverting probes that allow NIR excitation (which indeed does not excite endogenous fluorophores [112]), and longer-lived probes (lanthanides [113], quantum dots [114]) imaged by time-gated luminescence [115], [116]. Luminescent imaging probes based on silicon nanostructures [97], [117], [118] have gained much recent attention due to their significantly lower toxicity with respect to quantum dots derived from heavy metals, e.g., cadmium [119], their reduced photobleaching relatively to organic fluorophores [120], distinctive emission in the red-NIR, tissue-penetrating region of the spectrum, biodegradability and biocompatibility [97]. Thanks to the indirect nature of the silicon bandgap (cf. Section 1.2.2) silicon nanocrystals display a very long radiative lifetime (μs range) and, as already anticipated in Section 1.2.3, this can be greatly harnessed for time-gated imaging.

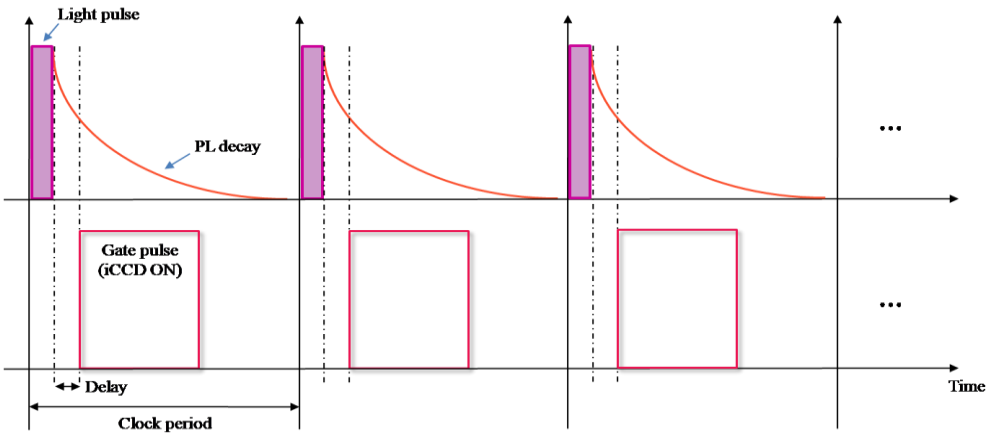

Figure 4 | 5. Temporal sketch for time-gated imaging implementation. Light (excitation) and gate (detection) pulses have the same periodicity and only differ for a fixed delay in the acquisition.

Fluorescence lifetime-based imaging usually requires highly sensitive instrumentation in order to discriminate the small differences between the radiative lifetimes of the components of the system to be imaged (usually in biological systems τ falls within 1-10 ns range) [121]. However, when such differences are huge (even by orders of magnitude), i.e., when a proper longer-lived probe is used, a gain in the contrast can be much more straightforwardly achieved with the time-gating method [122]. In particular, this approach employs an excitation pulse and integrates the emitted light within a certain temporal interval and at a delayed controlled time [123]. The delay time can be set and optimized in order to eliminate the short-lived autofluorescence signal and, at the same time, maximize the longer-lived probe signal by properly setting the integration time. The time-gated imaging technique requires a precise temporal correlation between the pulsed excitation source and the detector, which must match the same clock periodicity except from the fixed delay (Figure 4 | 5).

The scheme that was implemented in this thesis was optimized to pursue imaging in reflection mode (Figure 4 | 6): the detection system is constituted by a Peltier-cooled ANDOR iStar iCCD camera, coupled to an Olympus ACH 10x/0.25na infinity-corrected objective; the excitation source was provided by pulsed UV LED (LLS 365, Ocean Optics), guided to the sample via optical fiber; the whole system was triggered by means of a Keysight 33220A pulse generator. The electronic connections were optimized so to minimize undesired signal reflections or impedance mismatches that could lead to timing delays.

The limitations of the implemented setup are majorly represented by the limited working range of the Peltier coolers ($T_{min} \geq -10$ °C) which implies an intrinsic dark current signal and, most significantly, by the temporal length of the transients, i.e., the intrinsic jitter time of the trigger pulse as well as the temporal profile of the excitation pulse. A higher contrast can be achieved by minimizing the controlled delay in the acquisition, thus integrating a greater portion of the long-lived probe decaying signal.

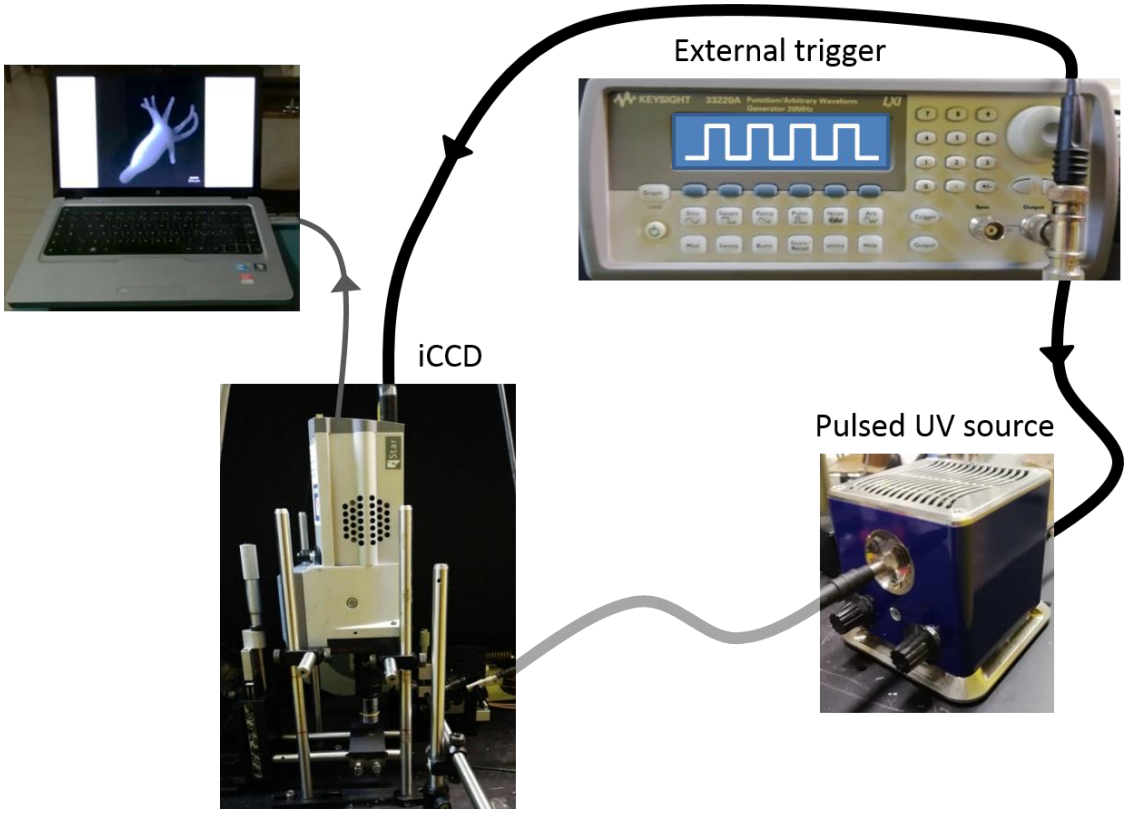

Figure 4 | 6. The components utilized in this thesis for time-gated imaging setup implementation: (a) pulse generator that provides the clock trigger; (b) externally modulated iCCD camera coupled to 10x objective and (c) externally triggered UV LED source (365 nm).

4.3.2 *In vivo* fluorescence imaging of *Hydra vulgaris*

Once completed the evaluation of feasibility for the usage of hPSiNPs(_PLL) *in vivo* (Section 4.2.2), the final step was to implement the application of such nanomaterials as luminescent probes in fluorescence imaging. In order to evaluate the uptake of hPSiNPs_PLL, N = 3 animals were firstly washed in freshly prepared Hydra medium and incubated at 1 mg/mL hPSiNPs and 0.25 mg/mL hPSiNPs_PLL concentrations previously resuspended in the same buffer (cf. Section 3.1.3) in mildly acidic pH regime (pH = 6). N = 3 animals were kept as control. The animals were continuously observed in real time, both in bright field and fluorescence modes (365 nm excitation; long-pass emission filter) in their incubation environment for up to 2 h using a Leica DM6 M microscope under 5x objective.

An effective interaction guided by electrostatic attraction between *Hydra* and hPSiNPs_PLL was observed already after 1 h incubation (Figure 4 | 7). The random distribution of the probe along the whole animal body suggests a passive uptake

mechanism. This evidence was further confirmed by the total lack of interaction with negatively charged hPSiNPs except from an accumulation on the adhesive basal disk.

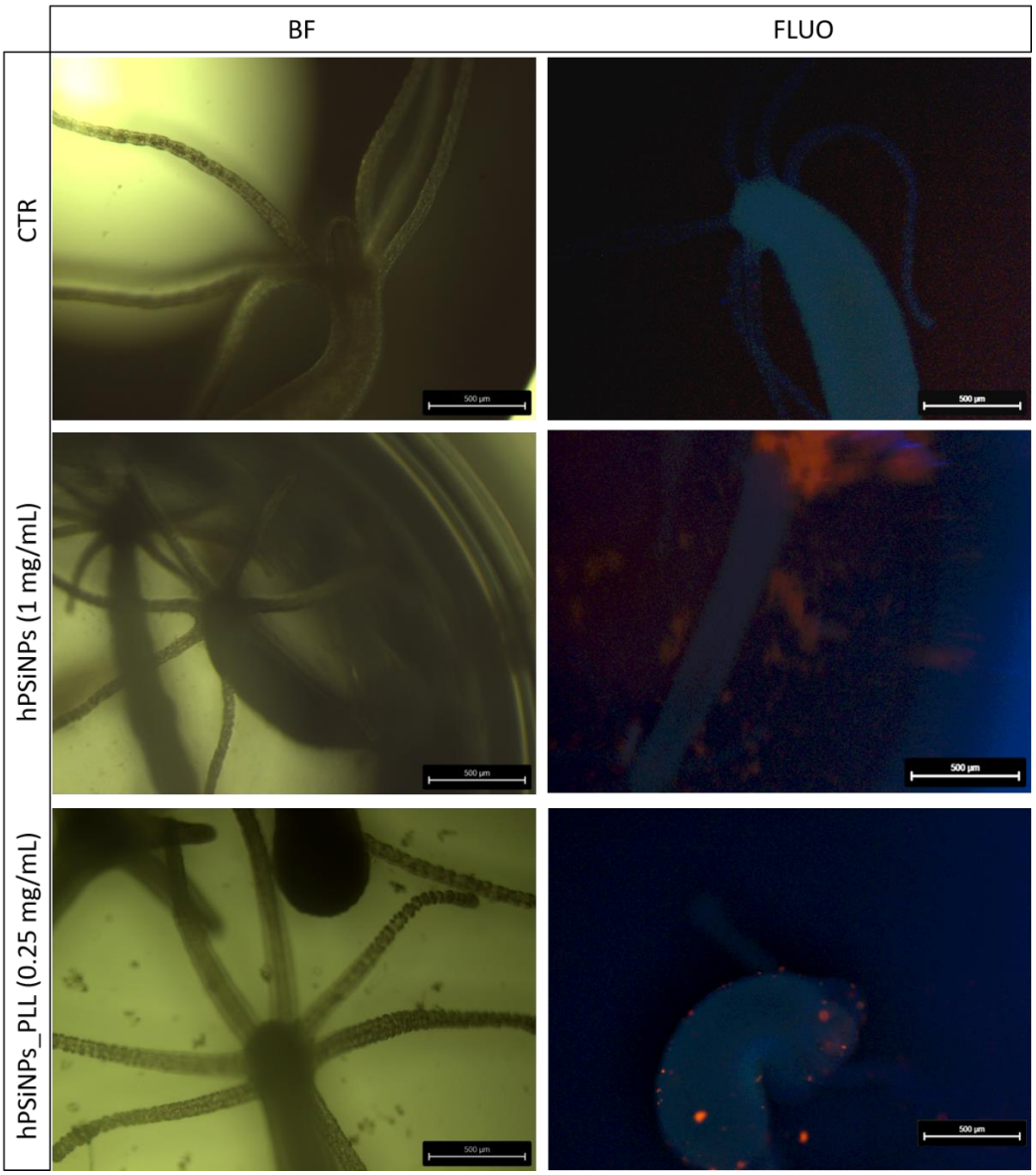

Figure 4 | 7. Real-time *in vivo* imaging of *Hydra vulgaris* during incubation at 1 mg/mL of hPSiNPs and 0.25 mg/mL of hPSiNPs_PLL. Control animals were observed as well. The acquisitions herein reported were taken at ~ 1 h incubation. The scale bar is 500 µm.

After 2 h observation, the animals were removed from the incubation environment, washed three times in freshly prepared Hydra medium, relaxed using 2% urethan solution [124], fixed using Lavdowski fixative, dried on a microscope slide and re-observed to evaluate hPSiNPs_PLL internalization. NPs on different focal planes, randomly distributed over the whole animal body (tentacles, hypostome area, gastric/budding regions) could be

evidenced in the incubated *Hydra*. However, internalization establishes at the sub-ectodermal level due to the limited incubation time. Despite the difference being univocally detectable with respect to the control animal (Figure 4 | 8 and Figure 4 | 9), the intense tissue autofluorescence severely limits the visibility of hPSiNPs_PLL. The next and final step will then be the application of time-gated imaging on this same *in vivo* experiment.

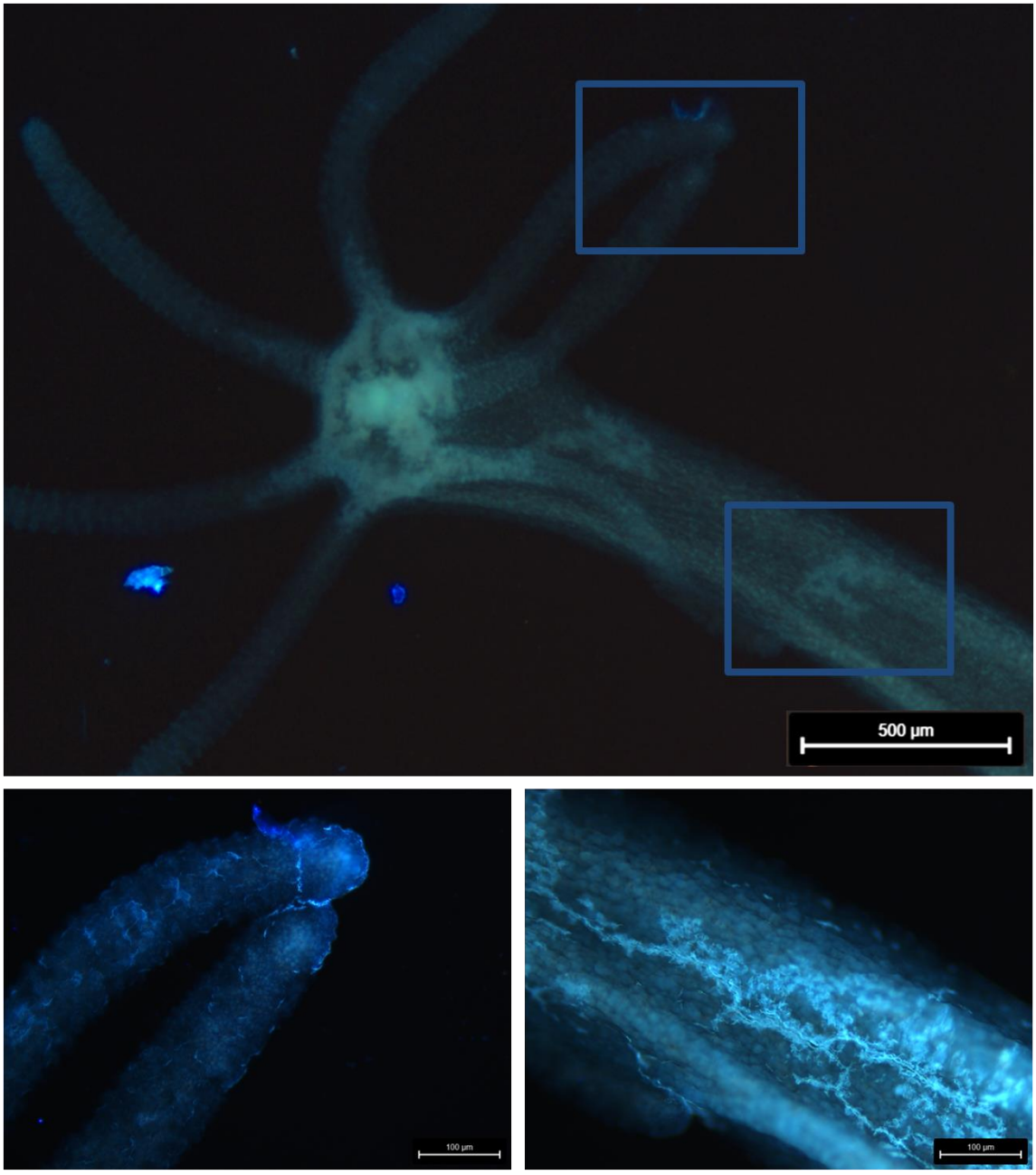

Figure 4 | 8. Fluorescence imaging of *Hydra vulgaris* (CTR) after fixation. The highlighted areas correspond to the images at higher magnification on the lower panel *(continues on next page)*.

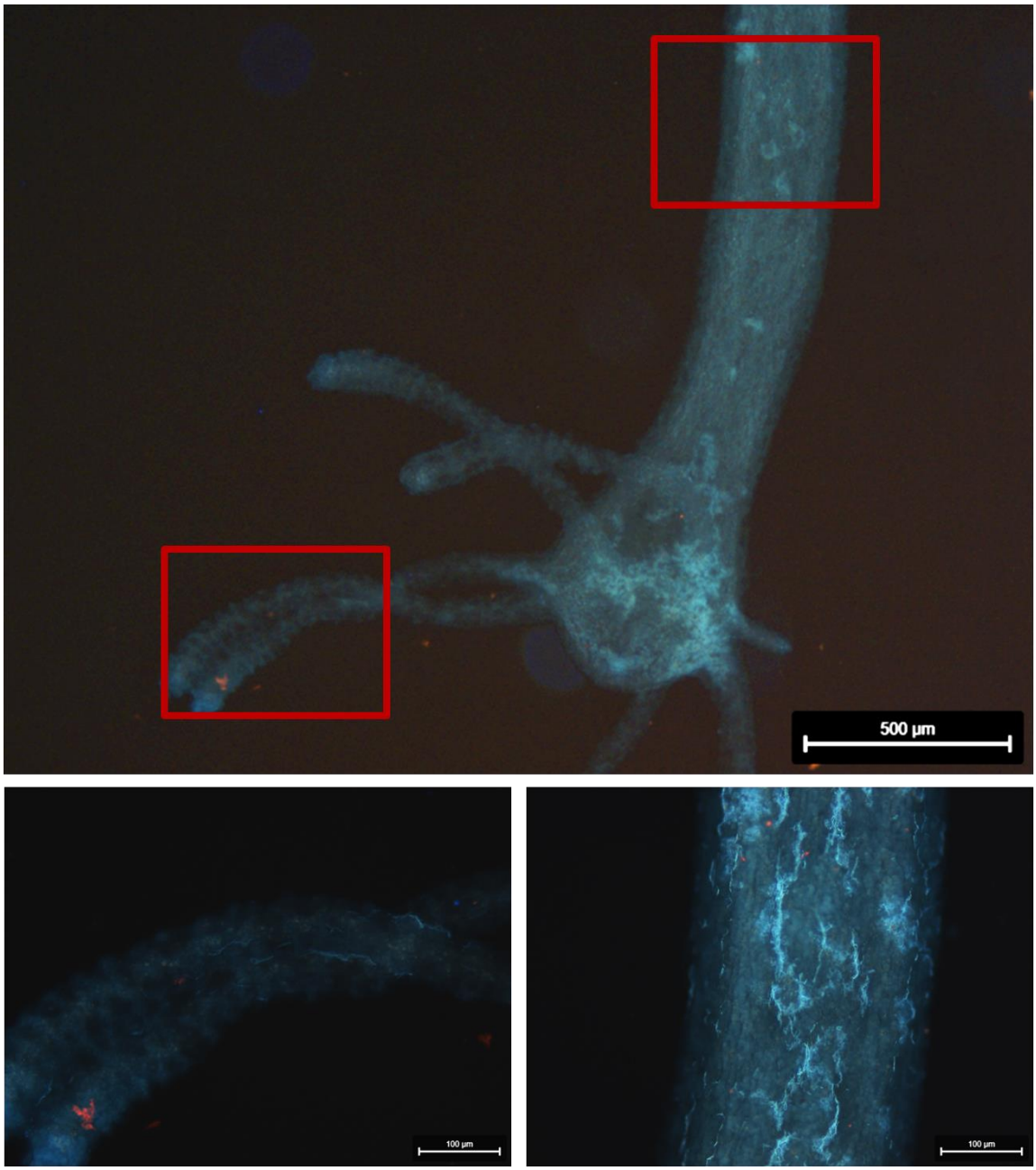

Figure 4 | 9. (Continues from Figure 4 | 8) Fluorescence imaging of *Hydra vulgaris* incubated at 0.25 mg/mL of hPSiNPs_PLL for 2 h after fixation. Again, the highlighted areas correspond to the images at higher magnification on the lower panel. The scarcely visible NPs are on different focal planes.

4.3.3 *In vivo* time-gated fluorescence imaging of *Hydra vulgaris*

As could be evidenced in the previous Section, hPSiNPs_PLL internalization was evidenced but scarcely visible due to *Hydra* autofluorescence. To probe the improvement in the image contrast expected by the application of the time gating, the same imaging experiment was replied with the experimental setup illustrated in Figure 4 | 6.

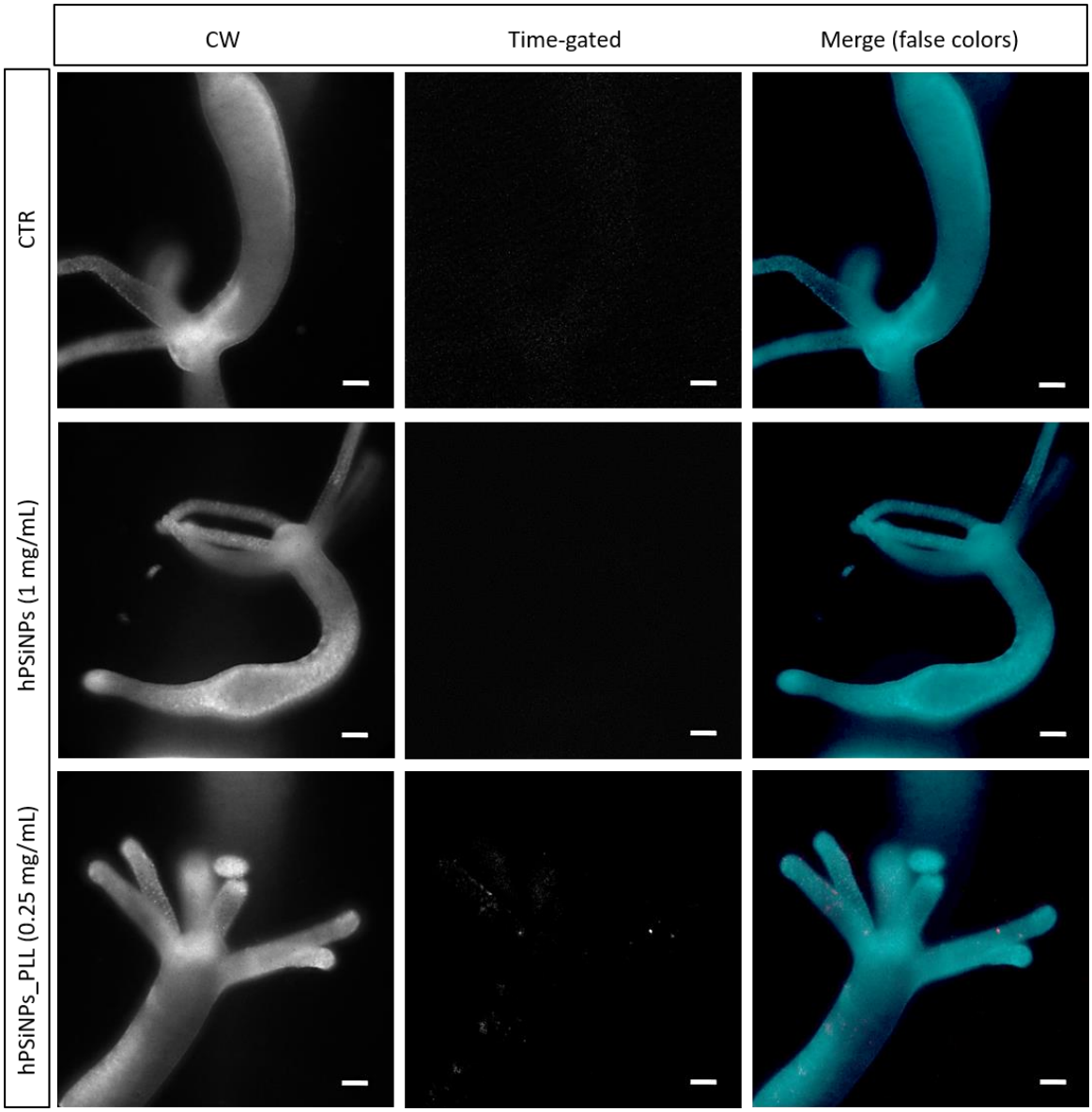

Figure 4 | 10. CW (left) and time-gated (right) *in vivo* images of *Hydra* after 2 h incubation in Hydra medium (CTR), hPSiNPs 1 mg/mL and hPSiNPs_PLL 0.25 mg/mL. Internalization only occurs in positively charged NPs. The scale bar is 200 μm.

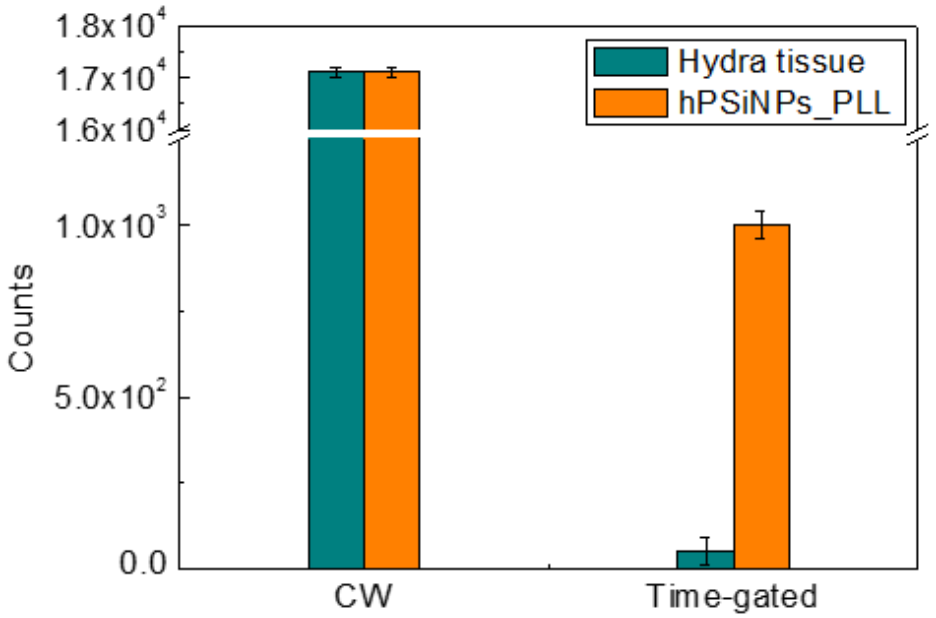

Figure 4 | 11. Histogram reporting the maximum registered counts before and after time-gating (referred to the images in the lowest panel of Figure 4 | 10). Such analysis allows to roughly evaluate the enhancement in the SNR thanks to the gating.

The incubation protocol was the same applied in the previous Section. To minimize temporally uncorrelated scattered light contributions, the animals were drop casted on flat crystalline Si and imaged. All the observations were conducted on urethan-relaxed animals, so completely *in vivo*. The UV source and the iCCD camera were triggered with a TTL squared pulse at 1 kHz frequency and duty cycle 20%. The observation window (iCCD gate pulse width) was set at 300 µs and the total exposure time at 200 ms to exploit the analogic Integrate-on-Chip function to further increase the collected signal. The camera temperature was set at T = -5 °C. The optimized time-gating resulted being of 16 µs due to the intrinsic jitter time of the excitation pulse.

As can be noticed, the short-lived light contribution from the living polyp was completely cut after the gating, with a registered intensity comparable to the dark current signal of the iCCD. At the same time, no long-lived PSiNPs contribution resulted in both CTR and highly concentrated hPSiNPs-incubated animals (Figure 4 | 10). This latter evidence confirms the impeded internalization due to the electrostatic repulsion between negatively charged UA-conjugated PSiNPs and *Hydra* ectodermal cells membrane. Coherently, an internalization was observed in the case of the hPSiNPs_PLL sample instead; hence, a quantitative analysis of the acquired intensity allows to estimate the

improvement in the signal-to-noise ratio (SNR), evaluated at the same excitation intensity, iCCD gain and setup configuration, before and after time gating. In particular, SNR is herein defined as the ratio between the average PSiNPs_PLL and the average *Hydra* tissue intensites, SNR = I_{PSiNPs}/I_{Hy}. When imaging in CW, hPSiNPs_PLL and *Hydra* tissue signals are totally indistinguishable, thus implying SNR ≤ 1. After time gating, the same ratio was estimated to increase up to ~20 as deducible from the histogram reported in Figure 4 | 11 ($I_{Hy}^{(TG)}$ ~50 cts., $I_{PSiNPs}^{(TG)}$ ~10^3 cts.). Such value can be straightforwardly increased by further iCCD temperature lowering and using faster excitation sources that allow to shorten the gating delay and, consequently, collect a greater fraction of emitted long-lived photons.

Many efforts can be further fulfilled to improve the outcomes of this technique, starting from PSiNPs functionalization, which can be optimized both in terms of biocompatibility (in order to lengthen the incubation time and probe the exact internalization dynamics) and targeted uptake (by virtue of selective biorecognition elements conjugation). However, the present study represents a crucial intermediate step in pursuing this objective.

Chapter V – Materials applications II: towards label-free optical biosensing with photoemissive nanostructures

This last chapter is devoted to the evaluation of the designed and surface-modified photoemissive nanostructures, extensively characterized in Chapter III, as innovative platforms in the biosensing field. Preliminary tests carried out in relevant diagnostic contexts allowed to set a point on their feasibility of usage, oulining their rapid and specific detection potential.

5.1 PSi/GO hybrid device for early diagnosis of Brugada syndrome

Brugada syndrome (BS) is a genetic disorder that conveys a predisposition to the risk of malignant ventricular arrhythmias, which lead to sudden death in young patients even in absence of evident cardiac structural anomalies [125]. More than 500 genetic mutations have been identified as responsible of BS so far, most of which can be associated to point-mutations in a specific gene, the SCN5A [126]. The current methodologies applied for BS diagnosis are based on the identification of a characteristic electrocardiographic pattern, observed either spontaneously or after dosing of sodium-channel blocker drugs, coupled to a genetic analysis [127]. Notably, the early diagnosis of this insidious pathology still represents a huge challenge [128].

In this perspective, nanotechnologies that exploit DNA or RNA as biorecognition elements have gained greater attention thanks to their potential application for the diagnosis of a wide range of diseases [129]. More recently, the introduction of peptide nucleic acids (PNAs) has marked a turning point in the field of DNA biosensing thanks to their unique physicochemical properties. Substantially, a PNA is a synthetic analogous of DNA, but the crucial difference lies in the composition of the organic backbone of the strands. In particular, the negatively-charged deoxyribose-phosphate structures of DNA are replaced by a neutral pseudo-peptide backbone, N-(2-aminoethyl) glycine. For this reason, the PNA/DNA hybridization is stronger than the one between DNA/DNA strands due to the lack of electrostatic repulsion [130], thus conferring a detection specificity at the single-base level. This feature makes PNAs a powerful tool for the diagnosis of genetic diseases.

In this work, a PNA molecule, designed to interact specifically with an appropriate DNA sequence of the SCN5A gene, is used as bioprobe. Herein, the developed and

characterized PSi/GO hybrid device, on which the PNA is covalently conjugated, serves as functional platform for multi-parametric optical biosensing and DNA target hybridization monitoring.

5.1.1 PNA covalent anchoring onto PSi/GO chip

Firstly, preliminary characterizations were carried out testing the PSi/GO hybrid architecture with BS-specific unlabeled PNA sequence, which is by its very nature highly specific towards its DNA complementary counterpart. From the chemical point of view, PNA conjugation was fulfilled following the same strategy adopted for PrA*, via EDC/NHS linking (cf. Section 3.2.2): specifically, amide bonds between GO carboxyl moieties and PNA terminal amine groups were formed. After PNA anchoring, a quenching of the GO PL signal could be evidenced (Figure 5 | 1(a)). Aiming at investigating this phenomenon, different PNA concentrations (100 µM, 300 µM, 600 µM) were incubated on the PSi/GO chip. The resulting trend is reported in Figure 5 | 1(b), where a dependence of the integrated PL intensity from the incubated PNA concentration is clearly shown. Such evidence can be ascribed to the increasing occupation of GO emissive radiative sites by PNA binding. The threshold concentration of 300 µM represents an estimation of the amount of probe that maximizes the GO active binding sites passivation.

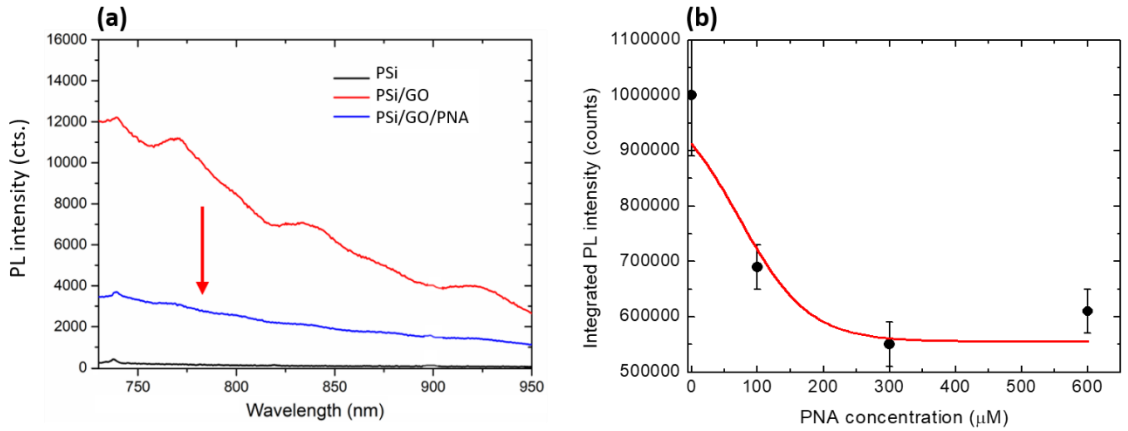

Figure 5 | 1. (a) Steady-state PL spectrum of PSi/GO composite before and after unlabeled PNA anchoring (300 µM). (b) Integrated PL intensity as a function of different incubated PNA concentrations.

5.1.2 Preliminary study on DNA sequence detection

Aiming at probing the DNA sensing capabilities of the PSi/GO/PNA architecture, a complementary (5'-AGGAGAGCACCGAGCCCCTGAG-3') FITC-labeled DNA sequence (at 100 µM concentration) was allowed to incubate on the PSi/GO/PNA platform for 2 h. After incubation, the sample was gently rinsed in deionized water to remove the unhybridized target.

The DNA*-incubated samples was characterized via spectroscopic reflectometry analogously to the PrA* infiltration monitoring procedure described previously (cf. Section 3.2.3), i.e., by analyzing the changes in the photonic features of the chip. Notably, 300 µM PNA concentration, despite maximizing the GO binding sites passivation, also resulted being the threshold for pore clogging, since a saturation in the reflectance spectra red-shifts could be evidenced at higher bioprobe amounts (data not shown). Hence, the measurements were carried out at a lower bioprobe concentration, from 300 to 100 µM. In this regime, as reported in Figure 5 | 2, a 24 nm red-shift could be detected in the FFT curves maxima, denoting an increase of the refractive index of the Faby-Pérot structure as a consequence of the target infiltration.

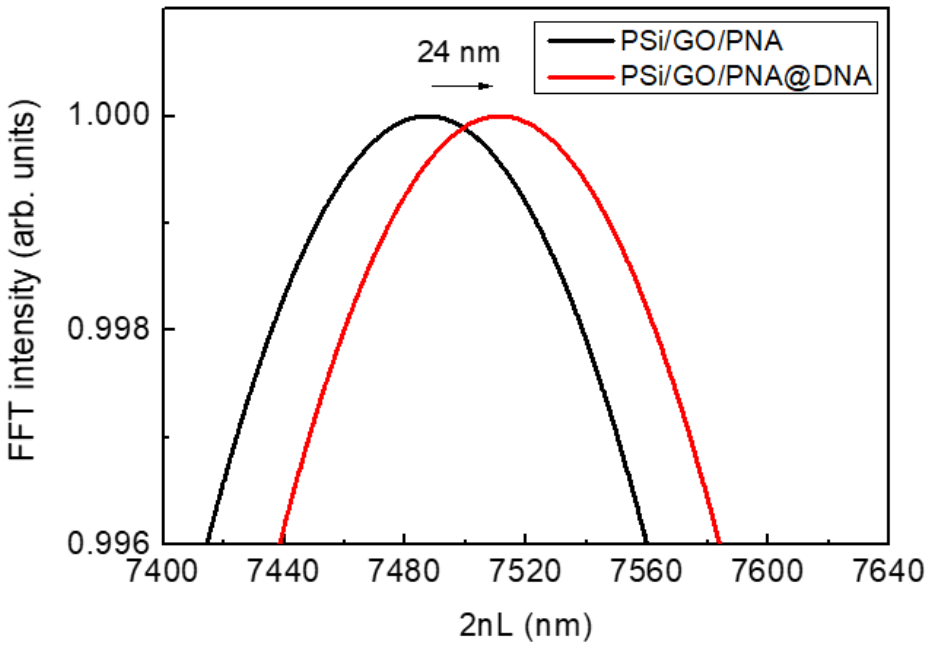

Figure 5 | 2. FFT analysis of PSi/GO/PNA nanocomposite chip before and after 2 h incubation with complementary DNA (100 µM).

A non-complementary FITC-labeled sequence (100 µM; 5'-CCTTTTTTTTTT-3') was also incubated to evaluate the specificity of the device. Both labelled complementary (c-) and non-complementary (nc-)DNA-incubated samples were monitored via fluorescence microscopy. Fluorescent samples were imaged using an inverted fully automated confocal Nikon AR-1 microscope. The NIS elements software was used for images acquisition/elaboration. As reported in Figure 5 | 3(a), no fluorescent signal could be detected after 2 h incubation with nc-DNA. Besides, a traceable signal was measured in the sample incubated with the complementary sequence. Confocal imaging was used as further technique to confirm the infiltration of c-DNA* within the porous matrix. Figure 5 | 3(b) provides a 3D representation of all the fluorescent focal planes recorded by the instrument. The side-view of the reconstructed focal planes is also shown. Globally, the data allowed to confirm the occurred hybridization between the PNA-functionalized PSi/GO device and the corresponding target without undesired non-specific interactions.

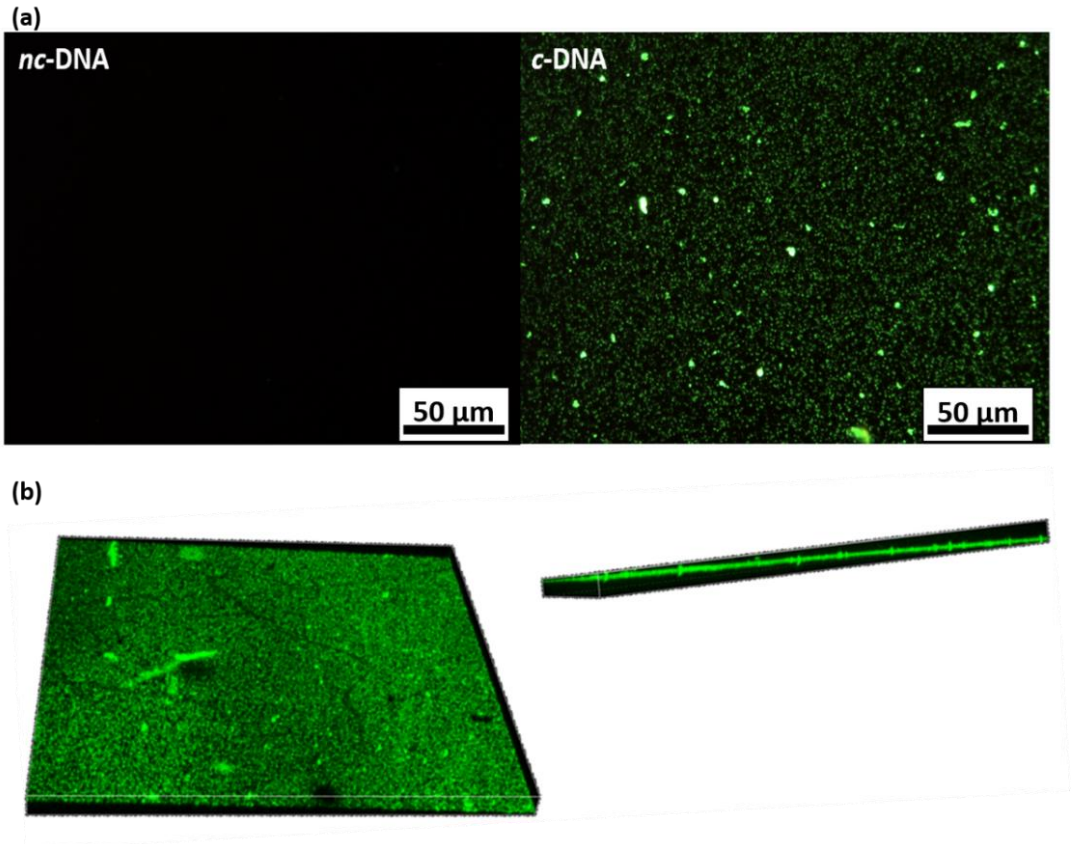

Figure 5 | 3. (a) Fluorescence images of PSi/GO/PNA device incubated with FITC-labeled nc-DNA and c-DNA sequences, both at 100 µM concentration. (b) Confocal microscopy image of c-DNA-incubated chip (3D front and side views). The infiltration of the labeled target within the porous structure can be clearly evidenced.

In summary, the fabricated PSi/GO hybrid structure was tested as multi-parametric platform for the label-free detection of the SCN5A point-mutation sequence region responsible for Brugada syndrome via covalent PNA anchoring. The interest in the use of PNA as bioprobe is essentially due to its capability to discriminate mutations associated to genetic diseases at the single-base level. First, the trackable PL quenching of GO allowed to estimate the optimal amount of bioprobe that maximizes the passivation of the surface. Subsequently, in order to evaluate the capability to detect the occurred PNA/DNA hybridization, the PSi/GO device was incubated with a c-DNA sequence and the response was assessed by FFT analysis of the reflectance spectra, which provided a trace of the effective interaction between the PSi/GO/PNA hybrid structure and the c-DNA sequence. Fluorescence and confocal microscopy were also used to confirm the highly specific hybridization process within the porous matrix. These preliminary data constitute the starting point for the development of a label-free biosensor with high stability, fast response time and high specificity exploitable for early genetic diseases diagnostics.

5.2 Label-free biosensing with fluorine-doped ZnO nanostructures

The improvement in bioprobe anchoring efficiency on ZnO nanostructures induced by fluorine doping has been evidenced and demonstrated in Section 3.3.2. After the characterization of the surface functionalization by the standard methods of confirming the immobilization of FITC-labeled protein A, samples of nZnO-F and nZnO were grown on silicon and functionalized with unlabeled PrA at different concentrations (2 mg/mL; 4 mg/mL; 6 mg/mL); in this case, the surface modification and PrA conjugation was monitored using photoluminescence analysis. In fact, the PL emission of the nanostructured ZnO is sensitive to the chemical modification of the material surface and can be used for monitoring biomolecular interactions in label-free optical sensing experiments [92]. Steady-state photoluminescence (PL) spectra of samples were excited by a continuous wave He-Cd laser at 325 nm (KIMMON Laser System). PL was collected at normal incidence to the surface of samples through a fiber, dispersed in a spectrometer (Princeton Instruments, Trenton, NJ, USA SpectraPro 300i), and detected using a Peltier-cooled charge-coupled device (CCD) camera (PIXIS 100F). A long-pass filter with a nominal cut-on wavelength of 350 nm was used to remove the laser line at the monochromator inlet.

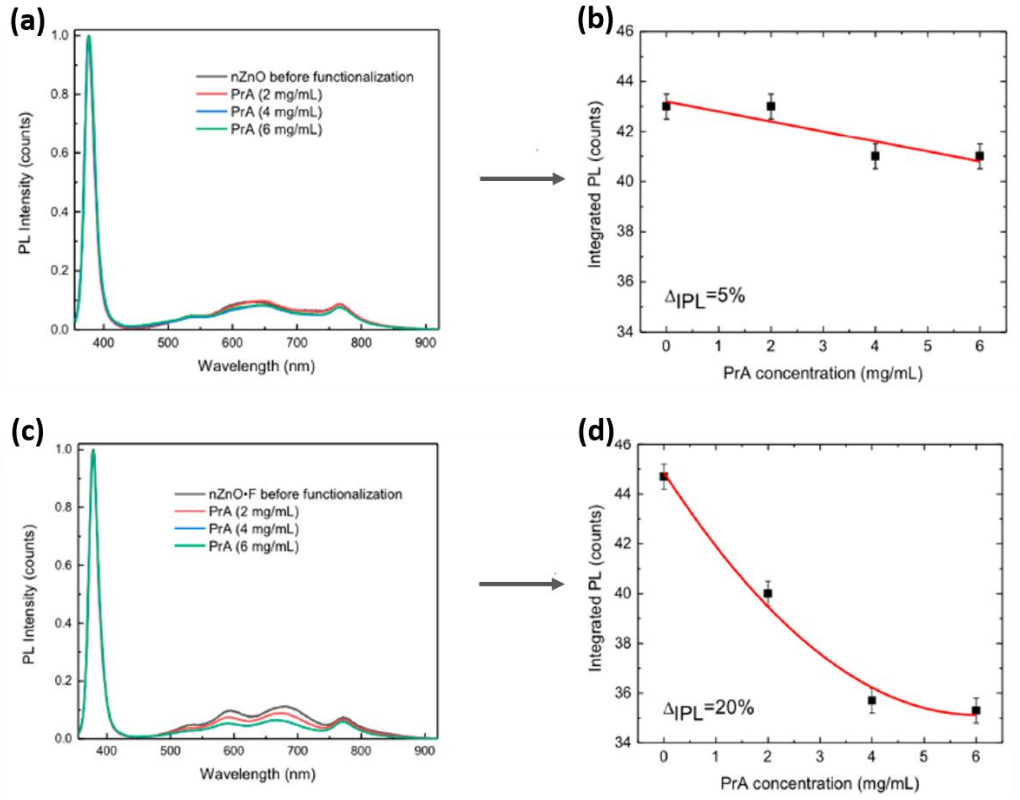

Figure 5 | 4. (a) Normalized PL spectra of nZnO surface after incubation with ulabeled PrA at different concentrations. (b) Plot of the integrated PL intensity as a function of the incubated [PrA]. (c) and (d) represent the same characterizations on nZnO-F surface.

Figure 5 | 4(a,c) report the PL spectra of the nZnO and nZnO-F, respectively, before (black lines) and after the surface functionalization with 2 mg/mL, 4 mg/mL and 6 mg/mL of PrA. For both materials, any variation of the peak at 380 nm (ascribed to near band edge excitonic transitions – cf. Section 1.3) was not observed. On the contrary, the intensity of the broad visible band, included between 500 and 800 nm and mainly related to the surface defects, decreased at the increasing of PrA concentration. By calculating the integrated PL intensities (I_{PL}) and plotting them as a function of the incubated PrA concentration (Figure 5 | 4(b,d)), a global variation of 20% could be obtained for the fluorine-doped sample and only 5% for the undoped sample. Such percentage variations were herein calculated as:

$$\Delta I_{PL} = \left| \frac{I_{PL}(6\ mg/mL) - I_{PL}(0)}{I_{PL}(0)} \right| \times 100.$$

To conclude, the interaction between nZnO-F and increasing concentrations of unlabeled PrA was characterized and quantified by photoluminescence analysis. The

results of the optical characterizations demonstrated that the fluorine-doped nZnO-F matrix could be better functionalized with respect to the undoped one, nZnO; the effect was attributed to the wrinkled flake-like morphology, which allowed the immobilization of a higher percentage of the biomolecule under investigation compared to the highly packed hexagonal nanocolumns of the undoped sample. The data reported in this study highlighted that nZnO-F could be effectively modified in order to fabricate a useful platform for label-free optical sensing.

Conclusions

In the present thesis, the potentialities of three inorganic nanomaterials with distinctive photoemissive behavior, i.e. PSiNPs, GO and nanostructured ZnO, have been discussed and exploited for applications in biophotonics.

The morphological, structural and optical properties of highly luminescent PSiNPs have been deeply investigated and characterized. The spectroscopic variation, both stationary and in the time domain, before and after covalent surface modification, has been carefully probed. Subsequently, the enhancement in the morphological and emissive stability of PSiNPs in physiological medium has been evaluated and successfully demonstrated after covalent capping with undecylenic acid, thus paving the way for the employment of such nanomaterial as label-free luminescent probe for bioimaging. MTT cell viability assay and fluorescence imaging of HeLa cells have validated the feasibility of usage of the functionalized PSiNPs *in vitro*.

In order to pursue the *in vivo* application using *Hydra vulgaris* as target organism, at first, a morphological screening of the animals after incubation for prolonged times and at high concentrations of UA-conjugated and bare PSiNPs has been performed. The data confirm an excellent biocompatibility, conferring a score 10 according to Wilby's classification. The optimization of a protocol for straightforward conjugation of poly-L-lysine *via* electrostatic interaction (to tune the surface charge of PSiNPs) has proved to be necessary to promote the uptake in the living organism. This surface modification introduced a moderate toxicity at high concentrations and prolonged incubation times, thus imposing the requirement of lower dosages. Subsequently to the working conditions optimization, the interaction between living *Hydra* and PLL-conjugated PSiNPs has been successfully observed *via* fluorescence imaging in real time. Finally, time-gated PL imaging has undoubtedly proved PLL-conjugated PSiNPs internalization in the sub-ectodermal region after limited-time incubation, overcoming the issue of endogenous autofluorescence by temporally sorting the signals. All observations have been successfully conducted *in vivo*. Future perspectives may include further improving in the surface functionalization, both in terms of biocompatibility and engineering with specific functionalities to improve the targeting (e.g., antibodies, aptamers and other biorecognition elements).

Carbodiimide crosslinking chemistry has been wisely exploited to develop a hybrid chip that combines the photonic properties of a macroporous PSi monolayer and the characteristic PL emission from GO. The infiltration of GO nanosheets within the porous matrix is fingerprinted by an induced modulation of the PL signal, whose periodicity matches that of the interference fringes in the optical spectrum of the PSi-based Fabry-Pérot photonic structure, indicating a variation of the refractive index within the porous matrix. With the same chemical strategy, as well as optical monitoring techniques, two different bioprobes (PrA and a PNA sequence) have been successfully immobilized. The occupation and energy levels rearrangement of radiative recombination sites due to the covalent anchoring of the bioprobe results in a trackable quenching of the GO PL signal. Such phenomenon, coupled to the shift of the characteristic fringes of the photonic structure, outlines biosensing architectures with multi-parametric transduction. The developed architecture has been preliminarily tested for the label-free detection of the SCN5A gene point-mutation associated to Brugada syndrome, leading to a rapid and specific response.

Finally, an analysis of the optical behavior of ZnO and fluorine-doped ZnO nanostructures has been carried out, aiming at understanding the possible influence of F-doping in the optical response of the nanostructures. Contextually, a covalent functionalization process, exploiting silane crosslinking chemistry, has been optimized for the anchoring of functional biomolecules, using PrA as preliminary bioprobe. The higher specific surface area of F-doped ZnO nanostructures resulted in an enhancement of the response of the device after the anchoring of different concentrations of PrA with respect to the undoped case. The results constitute a promising proof-of-concept for the development of PL-based optical biosensing platforms.

References

[1] K. Goda, "Biophotonics and beyond," *APL Photonics*, vol. 4, no. 5. AIP Publishing, 01-May-2019.

[2] A. Uhlir, "Electrolytic Shaping of Germanium and Silicon," *Bell Syst. Tech. J.*, vol. 35, no. 2, pp. 333–347, Mar. 1956.

[3] L. T. Canham, "Silicon quantum wire array fabrication by electrochemical and chemical dissolution of wafers," *Appl. Phys. Lett.*, vol. 57, no. 10, pp. 1046–1048, Sep. 1990.

[4] V. Lehmann and U. Gösele, "Porous silicon formation: A quantum wire effect," *Appl. Phys. Lett.*, vol. 58, no. 8, pp. 856–858, Feb. 1991.

[5] M. J. Sailor, *Porous silicon in practice : preparation, characterization and applications*. Wiley-VCH, 2012.

[6] "Recommendations for the characterization of porous solids (Technical Report)," *Pure Appl. Chem.*, vol. 66, no. 8, pp. 1739–1758, 1994.

[7] K.-P. S. Dancil, D. P. Greiner, and M. J. Sailor, "A Porous Silicon Optical Biosensor: Detection of Reversible Binding of IgG to a Protein A-Modified Surface," *J. Am. Chem. Soc.*, vol. 121, no. 34, pp. 7925–7930, Sep. 1999.

[8] P. A. Snow, E. K. Squire, P. S. J. Russell, and L. T. Canham, "Vapor sensing using the optical properties of porous silicon Bragg mirrors," *J. Appl. Phys.*, vol. 86, no. 4, pp. 1781–1784, Aug. 1999.

[9] V. Mulloni and L. Pavesi, "Porous silicon microcavities as optical chemical sensors," *Appl. Phys. Lett.*, vol. 76, no. 18, pp. 2523–2525, May 2000.

[10] S. Li, D. Hu, J. Huang, and L. Cai, "Optical sensing nanostructures for porous silicon rugate filters," *Nanoscale Res. Lett.*, vol. 7, no. 1, p. 79, 2012.

[11] H. F. Arrand *et al.*, "Novel liquid sensor based on porous silicon optical waveguides," *IEEE Photonics Technol. Lett.*, vol. 10, no. 10, pp. 1467–1469, Oct. 1998.

[12] C. Pacholski, "Photonic crystal sensors based on porous silicon," *Sensors (Switzerland)*, vol. 13, no. 4. pp. 4694–4713, Apr-2013.

[13] H. D. Fuchs, M. Stutzmann, M. S. Brandt, M. Rosenbauer, J. Weber, and M. Cardona, "Visible luminescence from porous silicon and siloxene," *Phys. Scr.*, vol. 1992, no. T45, pp. 309–313, Jan. 1992.

[14] M. S. Brandt, H. D. Fuchs, M. Stutzmann, J. Weber, and M. Cardona, "The origin of visible luminescencefrom 'porous silicon': A new interpretation," *Solid State Commun.*, vol. 81, no. 4, pp. 307–312, 1992.

[15] M. J. Estes and G. Moddel, "A model of size-dependent photoluminescence in amorphous silicon nanostructures: Comparison with observations of porous silicon," *Applied Physics*

Letters, vol. 68, no. 13. pp. 1814–1816, 1996.

[16] P. D. J. Calcott, K. J. Nash, L. T. Canham, M. J. Kane, and D. Brumhead, "Identification of radiative transitions in highly porous silicon," *J. Phys. Condens. Matter*, vol. 5, no. 7, 1993.

[17] C. Delerue, G. Allan, and M. Lannoo, "Theoretical aspects of the luminescence of porous silicon," *Phys. Rev. B*, vol. 48, no. 15, pp. 11024–11036, 1993.

[18] O. Bisi, S. Ossicini, and L. Pavesi, "Porous silicon: A quantum sponge structure for silicon based optoelectronics," *Surface Science Reports*, vol. 38, no. 1. Elsevier Science Publishers B.V., pp. 1–126, 2000.

[19] G. Grosso and G. Pastori Parravicini, *Solid state physics*. Academic Press, 2013.

[20] N. W. Ashcroft and N. D. Mermin, *Solid state physics*. Harcourt College Publishers, 1976.

[21] D. Kovalev, H. Heckler, M. Ben-Chorin, G. Polisski, M. Schwartzkopff, and F. Koch, "Breakdown of the k-Conservation Rule in Si Nanocrystals," *Phys. Rev. Lett.*, vol. 81, no. 13, pp. 2803–2806, Sep. 1998.

[22] F. Sangghaleh, I. Sychugov, Z. Yang, J. G. C. Veinot, and J. Linnros, "Near-Unity Internal Quantum Efficiency of Luminescent Silicon Nanocrystals with Ligand Passivation," *ACS Nano*, vol. 9, no. 7, pp. 7097–7104, Jul. 2015.

[23] G. Ledoux *et al.*, "Photoluminescence properties of silicon nanocrystals as a function of their size," *Phys. Rev. B - Condens. Matter Mater. Phys.*, vol. 62, no. 23, pp. 15942–15951, Dec. 2000.

[24] B. Gelloz, "Photoluminescence of porous silicon," in *Handbook of Porous Silicon*, Springer International Publishing, 2014, pp. 307–320.

[25] N. Koshida and H. Koyama, "Visible electroluminescence from porous silicon," *Appl. Phys. Lett.*, vol. 60, no. 3, pp. 347–349, 1992.

[26] D. I. Kovalev, I. D. Yaroshetzkii, T. Muschik, V. Petrova-Koch, and F. Koch, "Fast and slow visible luminescence bands of oxidized porous Si," *Appl. Phys. Lett.*, vol. 64, no. 2, pp. 214–216, Jan. 1994.

[27] A. Loni, A. J. Simons, P. D. J. Calcott, and L. T. Canham, "Blue photoluminescence from rapid thermally oxidized porous silicon following storage in ambient air," *J. Appl. Phys.*, vol. 77, no. 7, pp. 3557–3559, Apr. 1995.

[28] J. L. Batstone, M. A. Tischler, and R. T. Collins, "Stability of visible luminescence from porous silicon," *Appl. Phys. Lett.*, vol. 62, no. 21, pp. 2667–2669, 1993.

[29] Y. H. Xie *et al.*, "Luminescence and structural study of porous silicon films," *J. Appl. Phys.*, vol. 71, no. 5, pp. 2403–2407, 1992.

[30] T. Jamieson, R. Bakhshi, D. Petrova, R. Pocock, M. Imani, and A. M. Seifalian, "Biological applications of quantum dots," *Biomaterials*, vol. 28, pp. 4717–4732, 2007.

[31] M. Dovrat, Y. Goshen, J. Jedrzejewski, I. Balberg, and A. Sa'ar, "Radiative versus nonradiative decay processes in silicon nanocrystals probed by time-resolved

photoluminescence spectroscopy," *Phys. Rev. B*, vol. 69, no. 15, p. 155311, Apr. 2004.

[32] Martin, Delerue, Allan, and Lannoo, "Theory of excitonic exchange splitting and optical Stokes shift in silicon nanocrystallites: Application to porous silicon.," *Phys. Rev. B. Condens. Matter*, vol. 50, no. 24, pp. 18258–18267, Dec. 1994.

[33] I. Mihalcescu, J. C. Vial, and R. Romestain, "Carrier localization in porous silicon investigated by time-resolved luminescence analysis," *J. Appl. Phys.*, vol. 80, no. 4, pp. 2404–2411, Aug. 1996.

[34] L. Pavesi, "Influence of dispersive exciton motion on the recombination dynamics in porous silicon," *J. Appl. Phys.*, vol. 80, no. 1, pp. 216–225, Jul. 1996.

[35] L. Pavesi and M. Ceschini, "Stretched-exponential decay of the luminescence in porous silicon," *Phys. Rev. B*, vol. 48, no. 23, pp. 17625–17628, Dec. 1993.

[36] A. K. Geim and K. S. Novoselov, "The rise of graphene," *Nat. Mater.*, vol. 6, no. 3, pp. 183–191, Mar. 2007.

[37] K. Novoselov, "Electric field effect in atomically thin carbon films," *Science (80-.).*, vol. 306, pp. 666–669, 2004.

[38] F. Bonaccorso, Z. Sun, T. Hasan, and A. C. Ferrari, "Graphene photonics and optoelectronics," *Nat. Photonics*, vol. 4, no. 9, pp. 611–622, Sep. 2010.

[39] C. T. Chien *et al.*, "Tunable photoluminescence from graphene oxide," *Angew. Chemie - Int. Ed.*, vol. 51, no. 27, pp. 6662–6666, Jul. 2012.

[40] Z. Luo, P. M. Vora, E. J. Mele, A. T. C. Johnson, and J. M. Kikkawa, "Photoluminescence and band gap modulation in graphene oxide," *Appl. Phys. Lett.*, vol. 94, no. 11, 2009.

[41] G. Eda *et al.*, "Blue photoluminescence from chemically derived graphene oxide," *Adv. Mater.*, vol. 22, no. 4, pp. 505–509, Jan. 2010.

[42] J. Shang, L. Ma, J. Li, W. Ai, T. Yu, and G. G. Gurzadyan, "The origin of fluorescence from graphene oxide," *Sci. Rep.*, vol. 2, 2012.

[43] K. P. Loh, Q. Bao, G. Eda, and M. Chhowalla, "Graphene oxide as a chemically tunable platform for optical applications," *Nat. Chem.*, vol. 2, no. 12, pp. 1015–1024, Dec. 2010.

[44] Abid, P. Sehrawat, S. S. Islam, P. Mishra, and S. Ahmad, "Reduced graphene oxide (rGO) based wideband optical sensor and the role of Temperature, Defect States and Quantum Efficiency," *Sci. Rep.*, vol. 8, no. 1, Dec. 2018.

[45] J. V. Frangioni, "In vivo near-infrared fluorescence imaging," *Current Opinion in Chemical Biology*, vol. 7, no. 5. Elsevier Ltd, pp. 626–634, 2003.

[46] X. Sun *et al.*, "Nano-graphene oxide for cellular imaging and drug delivery," *Nano Res.*, vol. 1, no. 3, pp. 203–212, Sep. 2008.

[47] P. A. Rodnyi and I. V. Khodyuk, "Optical and luminescence properties of zinc oxide (Review)," *Opt. Spectrosc. (English Transl. Opt. i Spektrosk.*, vol. 111, no. 5, pp. 776–785, Nov. 2011.

[48] K. Ellmer, A. Klein, and B. Rech, *Transparent Conductive Zinc Oxide*, vol. 104, no. 3. Springer, 2008.

[49] B. K. Meyer *et al.*, "Bound exciton and donor–acceptor pair recombinations in ZnO," *Phys. status solidi*, vol. 241, no. 2, pp. 231–260, Feb. 2004.

[50] A. Van Dijken, E. A. Meulenkamp, D. Vanmaekelbergh, and A. Meijerink, "The Kinetics of the Radiative and Nonradiative Processes in Nanocrystalline ZnO Particles upon Photoexcitation," *J. Phys. Chem. B*, vol. 104, no. 8, pp. 1715–1723, Mar. 2000.

[51] A. Kohan, G. Ceder, D. Morgan, and C. G. Van de Walle, "First-principles study of native point defects in ZnO," *Phys. Rev. B - Condens. Matter Mater. Phys.*, vol. 61, no. 22, pp. 15019–15027, 2000.

[52] M. Liu, A. H. Kitai, and P. Mascher, "Point defects and luminescence centres in zinc oxide and zinc oxide doped with manganese," *J. Lumin.*, vol. 54, no. 1, pp. 35–42, 1992.

[53] Ü. Özgür *et al.*, "A comprehensive review of ZnO materials and devices," *Journal of Applied Physics*, vol. 98, no. 4. pp. 1–103, 15-Aug-2005.

[54] J. Joo, J. F. Cruz, S. Vijayakumar, J. Grondek, and M. J. Sailor, "Photoluminescent Porous Si/SiO2 Core/Shell Nanoparticles Prepared by Borate Oxidation," *Adv. Funct. Mater.*, vol. 24, no. 36, pp. 5688–5694, Sep. 2014.

[55] M. B. Gongalsky *et al.*, "Enhanced photoluminescence of porous silicon nanoparticles coated by bioresorbable polymers," *Nanoscale Res. Lett.*, vol. 7, no. 1, p. 446, Aug. 2012.

[56] R. Boukherroub, D. D. M. Wayner, D. J. Lockwood, and L. T. Canham, "Passivated Luminescent Porous Silicon," *J. Electrochem. Soc.*, vol. 148, no. 9, p. H91, Sep. 2001.

[57] R. Boukherroub, J. T. C. Wojtyk, D. D. M. Wayner, and D. J. Lockwood, "Thermal hydrosilylation of undecylenic acid with porous silicon," *J. Electrochem. Soc.*, vol. 149, no. 2, Feb. 2002.

[58] A. Petit, M. Delmotte, A. Loupy, J.-N. Chazalviel, F. Ozanam, and R. Boukherroub, "Microwave Effects on Chemical Functionalization of Hydrogen-Terminated Porous Silicon Nanostructures," *J. Phys. Chem. C*, vol. 112, no. 42, pp. 16622–16628, Oct. 2008.

[59] L. A. Huck and J. M. Buriak, "UV-Initiated Hydrosilylation on Hydrogen-Terminated Silicon (111): Rate Coefficient Increase of Two Orders of Magnitude in the Presence of Aromatic Electron Acceptors," *Langmuir*, vol. 28, no. 47, pp. 16285–16293, Nov. 2012.

[60] M. Hasanzadeh Kafshgari, N. H. Voelcker, and F. J. Harding, "Porous Silicon Nanoparticles for Applications in Nano-medicine," in *Comprehensive Nanoscience and Nanotechnology*, Elsevier, 2019, pp. 211–226.

[61] B. Marciniec, H. Maciejewski, and P. Pawlu\u0107, "Hydrosilylation of Carbon–Carbon Multiple Bonds—Application in Synthesis and Materials Science," in *Organosilicon Compounds*, Elsevier, 2017, pp. 169–217.

[62] A. Williams and I. T. Ibrahim, "Carbodiimide chemistry: recent advances," *Chem. Rev.*, vol.

81, no. 6, pp. 589–636, Dec. 1981.

[63] G. T. Hermanson, *Bioconjugate Techniques: Third Edition*. Elsevier Inc., 2013.

[64] C. Wang, Q. Yan, H.-B. Liu, X.-H. Zhou, and S.-J. Xiao, "Different EDC/NHS Activation Mechanisms between PAA and PMAA Brushes and the Following Amidation Reactions," *Langmuir*, vol. 27, no. 19, pp. 12058–12068, Oct. 2011.

[65] J. Bart, R. Tiggelaar, M. Yang, S. Schlautmann, H. Zuilhof, and H. Gardeniers, "Room-temperature intermediate layer bonding for microfluidic devices," *Lab Chip*, vol. 9, no. 24, pp. 3481–3488, 2009.

[66] S. J. P. McInnes and N. H. Voelcker, "Porous silicon-polymer composites for cell culture and tissue engineering applications," in *Porous Silicon for Biomedical Applications*, Elsevier Ltd., 2014, pp. 420–469.

[67] F. Boccafoschi, L. Fusaro, and M. Cannas, "Immobilization of peptides on cardiovascular stent," in *Functionalised Cardiovascular Stents*, Elsevier, 2018, pp. 305–318.

[68] Y. Wang *et al.*, "Charge-Reversal APTES-Modified Mesoporous Silica Nanoparticles with High Drug Loading and Release Controllability," *ACS Appl. Mater. Interfaces*, vol. 8, no. 27, pp. 17166–17175, Jul. 2016.

[69] B. Qiao, T. J. Wang, H. Gao, and Y. Jin, "High density silanization of nano-silica particles using γ-aminopropyltriethoxysilane (APTES)," *Appl. Surf. Sci.*, vol. 351, pp. 646–654, Oct. 2015.

[70] J.-H. Park, L. Gu, G. von Maltzahn, E. Ruoslahti, S. N. Bhatia, and M. J. Sailor, "Biodegradable luminescent porous silicon nanoparticles for in vivo applications," *Nat. Mater.*, vol. 8, no. 4, pp. 331–336, Apr. 2009.

[71] A. Loni, L. T. Canham, T. Defforge, and G. Gautier, "Supercritically-Dried Porous Silicon Powders with Surface Areas Exceeding 1000 m2/g," *ECS J. Solid State Sci. Technol.*, vol. 4, no. 8, pp. P289–P292, May 2015.

[72] J. Joo *et al.*, "Enhanced quantum yield of photoluminescent porous silicon prepared by supercritical drying," *Appl. Phys. Lett.*, vol. 108, no. 15, p. 153111, Apr. 2016.

[73] G. Socrates, *Infrared and raman characteristic group frequencies : tables and charts.* John Wiley & Sons, 2007.

[74] L. De Stefano, I. Rendina, M. De Stefano, A. Bismuto, and P. Maddalena, "Marine diatoms as optical chemical sensors," *Appl. Phys. Lett.*, vol. 87, no. 23, p. 233902, Dec. 2005.

[75] L. Vivien and L. Pavesi, *Handbook of silicon photonics*. Taylor & Francis, 2013.

[76] C. Reichardt, "Solvatochromic Dyes as Solvent Polarity Indicators," *Chem. Rev.*, vol. 94, no. 8, pp. 2319–2358, Dec. 1994.

[77] K. Suzuki *et al.*, "Reevaluation of absolute luminescence quantum yields of standard solutions using a spectrometer with an integrating sphere and a back-thinned CCD detector," *Phys. Chem. Chem. Phys.*, vol. 11, no. 42, p. 9850, Nov. 2009.

[78] J. R. Lakowicz, *Principles of fluorescence spectroscopy*. Springer, 2006.

[79] D. C. Johnston, "Stretched exponential relaxation arising from a continuous sum of exponential decays," *Phys. Rev. B - Condens. Matter Mater. Phys.*, vol. 74, no. 18, 2006.

[80] P. M, "Interaction between Electrolyte Ions and the Surface of a Cell Lipid Membrane," *J. Phys. Chem. Biophys.*, vol. 5, no. 2, 2015.

[81] D. Mazia, G. Schatten, and W. Sale, "Adhesion of cells to surfaces coated with polylysine: Applications to electron microscopy," *J. Cell Biol.*, vol. 66, no. 1, pp. 198–200, Jul. 1975.

[82] L. Zhang *et al.*, "Preparation of graphene quantum dots for bioimaging application," *J. Nanosci. Nanotechnol.*, vol. 12, no. 3, pp. 2924–2928, 2012.

[83] W. Becker and A. Bergmann, "Detectors for High-Speed Photon Counting (Technical Note)," 2016.

[84] M. Wahl, "Technical Note on Time-Correlated Single Photon Counting," 2014.

[85] M. Terracciano *et al.*, "Solid phase synthesis of a thrombin binding aptamer on macroporous silica for label free optical quantification of thrombin," *RSC Adv.*, vol. 6, no. 90, pp. 86762–86769, 2016.

[86] Q. Shabir *et al.*, "Quantification and Reduction of the Residual Chemical Reactivity of Passivated Biodegradable Porous Silicon for Drug Delivery Applications," *Silicon*, vol. 10, no. 2, pp. 349–359, Mar. 2018.

[87] J. M. Harris, M. R. Sedaghat-Herati, P. J. Sather, D. E. Brooks, and T. M. Fyles, "Synthesis of New Poly(Ethylene Glycol) Derivatives," in *Poly(Ethylene Glycol) Chemistry*, Springer US, 1992, pp. 371–381.

[88] S. Sam *et al.*, "Semiquantitative study of the EDC/NHS activation of acid terminal groups at modified porous silicon surfaces," *Langmuir*, vol. 26, no. 2, pp. 809–814, Jan. 2010.

[89] C. Pacholski, M. Sartor, M. J. Sailor, F. Cunin, and G. M. Miskelly, "Biosensing Using Porous Silicon Double-Layer Interferometers: Reflective Interferometric Fourier Transform Spectroscopy," *J. Am. Chem. Soc.*, vol. 127, no. 33, pp. 11636–11645, Aug. 2005.

[90] I. Rea *et al.*, "Photoluminescence of Graphene Oxide Infiltrated into Mesoporous Silicon," *J. Phys. Chem. C*, vol. 118, no. 47, pp. 27301–27307, Nov. 2014.

[91] L. De Stefano and S. D'Auria, "Confocal imaging of protein distributions in porous silicon optical structures," *J. Phys. Condens. Matter*, vol. 19, no. 39, Oct. 2007.

[92] J. Politi, I. Rea, P. Dardano, L. De Stefano, and M. Gioffrè, "Versatile synthesis of ZnO nanowires for quantitative optical sensing of molecular biorecognition," *Sensors Actuators B Chem.*, vol. 220, pp. 705–711, Dec. 2015.

[93] J. Zhang, T. Liu, Y. Zhang, W. Zeng, F. Pan, and X. Peng, "Hydrothermal synthesis and growth mechanisms of different ZnO nanostructures and their gas-sensing properties," *J. Mater. Sci. Mater. Electron.*, vol. 26, no. 3, pp. 1347–1353, Mar. 2015.

[94] G. P. Papari *et al.*, “Morphological, Structural, and Charge Transfer Properties of F-Doped ZnO: A Spectroscopic Investigation,” *J. Phys. Chem. C*, vol. 121, no. 29, pp. 16012–16020, Jul. 2017.

[95] N. L. Brown, S. P. Bottomley, M. D. Scawen, and M. G. Gore, “A study of the interactions between an IgG-binding domain based on the B domain of staphylococcal protein a and rabbit IgG,” *Mol. Biotechnol.*, vol. 10, no. 1, pp. 9–16, Aug. 1998.

[96] E. CHACON, D. ACOSTA, and J. J. LEMASTERS, “Primary Cultures of Cardiac Myocytes as In Vitro Models for Pharmacological and Toxicological Assessments,” in *In Vitro Methods in Pharmaceutical Research*, Elsevier, 1997, pp. 209–223.

[97] Y. Park, J. Yoo, M. H. Kang, W. Kwon, and J. Joo, “Photoluminescent and biodegradable porous silicon nanoparticles for biomedical imaging,” *Journal of Materials Chemistry B*, vol. 7, no. 41. Royal Society of Chemistry, pp. 6271–6292, 2019.

[98] S. P. Low, K. A. Williams, L. T. Canham, and N. H. Voelcker, “Evaluation of mammalian cell adhesion on surface-modified porous silicon,” *Biomaterials*, vol. 27, no. 26, pp. 4538–4546, Sep. 2006.

[99] T. Laaksonen *et al.*, “Failure of MTT as a toxicity testing agent for mesoporous silicon microparticles,” *Chem. Res. Toxicol.*, vol. 20, no. 12, pp. 1913–1918, Dec. 2007.

[100] M. Terracciano, L. Stefano, C. Tortiglione, A. Tino, and I. Rea, “In Vivo Toxicity Assessment of Hybrid Diatomite Nanovectors Using Hydra vulgaris as a Model System,” *Adv. Biosyst.*, vol. 3, no. 4, p. 1800247, Apr. 2019.

[101] R. E. Steele, “Developmental signaling in Hydra: What does it take to build a ‘simple’ animal?,” *Developmental Biology*, vol. 248, no. 2. Elsevier, pp. 199–219, 2002.

[102] D. A. Holdway, K. Lok, and M. Semaan, “The acute and chronic toxicity of cadmium and zinc to two hydra species.,” *Environ. Toxicol.*, vol. 16, no. 6, pp. 557–65, 2001.

[103] M. Sakaguchi, A. Mizusina, and Y. Kobayakawa, “Structure, development, and maintenance of the nerve net of the body column in Hydra,” *J. Comp. Neurol.*, vol. 373, no. 1, pp. 41–54, Sep. 1996.

[104] M. Terracciano *et al.*, “Silica-Based Nanovectors: From Mother Nature to Biomedical Applications,” in *Algae - Organisms for Imminent Biotechnology*, InTech, 2016.

[105] B. Quinn, F. Gagné, and C. Blaise, “Hydra, a model system for environmental studies,” *Int. J. Dev. Biol.*, vol. 56, no. 6–8, pp. 613–625, 2012.

[106] O. K. Wilby and J. M. Tesh, “The Hydra assay as an early screen for teratogenic potential.,” *Toxicol. In Vitro*, vol. 4, no. 4–5, pp. 582–3, 1990.

[107] K. Isaksson, D. Åkerberg, M. Posaric-Bauden, R. Andersson, and B. Tingstedt, “In vivo toxicity and biodistribution of intraperitoneal and intravenous poly-l-lysine and poly-l-lysine/poly-l-glutamate in rats,” *J. Mater. Sci. Mater. Med.*, vol. 25, no. 5, pp. 1293–1299, May 2014.

[108] C. Tortiglione, A. Quarta, M. A. Malvindi, A. Tino, and T. Pellegrino, “Fluorescent nanocrystals reveal regulated portals of entry into and between the cells of Hydra,” *PLoS One*, vol. 4, no. 11, Nov. 2009.

[109] M. J. Sanderson, I. Smith, I. Parker, and M. D. Bootman, “Fluorescence microscopy,” *Cold Spring Harb. Protoc.*, vol. 2014, no. 10, pp. 1042–1065, Oct. 2014.

[110] F. Rost, “Fluorescence Microscopy, Applications,” in *Encyclopedia of Spectroscopy and Spectrometry*, Elsevier, 1999, pp. 565–570.

[111] D. M. Shcherbakova and V. V. Verkhusha, “Near-infrared fluorescent proteins for multicolor in vivo imaging,” *Nat. Methods*, vol. 10, no. 8, pp. 751–754, Aug. 2013.

[112] J. Bin Li, H. W. Liu, T. Fu, R. Wang, X. B. Zhang, and W. Tan, “Recent Progress in Small-Molecule Near-IR Probes for Bioimaging,” *Trends in Chemistry*, vol. 1, no. 2. Cell Press, pp. 224–234, 01-May-2019.

[113] K. Hanaoka, K. Kikuchi, S. Kobayashi, and T. Nagano, “Time-Resolved Long-Lived Luminescence Imaging Method Employing Luminescent Lanthanide Probes with a New Microscopy System,” *J. Am. Chem. Soc.*, vol. 129, no. 44, pp. 13502–13509, Nov. 2007.

[114] P. Wu and X. P. Yan, “Doped quantum dots for chemo/biosensing and bioimaging,” *Chem. Soc. Rev.*, vol. 42, no. 12, pp. 5489–5521, May 2013.

[115] M. Rajendran and L. W. Miller, “Evaluating the Performance of Time-Gated Live-Cell Microscopy with Lanthanide Probes,” *Biophys. J.*, vol. 109, no. 2, pp. 240–248, Jul. 2015.

[116] T. Pons, S. Bouccara, V. Loriette, N. Lequeux, S. Pezet, and A. Fragola, “In Vivo Imaging of Single Tumor Cells in Fast-Flowing Bloodstream Using Near-Infrared Quantum Dots and Time-Gated Imaging,” *ACS Nano*, vol. 13, no. 3, pp. 3125–3131, Mar. 2019.

[117] M. Sakiyama, H. Sugimoto, and M. Fujii, “Long-lived luminescence of colloidal silicon quantum dots for time-gated fluorescence imaging in the second near infrared window in biological tissue,” *Nanoscale*, vol. 10, no. 29, pp. 13902–13907, Aug. 2018.

[118] W. Yang, P. K. Srivastava, S. Han, L. Jing, C.-C. Tu, and S.-L. Chen, “Optomechanical Time-Gated Fluorescence Imaging Using Long-Lived Silicon Quantum Dot Nanoparticles,” *Anal. Chem.*, vol. 91, no. 9, pp. 5499–5503, May 2019.

[119] A. M. Derfus, W. C. W. Chan, and S. N. Bhatia, “Probing the Cytotoxicity of Semiconductor Quantum Dots,” *Nano Lett.*, vol. 4, no. 1, pp. 11–18, Jan. 2004.

[120] X. Cheng *et al.*, “Versatile ‘Click Chemistry’ Approach to Functionalizing Silicon Quantum Dots: Applications toward Fluorescent Cellular Imaging,” *Langmuir*, vol. 30, no. 18, pp. 5209–5216, May 2014.

[121] “Fluorescence Lifetime Imaging (FLIM) in Confocal Microscopy Applications: An Overview | Imaging & Microscopy - Research, Development, Production.” [Online]. Available: https://www.imaging-git.com/applications/fluorescence-lifetime-imaging-flim-confocal-microscopy-applications-overview. [Accessed: 29-Dec-2019].

[122] J. Joo, X. Liu, V. R. Kotamraju, E. Ruoslahti, Y. Nam, and M. J. Sailor, "Gated Luminescence Imaging of Silicon Nanoparticles," *ACS Nano*, vol. 9, no. 6, pp. 6233–6241, Jun. 2015.

[123] R. E. Connally and J. A. Piper, "Time-Gated Luminescence Microscopy," *Ann. N. Y. Acad. Sci.*, vol. 1130, no. 1, pp. 106–116, May 2008.

[124] M. Macklin, "The effect of urethan on hydra.," *Biol. Bull.*, vol. 150, no. 3, pp. 442–452, 1976.

[125] P. Brugada and J. Brugada, "Right bundle branch block, persistent ST segment elevation and sudden cardiac death: A distinct clinical and electrocardiographic syndrome. A multicenter report," *J. Am. Coll. Cardiol.*, vol. 20, no. 6, pp. 1391–1396, Nov. 1992.

[126] Q. Chen *et al.*, "Genetic basis and molecular mechanism for idiopathic ventricular fibrillation," *Nature*, vol. 392, no. 6673, pp. 293–296, Mar. 1998.

[127] S. G. Priori *et al.*, "2015 ESC Guidelines for the management of patients with ventricular arrhythmias and the prevention of sudden cardiac death the Task Force for the Management of Patients with Ventricular Arrhythmias and the Prevention of Sudden Cardiac Death of the European Society of Cardiology (ESC) Endorsed by: Association for European Paediatric and Congenital Cardiology (AEPC)," *European Heart Journal*, vol. 36, no. 41. Oxford University Press, pp. 2793-2867l, 2015.

[128] A. D. Snir and H. Raju, "Current Controversies and Challenges in Brugada Syndrome," *Eur. Cardiol. Rev.*, vol. 14, no. 3, pp. 1–6, Sep. 2019.

[129] F. Lucarelli, G. Marrazza, A. P. F. Turner, and M. Mascini, "Carbon and gold electrodes as electrochemical transducers for DNA hybridisation sensors.," *Biosens. Bioelectron.*, vol. 19, no. 6, pp. 515–30, Jan. 2004.

[130] R. P. Singh, B. K. Oh, and J. W. Choi, "Application of peptide nucleic acid towards development of nanobiosensor arrays," *Bioelectrochemistry*, vol. 79, no. 2. pp. 153–161, Oct-2010.

Appendix

A.1 Colorimetric biosensing with gold nanoparticles

Metal nanoparticles have been widely proposed as biosensing platforms in recent years due to their unique optical properties [1]. The interaction of light with metal nanostructures may induce coherent and non-propagating oscillations of free electrons with a resonance frequency, called localized surface plasmon resonance (LSPR) [2]. The main effects of LSPR are the enhancement of the electromagnetic field intensity near the nanoparticle surface and the appearance of a strong extinction peak [3]. The LSPR depends on the local environment so that a change of the local refractive index leads to an LSPR spectral shift, thus resulting in a color variation of NP colloidal solutions [4,5]. For such potential of probing a nanoscale region around their surface, nanoparticles have been successfully employed in molecular sensing [6-8]. As far as biosensing is concerned, considerable efforts have been directed to develop low-cost, easy, and rapid colorimetric diagnostic tools for point-of-care applications or even for home use [1]. For gold and silver nanoparticles, the LSPR falls in the visible range, but gold is generally preferred due to its biocompatibility, inertness and surface chemistry [9,10]. Colorimetric sensing based on gold nanoparticles (AuNPs) exploits the color change of suspensions from red to purple as a result of surface plasmon coupling between nanoparticles, specifically pinpointing the transition from a dispersed to an aggregated state [11,12].

Refractive index variations-related LSPR shifts in AuNPs can be engineered and exploited in biosensing by using biomolecular recognition elements such as antibodies (Abs). To date, various strategies have been developed to immobilize Abs on AuNPs surface with a specific orientation [13]. Mostly utilized immobilization methods are based on the decoration of the AuNP surface with bifunctional or mediator linkers, which lead to acceptable selectivity but also to a lack of reproducibility due to the long, wet-chemistry-based procedures which are usually required [14,15].

Recently, it has been shown that Abs can be directly immobilized on gold surfaces by using a UV light-induced approach, known as photochemical immobilization technique (PIT) [16-18]. In particular, the absorption of UV light by nearby aromatic amino acids leads to the breakage of selected disulfide bridges, and the subsequent reactive thiol groups covalently bind to the gold substrate. The effectiveness of PIT has already been widely

demonstrated in the case of gold surfaces functionalization [19-21]. Herein, the effectiveness of PIT on Ab-conjugated AuNPs will be demonstrated, turning them into immunoprobes that aggregate in the presence of antigens. Immunoglobulin G (IgG) antibody was herein used. The whole process, from functionalization to immunosensing, is depicted in Figure A | 1.

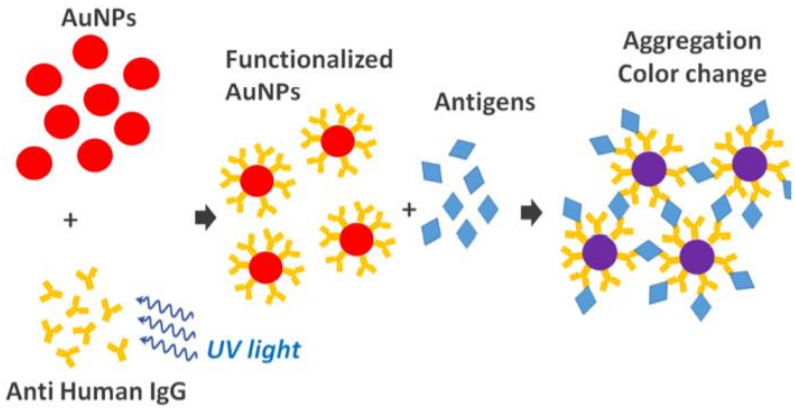

Figure A | 1. Outline of the AuNPs photochemical functionalization process and their application as colorimetric biosensor exploiting the LSPR peak shift.

A.1.1 AuNPs synthesis and PIT functionalization

Tetrachloroauric acid trihydrate ($HAuCl_4 \cdot 3H_2O$), sodium citrate and bovine serum albumin (BSA) were purchased from Sigma-Aldrich. Goat antihuman IgG, human IgG, and IgG from mouse were obtained from ImmunoReagents, Inc. Ultrapure water from Milli-Q system was used for all preparations. Synthesis of AuNPs. Spherical gold nanoparticles were synthesized by slightly modifying an established protocol [22]. A gold salt solution composed of 50 mL of ultrapure water and 500 µL and 8 mg/mL of $HAuCl_4 \cdot 3H_2O$ was prepared and boiled under constant stirring. Thus, 6 mL of 10 mg/mL sodium citrate was added, and the resulting solution was boiled for 2 min to achieve particles nucleation. After that, 4.8 mL of 8 mg/mL $HAuCl_4 \cdot 3H_2O$ was added to induce particles growth, and the stirring of the boiling solution was continued for 2 min. At the end of this process, the color of the suspension turned dark red. The AuNPs colloid was stored in dark at 4 °C.

In order to proceed with the photochemical functionalization, a 50 µg/mL antihuman IgG solution was prepared and irradiated for 1 min with a HERAEUS amalgam-

type NNI 40/20 lamp emitting at 254 nm with a power of 40 W, at an effective irradiation intensity of about 0.3 W/cm^2. A volume of 20 μL of the irradiated antihuman IgG solution was added to 1 mL of AuNPs previously purified by centrifugation at 3000 g for 10 mins and resuspension in ultrapure water. The resulting mixture was incubated for 3 min. The amount of antihuman IgG present in the mixture was progressively increased by adding 4 μL of the irradiated antibody solution. Unbound Abs were removed by centrifugation at 3000 g for 10 min and subsequent resuspension of Ab-functionalized AuNPs in ultrapure water. Finally, 1 mg/mL BSA was added to the functionalized colloid to block AuNPs surface from nonspecific adsorption.

A.1.2 AuNPs and PIT-functionalized AuNPs characterization

UV−vis absorption spectroscopy and dynamic light scattering (DLS) were used here to characterize both bare and antihuman IgG functionalized AuNPs and, afterwards, to study the optical response of the functionalized colloid in presence of the antigen human IgG. The UV−vis absorption spectra were recorded using a Jenway 6715 UV-vis spectrophotometer with 0.1 nm resolution and 0.2 nm spectral bandwidth. Hydrodynamic diameter and ζ potential measurements were performed with Zetasizer Nano ZS (Malvern Instruments) equipped with a 633 nm He−Ne laser at the detection angle of 173°. The morphology of as-synthesized AuNPs, Ab-functionalized AuNPs and antigen-induced aggregates were analyzed by a Zeiss ∑IGMA field emission scanning electron microscope (FESEM) with a nominal resolution of ∼3 nm at 1 kV.

Both UV-vis absorption spectroscopy and SEM images (Figure A | 2) highlight the presence of quite regular spherical monodisperse nanoparticles with a diameter of approximately 40 nm after the synthesis (Figure A | 2(a)). Figure A | 2(b) shows the UV−vis absorption spectra of the same AuNPs (solid black line) that reveal an LSPR band centered at 530.2 nm, as expected for spherical AuNPs with 40 nm [23]. Nevertheless, dynamic light scattering (DLS) measurements confirmed the AuNPs size determined by SEM images, providing a hydrodynamic diameter of about 40 nm and a polydispersity index of 0.2. The mean ζ potential has been measured to be −32 ± 1 mV, thereby confirming the existence of electrostatic repulsion forces among the particles that prevent their aggregation (data not shown).

After PIT functionalization, the UV−vis absorption spectra showed a red shift of the maximum absorption wavelength as a result of the formation of a protein corona [22].

The red shift stabilization occurred at 1 μg/mL antihuman IgG concentration, thus corresponding to the maximum coverage of the AuNPs surface. After the functionalization with IgG, the solution was centrifuged and the AuNPs pellet was resuspended in pure water. The dotted red line in Figure A | 2(b) shows that the functionalized nanoparticles have the same spectrum except from a $\Delta\lambda \sim 3.4$ nm red shift (dotted red line) as a consequence of the protein layer tethered to the gold surface. The two spectra show the same overall shape and intensity, thereby demonstrating a successful conjugation of the antibody to the gold surface without any significant lack of AuNP during the centrifugation and the subsequent resuspension. It is worth noticing that the absorption spectrum of the functionalized AuNPs was recorded after only 5 min of incubation. Despite seeming short, this time resulted sufficient to reach the equilibrium because no further change in the absorption spectrum was observed for incubation times >5 min. Furthermore, the LSPR peak position resulted unchanged even after blocking with BSA, suggesting the effectiveness of PIT in AuNPs because it provides both a stable attachment and a high surface coverage.

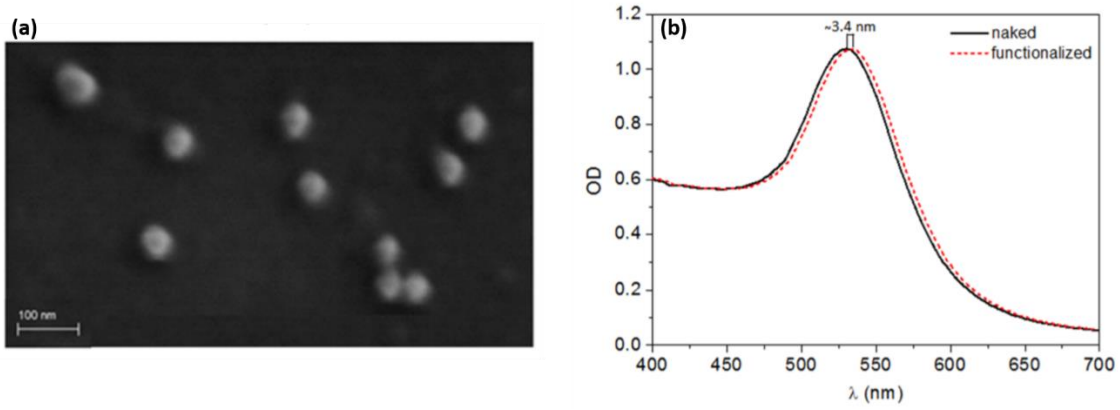

Figure A | 2. (a) SEM image of Ab-functionalized AuNPs. (b) UV-vis absorption spectra of AuNPs prior to and after Ab functionalization (1 μg/mL irradiated human IgG concentration) and BSA blocking.

A.1.3 Human IgG biosensing with PIT-functionalized AuNPs

Various amounts of human IgG in the range of 5 ng/mL to 1 μg/mL were added to 1 mL aliquots of the Ab-functionalized AuNPs and the samples were incubated at room temperature. Then, UV−vis absorption spectra in the 400-700 nm spectral range were collected at different incubation times to study the optical response of the system and its changes over time.

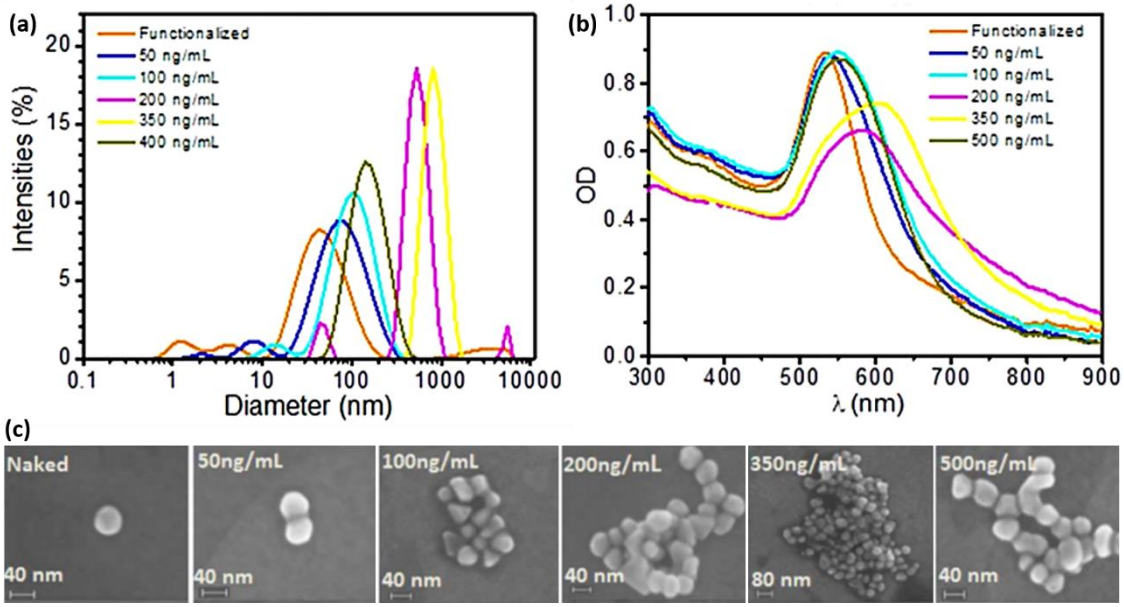

Figure A | 3. Colorimetric biosensing response of PIT-functionalized AuNPs colloid. (a) Hydrodynamic diameter distributions; (b) UV-vis absorption spectra and (c) representative SEM images in the range of 50-500 µg/mL human IgG concentrations.

The behavior of AuNPs as a biosensor is described inFigure A | 3, where both hydrodynamic diameter increase (Figure A | 3 (a)) and LSPR peak shifts (Figure A | 3(b)) are the results of the change of cluster size induced by the antigens (human IgGs) that act as linkers between nanoparticles when grafted on their surface. The structures reported in Figure A | 3(c) are representative of the cluster size distributions for several antigen concentrations. As clearly observable, the presence of the analyte promotes aggregation until the optimum concentration of about 350 ng/mL is reached. Interestingly, after that, further increase of the concentration hampers the aggregation. This is because beyond such a value the AuNPs are saturated with the antigens, which do not bind each other, thereby preventing nanoparticles from aggregating. Such a dynamics is well-known in immunology as “prozone” or “hook effect” and may give rise to false negative when the analyte concentration is too high [24]. This effect can be easily overcome with a double measurement at two different concentrations (serial dilutions) so that one can easily discriminate whether the low signal arises from a concentration that is too low or too high.

The shift of the resonance peak wavelength as a function of human IgG concentration is reported in Figure A | 4, which constitutes the dose−response curve for the colorimetric immunosensor. At human IgG concentration lower than 20 ng/mL, only a

small shift (<2 nm) of the resonance wavelength is observed, but at higher analyte concentrations, a significant red-shift occurs, which is responsible for a color change from red to purple. The maximum of the dose−response curve and the region around it are referred to as hook point and zone of equivalence, respectively. At concentrations below the hook point, the number of bind human IgG Abs is relatively low and aggregation is not optimized (small red-shift), whereas at concentration of human IgG above the hook point, the binding sites of the AuNPs tend to saturate again and result in a reduced cross-linking, thus justifying the observed reduced red-shift.

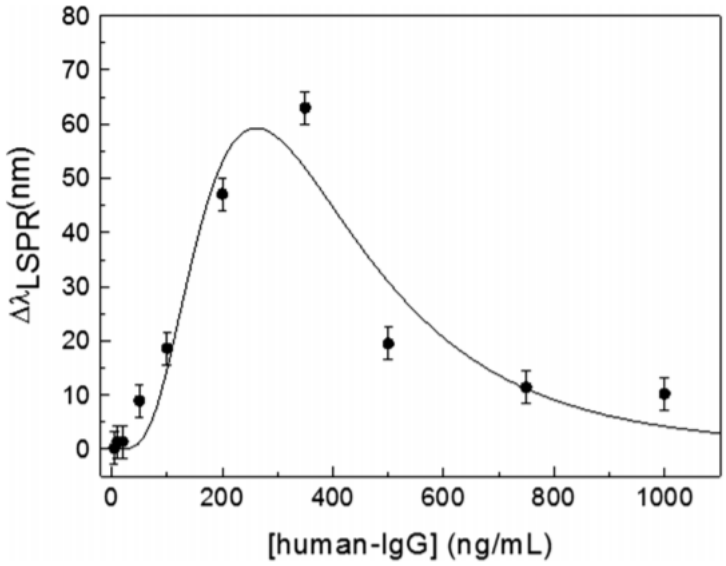

Figure A | 4. Dose-response curve of PIT-functionalized AuNPs immunosensor, expressed in terms of the LSPR peak shift as a function of the antigen concentration.

Finally, the specificity of the developed immunosensor was evaluated. In particular, possible cross-reactions with a similar protein, mouse IgG (with which human IgG shares a significant common portion), were checked. To this aim, 4 μL of a solution containing 50 μg/mL mouse IgG was added to 1 mL of the sensing solution containing approximately 6 × 10^{10} NPs/mL. The absorption spectra measured after 1 h even after 24 h incubation showed no substantial change (Figure A | 5), thereby demonstrating not only the lack of any cross-reaction with mouse IgG, but also the long-term stability of the PIT-functionalized colloid.

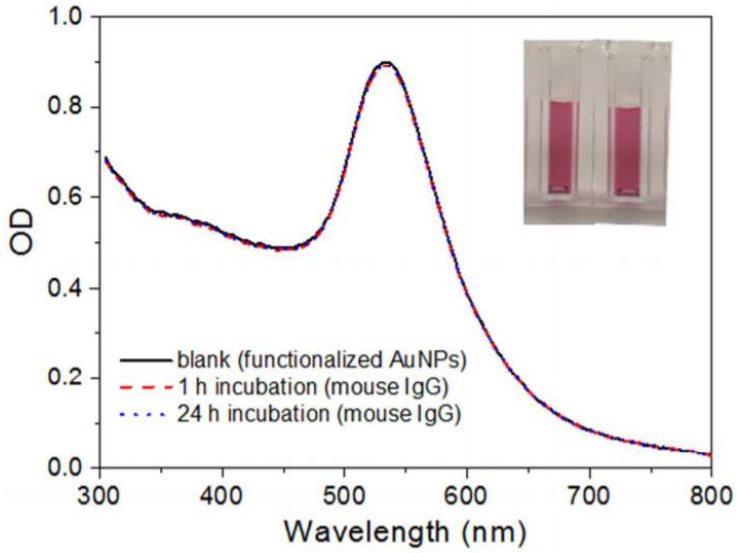

Figure A | 5. Specificity test towards 200 ng/mL of mouse IgG. No shift in the LSPR peak in the UV-vis spectra nor differences by the naked eye (inset) were evidenced for up to 24 h incubation.

To conclude, a colorimetric immunosensor for the detection of human IgG based on Ab-functionalized AuNPs was herein presented. The stability of the colloidal solution is warranted by the covalent anchoring of Abs achieved with PIT. The specificity is inherently warranted by the presence of antibodies acting as biorecognition elements. Plus, the performances in terms of sensitivity and limit of detection allow its application in scenarios where fast response is required. The presence of human IgG is immediately visualized as a change of the color of the solution due to the formation of aggregates. The positive response range for human IgG is 50−500 ng/mL, thereby making it suitable for application to medical diagnostics in a number of circumstances. The possible artifacts brought about by hook effects can be easily overcome by serial dilutions made affordable by the prompt response (few minutes) and ease of use.

References

[1] L. Tang and J. Li, “Plasmon-Based Colorimetric Nanosensors for Ultrasensitive Molecular Diagnostics,” ACS Sensors, vol. 2, no. 7, pp. 857–875, Jul. 2017.

[2] M. Li, S. K. Cushing, and N. Wu, “Plasmon-enhanced optical sensors: A review,” Analyst, vol. 140, no. 2. Royal Society of Chemistry, pp. 386–406, 21-Jan-2015.

[3] E. Petryayeva and U. J. Krull, “Localized surface plasmon resonance: Nanostructures, bioassays and biosensing-A review,” Analytica Chimica Acta, vol. 706, no. 1. pp. 8–24, 07-Nov-2011.

[4] V. Amendola, R. Pilot, M. Frasconi, O. M. Maragò, and M. A. Iatì, “Surface plasmon resonance in gold nanoparticles: A review,” Journal of Physics Condensed Matter, vol. 29, no. 20. Institute of Physics Publishing, 20-Apr-2017.

[5] J. J. Mock, D. R. Smith, and S. Schultz, “Local Refractive Index Dependence of Plasmon Resonance Spectra from Individual Nanoparticles,” Nano Lett., vol. 3, no. 4, pp. 485–491, Apr. 2003.

[6] K.-S. Lee and M. A. El-Sayed, “Gold and Silver Nanoparticles in Sensing and Imaging: Sensitivity of Plasmon Response to Size, Shape, and Metal Composition,” J. Phys. Chem. B, vol. 110, no. 39, pp. 19220–19225, Oct. 2006.

[7] K. M. Mayer and J. H. Hafner, “Localized Surface Plasmon Resonance Sensors,” Chem. Rev., vol. 111, no. 6, pp. 3828–3857, Jun. 2011.

[8] N. M. Khashab, J. O. Durand, and J. I. Zink, “Engineering nanoparticles for sensing and biomedical applications: A themed collection,” Molecular Systems Design and Engineering, vol. 2, no. 4, Royal Society of Chemistry, pp. 347–348, 2017.

[9] X. Zhang, “Gold Nanoparticles: Recent Advances in the Biomedical Applications,” Cell Biochem. Biophys., vol. 72, no. 3, pp. 771–775, Jul. 2015.

[10] A. Chaudhary, S. Khan, A. Gupta, and C. K. Nandi, “Effect of surface chemistry and morphology of gold nanoparticle on the structure and activity of common blood proteins,” New J. Chem., vol. 40, no. 6, pp. 4879–4883, 2016.

[11] S. K. Ghosh and T. Pal, “Interparticle Coupling Effect on the Surface Plasmon Resonance of Gold Nanoparticles: From Theory to Applications,” Chem. Rev., vol. 107, no. 11, pp. 4797–4862, Nov. 2007.

[12] M. Nilam, A. Hennig, W. M. Nau, and K. I. Assaf, “Gold nanoparticle aggregation enables colorimetric sensing assays for enzymatic decarboxylation,” Anal. Methods, vol. 9, no. 19, pp. 2784–2787, May 2017.

[13] P. Tiwari, K. Vig, V. Dennis, and S. Singh, “Functionalized Gold Nanoparticles and Their Biomedical Applications,” Nanomaterials, vol. 1, no. 1, pp. 31–63, Jun. 2011.

[14] M. Hadi Jazayeri, H. Amani, A. A. Pourfatollah, H. Pazoki-Toroudi, and B. Sedighimoghaddam, “Various methods of gold nanoparticles (GNPs) conjugation to antibodies,” 2016.

[15] N. Mustafaoglu, T. Kiziltepe, and B. Bilgicer, “Site-specific conjugation of an antibody on a gold nanoparticle surface for one-step diagnosis of prostate specific antigen with dynamic light scattering,” Nanoscale, vol. 9, no. 25, pp. 8684–8694, Jul. 2017.

[16] B. Della Ventura, L. Schiavo, C. Altucci, R. Esposito, and R. Velotta, “Light assisted antibody immobilization for bio-sensing,” Biomed. Opt. Express, vol. 2, no. 11, p. 3223, Nov. 2011.

[17] R. Funari, B. Della Ventura, C. Altucci, A. Offenhäusser, D. Mayer, and R. Velotta, “Single Molecule Characterization of UV-Activated Antibodies on Gold by Atomic Force Microscopy,” Langmuir, vol. 32, no. 32, pp. 8084–8091, Aug. 2016.

[18] B. Della Ventura et al., “Biosensor surface functionalization by a simple photochemical immobilization of antibodies: Experimental characterization by mass spectrometry and surface enhanced Raman spectroscopy,” Analyst, vol. 144, no. 23, pp. 6871–6880, Dec. 2019.

[19] R. Funari et al., “Detection of parathion and patulin by quartz-crystal microbalance functionalized by the photonics immobilization technique,” Biosens. Bioelectron., vol. 67, pp. 224–229, May 2015.

[20] B. Della Ventura, N. Sakač, R. Funari, and R. Velotta, “Flexible immunosensor for the detection of salivary α-amylase in body fluids,” Talanta, vol. 174, pp. 52–58, Nov. 2017.

[21] B. Della Ventura et al., “Effective antibodies immobilization and functionalized nanoparticles in a quartzcrystal microbalance-based immunosensor for the detection of parathion,” PLoS One, vol. 12, no. 2, Feb. 2017.

[22] M. J. Pollitt, G. Buckton, R. Piper, and S. Brocchini, “Measuring antibody coatings on gold nanoparticles by optical spectroscopy,” RSC Adv., vol. 5, no. 31, pp. 24521–24527, 2015.

[23] P. N. Njoki et al., “Size Correlation of Optical and Spectroscopic Properties for Gold Nanoparticles,” J. Phys. Chem. C, vol. 111, no. 40, pp. 14664–14669, Oct. 2007.

[24] S. Amarasiri Fernando and G. S. Wilson, “Studies of the ‘hook’ effect in the one-step sandwich immunoassay,” J. Immunol. Methods, vol. 151, no. 1–2, pp. 47–66, Jul. 1992.

A.2 Scientific production

Publications

M. Iarossi, C. Schiattarella, I. Rea, L. De Stefano, R. Fittipaldi, A. Vecchione, R. Velotta, and B. Della Ventura, "Colorimetric Immunosensor by Aggregation of Photochemically Functionalized Gold Nanoparticles", ACS Omega 3(4), 3805-3812 (2018).

R. Moretta, M. Terracciano, P. Dardano, M. Casalino, L. De Stefano, C. Schiattarella, and I. Rea, "Toward Multi-Parametric Porous Silicon Transducers Based on Covalent Grafting of Graphene Oxide for Biosensing Applications", Frontiers in Chemistry 6, 583 (2018).

C. Schiattarella, M. Terracciano, T. Defforge, G. Gautier, B. Della Ventura, R. Moretta, L. De Stefano, R. Velotta, and I. Rea, "Photoemissive properties and stability of undecylenic acid-modified porous silicon nanoparticles in physiological medium", Applied Physics Letters 114, 113701 (2019).

G. Chianese, M. Terracciano, R. Moretta, P. Cappiello, G. Vitiello, A. Aronne, C. Schiattarella, L. De Stefano, and I. Rea. "Synthesis and Surface Modification of Nanostructured F-Doped ZnO: Toward a Transducer for Label-Free Optical Biosensing", Applied Sciences 9(16), 3380 (2019).

Conference proceedings

C. Schiattarella, M. Terracciano, T. Defforge, G. Gautier, B. Della Ventura, R. Moretta, L. De Stefano, R. Velotta, and I. Rea, "Nanostructured silicon-based nanoparticles as label-free photoluminescent probes for *in vivo* imaging", in IEEE Xplore®, proceeding of 20th Italian National Conference on Photonic Technologies (Fotonica 2018), Lecce, 2018.

C. Schiattarella, G. Vitiello, M. Terracciano, R. Moretta, I. Rea, B. Silvestri, A. Aronne, and L. De Stefano, "Highly photo-emissive F-doped ZnO for optical biosensing", in IEEE Xplore®, proceeding of 20th Italian National Conference on Photonic Technologies (Fotonica 2018), Lecce, 2018.

Oral presentations

C. Schiattarella, M. Terracciano, T. Defforge, G. Gautier, C. Tortiglione, R. Moretta, B. Della Ventura, L. De Stefano, R. Velotta, and I. Rea, "Emission properties of functionalized porous silicon nanoparticles for *in vivo* imaging", at 7th EOS Topical Meeting on Optical Microsystems, 11-14 September 2017, Capri (NA), Italy.

C. Schiattarella, M. Terracciano, T. Defforge, G. Gautier, B. Della Ventura, R. Moretta, L. De Stefano, R. Velotta, and I. Rea, "Functionalized silicon nanostructures for selective label-free bioimaging", at Europt(r)ode XIV, 25-28 March 2018, Naples, Italy.

C. Schiattarella, R. Moretta, R. Schettino, N. Borbone, G. Piccialli, G. Oliviero, M. Terracciano, P. Dardano, M. Casalino, I. Rea, and L. De Stefano, "Graphene Oxide-Porous Silicon Device for Multiparametric Detection of Biomolecular Interactions", at XX AISEM 2019, 11-13 February 2019, Naples, Italy.

I. Rea, M. Terracciano, R. Moretta, C. Schiattarella, P. Dardano, and L. De Stefano, "Highly Photo-emissive Semiconductor Nanoparticles for Optical Imaging and Sensing" ***invited*** oral for 41st PIERS 2019 in Rome, 17-20 June 2019, Rome, Italy.

C. Schiattarella, I. Rea, P. Dardano, R. Moretta, M. Terracciano, and L. De Stefano, "Porous Silicon-based Hybrid Devices for Multi-parametric Photonic Biosensors", ***invited*** oral for 41st PIERS 2019 in Rome, 17-20 June 2019, Rome, Italy.

C. Schiattarella, M. Terracciano, T. Defforge, G. Gautier, C. Tortiglione, R. Moretta, B. Della Ventura, L. De Stefano, R. Velotta, and I. Rea, "Time-gated imaging of luminescent microporous silicon nanoparticles in living Hydra polyps", at 8th EOS Topical Meeting on Optical Microsystems, 9-11 September 2019, Capri (NA), Italy.

C. Schiattarella, R. Moretta, M. Terracciano, T. Defforge, G. Gautier, C. Tortiglione, B. Della Ventura, L. De Stefano, R. Velotta, and I. Rea, "Biocompatible luminescent silicon nanostructures for label-free time-gated *in vivo* imaging in *Hydra vulgaris*", at FisMat2019, 30 September - 4 October 2019, Catania, Italy.

C. Schiattarella, R. Moretta, T. Defforge, G. Gautier, C. Tortiglione, B. Della Ventura, M. Terracciano, L. De Stefano, R. Velotta, and I. Rea, "Poly-L-lysine-conjugated porous silicon nanoparticles as label-free luminescent probes for *in vivo* time-gated imaging

of *Hydra vulgaris*", *accepted as oral* at PSST 2020 – Porous Semiconductors – Science and Technology 2020, 15-20 March 2020, Lido di Camaiore (LU), Italy ***(postponed)***.

Poster presentations

C. Schiattarella, M. Terracciano, T. Defforge, G. Gautier, C. Tortiglione, R. Moretta, L. De Stefano, R. Velotta and I. Rea, "*In vivo* imaging by chemically modified photoluminescent porous silicon nanoparticles", at PSST 2018 – Porous Semiconductors – Science and Technology 2018, 11-16 March 2018, La Grande Motte, France.

A.3 Other national/international experiences

Doctoral schools/courses attended

1st International School on Nano-Tooling - Manipulating, Shaping and Functionalizing the Matter, 30-31 March 2017, Pozzuoli (NA), Italy.

10th Advanced Study Course on Optical Chemical Sensors (ASCOS 2017), 20-27 July 2017, Třešť, Czech Republic.

Terza Scuola Nazionale Biosensori Ottici e Biofotonica (BiO&B), 11-15 December 2017, Naples, Italy.

2018 Summer School for Silicon Nanotechnology (SSSiN 2018), 9 July – 17 August 2018, La Jolla (CA), United States.

International visiting experience

Prof. M. J. Sailor Lab, Department of Chemistry and Biochemistry, University of California San Diego, 9500 Gilman Dr, La Jolla, CA 92093, United States (from July 6 to December 14, 2018).